NTNU

Norwegian University of
Science and Technology

# Exploring supermagnetism in patterned thin films of $La_{0.7}Sr_{0.3}MnO_3$

Hans Henrik S Urdahl

Nanotechnology
Submission date: June 2016
Supervisor: Erik Folven, IET
Co-supervisor: Samuel Dingeman Slöetjes, IET

Norwegian University of Science and Technology
Department of Electronics and Telecommunications

**Abstract**

Supermagnetism refers to the collective magnetic ordering of superparamagnetic nanoparticles. The phenomenon may be used to engineer novel magnetic materials. To investigate how supermagnetism may be manifest in patterned thin films of the ferromagnetic complex oxide $La_{0.7}Sr_{0.3}MnO_3$ (LSMO), we used GPU-accelerated micromagnetic simulations to investigate the magnetic properties of single LSMO nanomagnets and ordered arrays of such nanomagnets. We found superparamagnetism in 5 nm thick, cylindrical LSMO nanomagnets at diameters of 20 nm to 140 nm. We then investigated the supermagnetic ground states of ordered arrays of LSMO nanomagnets, and found that by controlling the stacking of the arrays, the supermagnetic ground state could be tuned. Square stacking lead to superantiferromagnetic ground states and hexagonal stacking to superferromagnetic ground states. Effects of finite size and tuning the ground state by an applied field were discussed. We explored the hysteretic properties of the arrays, and found a step-like hysteresis curve for the square lattice. It was explained in terms of dipolar lattices and supermagnetic phase transitions, and compared with 2D Ising spin-lattices. The hexagonal array exhibited hysteresis similar to that of conventional soft magnetic materials. Spin-glass properties of the arrays were explored by looking at quenched disorder, and field-cooled and zero-field cooled magnetization of the arrays. Magnetic irreversibility was found, which was suggestive of spin-glass behavior. We conclude that ordered supermagnetic systems are excellent candidates for engineering artifical spin systems and magnetic metamaterials, either for technological or fundamental research purposes, and that such systems can be realized in patterned LSMO thin films.

**Sammendrag**

Supermagnetisme henviser til den kollektive magnetiske ordningen av superparamagnetiske nanopartikler. Fenomenet kan muligens brukes til å overkomme den superparamagnetiske effekten relatert til å skape nye magnetiske materialer. For å undersøke hvordan supermagnetisme manifesteres i mønstrede tynnfilmer av det ferromagnetiske komplekse oksidet $La_{0.7}Sr_{0.3}MnO_3$ (LSMO), brukte vi GPU-akselererte mikromagnetiske simuleringer for å undersøke de magnetiske egenskapene til enkelte LSMO nanomagneter og ordnede gitter av slike nanomagneter. Vi fant at ved å kontrollere gitterstrukturen, kunne den supermagnetiske grunntilstanden påvirkes. Kvadratiske gitter gav superantiferromagnetisk grunntilstand, og heksagonale gitter gav superferromagnetisk grunntilstand. Effekten av endelig størrelse og manipulering av grunntiltanden ved hjelp av et ytre felt ble diskutert. Vi utforsket de hysteretiske egenskapene til gitrene, og fant en trappetrinns-lignende hysteresekurve for det kvadratiske gitteret. Det ble forklart ved hjelp av dipol-gitter samt supermagnetiske faseoverganger, og sammenlignet med 2D Ising spinn-gitter. Det heksagonale gitteret hadde hysteretiske egenskaper som vanlige myke magnetiske materialer. Spinn-glass-egenskaper ble utforsket ved å se på uorden som følge av bråkjøling, samt felt-avkjølt og null-felt-avkjølt magnetisering. Magnetisk irreversibilitet ble funnet, hvilket var en indikasjon på spin-glass-oppførsel. Vi konkluderer med at ordnede, supermagnetiske systemer er utmerkede kandidater for å skape kunstige spinn-systemer og magnetiske metamaterialer, enten for teknologiske eller forskningsanvendelser, og at slike systemer kan realiseres i mønstrede tynnfilmer av LSMO.

# Preface

This thesis was written as the final part of my Master of Science in nanotechnology and nanoelectronics at the Norwegian University of Science and Technology (NTNU). The underlying research and the thesis itself were produced during my $10^{\text{th}}$ semester at NTNU, during the spring of 2016, at the Department of Electronics and Telecommunications.

The material parameters presented in Section 3.3 are reproduced and used with permission from Lee et. al [37]. Apart from that, this thesis consists of original, unpublished and independent work by the author.

I would like to thank my supervisor Assoc. Prof. Erik Folven and co-supervisor PhD. cand. Samuel Dingeman Slöetjes for valuable ideas and feedback during my work. The time and effort they dedicated to helping me produce this thesis is greatly appreciated.

# Contents

# List of Figures

# List of Tables

# Chapter 1

# Introduction

## 1.1 Motivation and background

Magnetism as a phenomenon has sparked excitement and interest among mankind ever since it was first described approximately 2500 years ago [55]. Since its discovery, magnetism has been utilized in a vast range of technological applications, from navigation to high tech applications such as modern digital data storage.

In todays society, magnetism is perhaps most prevalently encountered in electronic applications. Electronics have formed a backbone in modern society, especially since the invention of the transistor in 1947 [59], which ushered in a new era of modern radio and computer technology. The evolution of microelectronics has been a driving force for both research and economic growth all over the world. Today, information is stored, manipulated and transferred mainly via charge. Most transistors are found in highly integrated circuits. One of the main reasons for why integrated electronics have been so successful, is the concept of scaling. Scaling down physical dimensions has led to density, speed and power improvements [59], but a limit to scalability is quickly approaching, as the physical dimensions of components are approaching the atomic scale. The newest line of commercialized CPUs from Intel already have critical dimensions of 14 nm, and there have been difficulties in further downscaling [11].

As the microelectronic research roadmap nears its end, new venues must be explored. Spintronics (derived from the expression spin electronics) is one of the emerging concepts, that may possibly push the boundaries of state-of-the-art technology. Opposed to common belief, spintronics is more an augmentation of electronics, than it is a competitor. The fundamental concept of spintronics lies in the ability to sense and manipulate

the spin degree of freedom in solid state systems [68]. Since the spin degree of freedom is intimately connected to magnetism, there is reason to believe that magnetic materials will become ever more ubiquitous than what currently is the case.

A relatively new direction in magnetic spintronics and magnetoelectronics is called magnonics [44]. Magnonics focuses on the transfer of magnetic moment, or spin, by so-called spin waves. The aim is to be able to use spin waves as basis for devices for data processing, communications and storage. Using spin waves is a possible new route to processing information at the nanoscale [32].

The study of nanoscale magnetic materials has shown that such materials possess properties that are not present in their macroscopic bulk counterparts, such as the giant magnetoresistance (GMR) effect used in magnetic memory. GMR is a phenomenon where the electrical resistance of a thin film heterojunction consisting of a ferromagnetic layer, a metallic layer and another ferromagnetic layer can be tuned by controlling the magnetization directions of the thin films. The phenomenon can easily be understood from a semiclassical transport picture, where the transport is governed by the Boltzmann equation, in combination with spin-dependent scattering [16]. The phenomenon was discovered independently by two research groups in 1988 [3] and 1989 [9], and yielded the discoverers the Nobel Prize in Physics in 2007. This effect is widely used for instance in read heads for magnetic memory devices. Research on nanoscale magnetic materials may lead to the discovery of new and exciting properties.

One of the largest challenges of modern magnetic memory is related to thermal stability of recorded data [43]. In order to further improve on data storage density, the superparamagnetic effect (i.e. thermally activated switching of magnetic logic elements) must be mediated, either through engineering of more thermally stable magnetic materials for memory applications, or through entirely new approaches to data storage.

A possible new take on how to beat the superparamagnetic effect could be through use of the phenomenon referred to as supermagnetism. The essence of supermagnetism is the collective ordering of superparamagnetic nanoparticles [5]. In a sense, supermagnetism is an approach to exploit superparamagnetism and may lead to a whole new paradigm for engineering of magnetic materials [53].

An efficient way to learn more about supermagnetism in nanostructures is by use of computer simulations. By numerically solving dynamical equations for the magnetization of ferromagnetic materials, predictions can be made on how the magnetic properties of these materials are. Recent advances in GPU-accelerated parallel computing have allowed

simulation of systems that are orders of magnitude larger than what was previously possible. The speed up of modern, GPU-based simulation software as compared to older CPU-based software may be as much as two orders of magnitude [62]. Until recently, simulating supermagnetic systems using CPU-based computing has been unfeasible due to the computational costs, hence this work would not have been possible only a few years ago.

## 1.2 Project outline

In this project, we will explore supermagnetism in patterned thin films of $La_{0.7}Sr_{0.3}MnO_3$ (LSMO) using micromagnetic simulations as our tool. The main goal of the investigations is to find out if it is possible to fabricate supermagnetic structures based on LSMO thin film systems.

LSMO is an itinerant ferromagnetic metallic oxide with a bulk Curie temperature of approximately 380 K [40]. While several studies have looked at supermagnetic ordering between nanoparticles [41, 51, 18, 50, 47, 42] using analytical and experimental approaches, and substantial research has been done on the magnetic properties of LSMO thin films and nanoparticles or -islands [54, 57, 49, 29, 67], using micromagnetic simulations to explore the magnetic properties of nanoscale LSMO structures in connection with supermagnetic ordering has not been done. Inspired by recent studies [64, 63, 26], we will investigate the magnetic properties of both single-particle nanoscale LSMO, as well as ordered arrays of LSMO nanomagnets.

More specifically, we will explore the magnetic phase diagram of single LSMO nanomagnets. Based on the findings of the explorations, we will investigate how supermagnetic ordering can be tuned by varying coordination and geometry of regular nanomagnet lattices. To elucidate the magnetic properties of supermagnetic lattices, we will perform hysteresis simulations, and investigations of magnetic phase transitions due to temperature change.

## 1.3 Structure of thesis

The structure of the thesis is as follows. Chapter 2 is dedicated to developing the necessary theoretical framework. We will give a review of magnetism, the micromagnetic model and supermagnetism. In Chapter 3, we describe how micromagnetic simulations

are performed, the model system and the software used. Chapters 4 and 5 will be used to present and discuss the results from the simulations. Finally, in Chapter 6 we summarize our findings, present our conclusions and make suggestions for further work. Supplementary results and information can be found in Appendices A and B.

# Chapter 2

# Theory

In this chapter we will shortly review the necessary theoretical background for this work. In Section 2.1, we will give a brief description of classic magnetism. Section 2.2 is dedicated to the micromagnetic model, while Section 2.3 describes the relatively new field of supermagnetism. Our review of classic magnetism in solid materials will follow the general outline of Spaldin [52]. For a thorough description of the theory of magnetism, the reader is referred to the work of Stöhr and Siegmann [55].

## 2.1 Magnetism in solid materials

### 2.1.1 The microscopic origin of magnetism

A natural starting point for explaining magnetism in materials is with the discovery and formulation of Ampère's circuital law of magnetism, which relates the magnetic field to the angular momentum of an electrically charged body. Ampère did indeed hypothesize that all magnetic effects were a result of circulating molecular currents. This hypothesis turned out to be remarkably accurate, since later discoveries showed that magnetism arises mainly from the orbital angular momentum of electrons, in addition to the spin angular momentum of the electrons. The latter contribution was not identified until after Niels Bohr in 1913 postulated that the orbital angular momentum of the electron is quantized [10], which was confirmed by the famous Stern-Gerlach experiment in 1922 [25]. Although the electron spin was postulated already in 1921 by A. Compton [17] (albeit based on the wrong reasons), it was not before Uhlenbeck and Goudsmit in 1926 hypothesized the electron spin based on the fine structure of atomic spectra [61], that

the idea gained traction.

Hence, the magnetic moment of a free atom can be found through the use of Ampère's law and the total angular momentum of the electron. By vector addition of the magnetic moments of the electrons in a free atom, the total magnetic moment of the atom can be found. The picture is somewhat more complicated, since the atomic nuclei also has a small magnetic moment, but this is largely ignored, since the electronic contribution is far greater. For a material, comprised of atoms, the magnetic properties of the material is determined by the sum of the magnetic moments of each atom. Depending on the configurations of these moments, the material can be classified as ferro-, antiferro-, ferri-, dia- or paramagnetic. This will be further explained in Sections 2.1.2 and 2.1.3.

### 2.1.2 Magnetic materials and magnetization

The magnetization of a material, $\boldsymbol{M}$, is determined by the addition of all the magnetic moments of the atoms (or ions) of the material, as well as how these magnetic moments interact. The magnetization is defined as magnetic moment per unit volume, or $\boldsymbol{M} = \boldsymbol{m}/V$, and is a material specific property. Here, $\boldsymbol{m}$ is the total magnetic moment of volume element $V$. The response of a magnetic material to an applied magnetic field, $\boldsymbol{H}$, is called the magnetic induction (or magnetic flux density) $\boldsymbol{B}$. The relationship between $\boldsymbol{B}$, $\boldsymbol{H}$ and $\boldsymbol{M}$ is given by

$$\boldsymbol{B} = \mu_0 \left( \boldsymbol{H} + \boldsymbol{M} \right), \tag{2.1}$$

where $\mu_0$ is the permeability of free space. The units of $\boldsymbol{H}$ and $\boldsymbol{M}$ are A/m, $\boldsymbol{B}$ has units T and $\mu_0$ H/m. Another important property of a magnetic material is defined by how the magnetization varies with the applied field. This property is called the susceptibility, and can be defined as

$$\chi = \frac{\boldsymbol{M}}{\boldsymbol{H}}. \tag{2.2}$$

It is important to note that this definition is valid only for so-called linear materials. By combining Equations 2.1 and 2.2, we can write

$$\boldsymbol{B} = \mu_0 \left( 1 + \chi \right) \boldsymbol{H} = \mu_0 \mu_r \boldsymbol{H}, \tag{2.3}$$

where $\mu_r = 1 + \chi$ is the relative permeability of the magnetic material. We see that while the susceptibility describes the relation between the applied field and the magnetization of the material, the permeability relates the magnetic flux density in the material to the applied field. In linear materials these quantities are related.

### 2.1.3 Magnetization curves and hysteresis loops

One of the most common tools for determining and classifying the magnetic properties of a material is by plotting $\boldsymbol{M}$ versus $\boldsymbol{H}$ for the material. Such plots are called magnetization curves (or hysteresis loops, if the magnetization curve is performed over a full cycle of $\boldsymbol{H}$). By examining Eq. 2.2, we see that the slope of the magnetization curve, $\boldsymbol{M}(\boldsymbol{H})$, is the susceptibility. For para-, dia- and antiferromagnetic materials, the magnetization curve is linear, at least for small to intermediate applied fields, as illustrated in Figure 2.1. The atomic spin structure of para- and antiferromagnetic materials are illustrated in Figure 2.2. By considering the spin structure of these materials, the magnetization curves can be further understood. When an external field is applied, the spins of the para- or antiferromagnetic material will slowly align with the applied field, but when it is removed again, the atomic spins will relax to a similar structure to those exhibited in Figure 2.2.

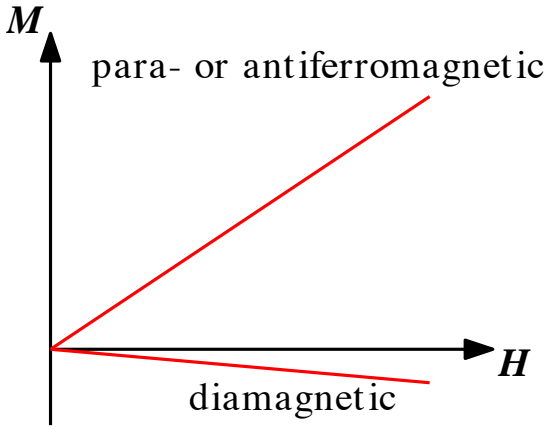


Figure 2.1: An illustration of typical magnetization curves for dia-, para- and antiferromagnetic materials.

The susceptibility of para- and antiferromagnetic materials is quite small if compared to ferromagnetic materials, and for diamagnetic materials, the susceptibility is in fact negative. The relative permeability of such materials is therefore also small. For para- and antiferromagnetic materials, $\mu_r \gtrsim 1$, whereas for diamagnetic materials, $\mu_r \lesssim 1$. What this means for the magnetization of these materials is that para- and antiferromagnets require quite large applied fields to achieve significant magnetization of the material. In addition, when the field is removed, the magnetization will vanish. Diamagnetic materials will actually oppose an applied field, so that the induced magnetization in the material is opposite to the applied field, but weak.

The magnetization curves for ferro- and ferrimagnetic materials are quite different from

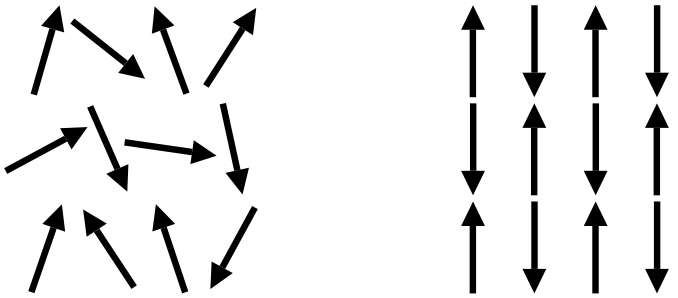

(a) (b)

Figure 2.2: Illustrations of typical ground state atomic spin structures of (a) a paramagnetic material and (b) an antiferromagnetic material. Both materials have zero net magnetization when no magnetic field is applied.

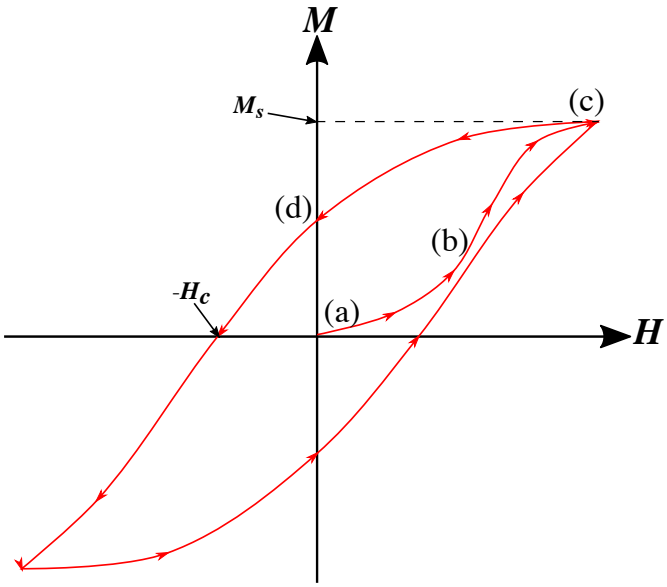


Figure 2.3: An illustration of a typical hysteresis loop for a ferro- or ferrimagnetic material. $\boldsymbol{M}_S$ is the saturation magnetization and $\boldsymbol{H}_c$ the coercive field. The magnetization at point (d) is often called the remanent magnetization, $\boldsymbol{M}_r$. Illustrations of the magnetic microstructure of a typical ferromagnet at points (a) through (d) are shown in Figure 2.4.

the before-mentioned materials. An illustration of a typical hysteresis loop is shown in Figure 2.3. The difference between a magnetization curve and a hysteresis loop is illustrated well by this figure. Whereas the magnetization curve only consists of the parts of the curve starting at point (a) and ending at point (d), the hysteresis loop provides more information. It is important to note that as opposed to the curves illustrated in Figure 2.1, the magnetization curves of ferro- and ferrimagnetic materials will exhibit orders of magnitude larger magnetization for small applied fields. Hence, both the susceptibility

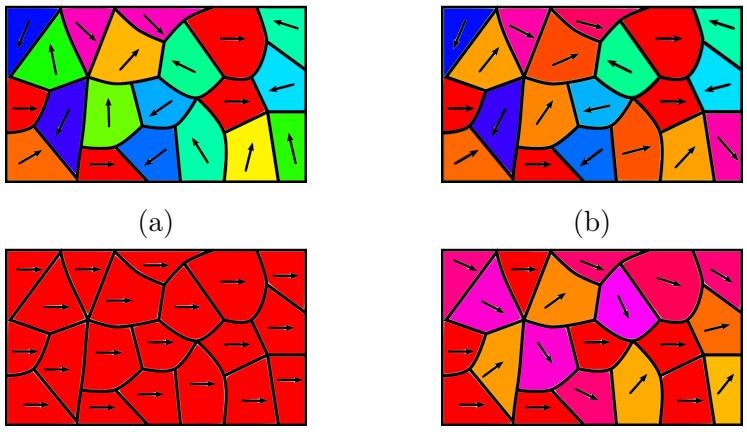


Figure 2.4: Illustrations of the magnetic microstructure of a ferromagnet at points (a) through (d) in the hysteresis loop shown in Figure 2.3. In (a), the material is demagnetized. The magnetic regions point in all directions, so that the total magnetization vanishes. In (b), some additional regions have become magnetized to the right, leading to a positive net magnetization. In (c), the magnetization is completely saturated and in (d), the material has relaxed slightly to the remanent state. In a real magnetic material, the picture is more complicated, as the magnetization process would also involve deformation and motion of the different magnetic regions.

and relative permeability of such materials are large and positive. In addition, they are not constant, but are in fact dependent on $\boldsymbol{H}$. This is apparent from the saturation of the magnetization and the non-linear nature of the magnetization curve.

Another important aspect of these materials is the apparent "memory effect" of the magnetization, meaning that the current magnetization depends on whether the material has been previously exposed to a magnetic field or not, and how this field was applied. The magnetic microstructure at points (a) through (d) are shown in Figure 2.4, and illustrates the memory effect. In the demagnetized state, point (a), the material has not been exposed to any external fields of considerable strength, and the macroscopic magnetization is approximately zero. As the material is exposed to stronger fields, we see that some regions switch their direction of magnetization, illustrated in (b). Complete saturation is reached at point (c), and when the field is removed again, we end up at point (d), the remanent state, which is distinctly different from the state at point (a). In order to get back to a state of zero magnetization, a reverse field must be applied. This is called the coercive field, $\boldsymbol{H}_c$. This picture is consistent with our understanding of ferro- and ferrimagnetic materials as materials that can retain some magnetization in the absence of a field, as illustrated in Figure 2.5, making them suitable as permanent magnets. Of

course, the processes are more complex in a real material, as the mechanism of magnetization switching would also involve deformation and motion of the magnetic regions, commonly referred to as domains.

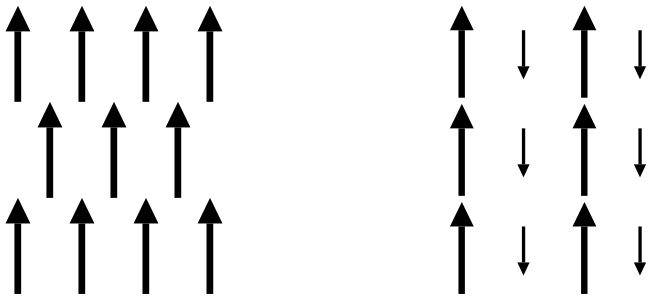


Figure 2.5: Illustrations of typical atomic spin structures of (a) a ferromagnetic material and (b) a ferrimagnetic material after they have been magnetized. Both materials have a net magnetization, even when no external field is applied.

### 2.1.4 Ferromagnetic ordering and exchange coupling

The high value of $\chi$ for ferromagnetic materials leads to long-range ordering of atomic spins. In order to explain this ordering, we need to examine the driving force behind the phenomenon. The most significant driving force responsible for atomic spin alignment is the quantum mechanical effect known as exchange coupling, which happens between neighboring spins in a material.

Exchange coupling as a phenomenon can be directly inferred from the Pauli exclusion principle, which states that no two fermions (of which electrons are a subgroup) can occupy the same quantum state of a system. A quantum state can be considered as the configuration space composed of both the orbital degree of freedom as well as the spin degree of freedom for the electrons. If two electrons have the same orbital configuration, their spins must be antiparallel, roughly leading to a net spin of zero. In the opposite case, two electrons with different orbital configurations can have parallel spins. This collective configuration would lead to nonzero net spin for the system. The exchange coupling effect arises from the fact that the configuration in which the spins are parallel lead to less Coloumbic repulsion between the electrons (since they do not possess the same orbital configuration), which can lower the total energy of the system, making a state with parallel spins the favored ground state of the system. This picture is of course vastly simplified compared to the complex interactions that happen in real systems, but provides

an intuitive understanding of exchange coupling. In real materials, the exchange coupling can also favor antiparallel spins, leading to antiferromagnetic ordering. The mechanisms behind these interactions are however more complex, and will not be discussed here.

### 2.1.5 Ferromagnetic domain formation

A ferromagnetic domain is a small region in a ferromagnetic material, where the magnetic dipoles are all aligned in the same direction. In a demagnetized ferromagnet, the net magnetization is zero. This happens because the net magnetization of each domain points in different directions, so that the magnetization of the entire ferromagnet vanishes. If we only considered exchange coupling as a driving force behind ferromagnetic ordering, we would expect the entire ferromagnet to consist of a single domain. Single-domain ferromagnets do in fact minimize the exchange energy, i.e. the free energy associated with the exchange coupling of the magnetic dipoles in the system. The ground state of the system will however be the state that minimizes the total free energy of the system. There is for instance a large energy cost associated with supporting a magnetic field outside the ferromagnetic material. This kind of field is known as a stray field, or sometimes as the demagnetizing field. An illustration of how domains may form is shown in Figure 2.6. For ferromagnets of macroscopic size, the ground state will typically consist of many domains, and generally not in an ordered fashion, as portrayed in the figure.

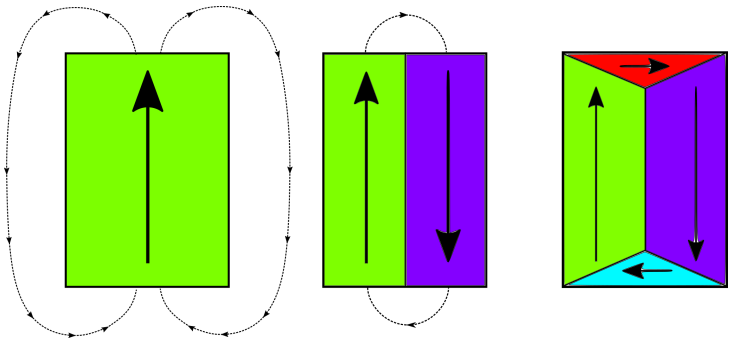

Figure 2.6: Illustrations of how domains may be formed in a ferromagnetic material in order to reduce the stray magnetic field, illustrated by the field lines outside the ferromagnet. To the left, the exchange energy is minimized by having all spins in a collinear fashion. By forming domains, as illustrated in the middle and to the right, the stray field is greatly reduced. In the flux-closed state to the right, there is hardly any stray magnetic field.

## 2.2 The micromagnetic model

### 2.2.1 The fundamental micromagnetic constraint

The micromagnetic model is a continuum model first proposed by W. F. Brown in 1959 as a successor to domain theory [12]. Brown recognized that domain theory was incomplete in the sense that it assumed magnetic domains and domain walls as fundamental concepts, not as phenomena arising from a full, self-consistent treatment of magnetism. The micromagnetic framework has not proved to be as successful as Brown hoped, due to severe mismatches between calculated properties and experimental values in early work [2]. One of the most notable failures of early work in micromagnetism was the attempt at approximating, or even ignoring, magnetostatic interactions, which are inherently long-range, and arguably the dominant energy term for many magnetic structures. The long-range nature of magnetostatic interactions means that calculating accurate values of the magnetostatic energy is a computationally expensive problem. An efficient way of doing this was not discovered until LaBonte, a student of Brown, developed an algorithm for doing this in one dimension [15] and then in two dimensions [35]. These methods can be viewed as the basis of modern micromagnetic computational algorithms.

The fundamental assumption of micromagnetism can be formulated as

$$\boldsymbol{M}(\boldsymbol{r}) = M_S \, \hat{\boldsymbol{m}}(\boldsymbol{r}), \tag{2.4}$$

i.e. that the magnetization can be expressed as a product of the saturation magnetization, $M_S$, and a continuous vector field of unit length, $\hat{\boldsymbol{m}}(\boldsymbol{r})$, often called the reduced magnetization. By modeling the magnetic structure of materials as a continuous vector field, we ignore the discrete nature of atoms, and assume that the magnetization is smooth on the atomic scale.

### 2.2.2 The Landau-Lifshitz equation

The differential equation which governs dynamical behavior of the magnetization (and hence also the reduced magnetism) is

$$\partial_t \hat{\boldsymbol{m}} = \boldsymbol{\tau}, \tag{2.5}$$

where $\hat{\boldsymbol{m}} \equiv \hat{\boldsymbol{m}}(\boldsymbol{r})$, and equivalently for $\boldsymbol{\tau}$, which is the "dimensionless torque" (units $\mathrm{s}^{-1}$). By using the following expression for $\boldsymbol{\tau}$, we recover the equation known as the

Landau-Lifshitz (LL) equation [36, 55]. The expression for the torque can be formulated as

$$\boldsymbol{\tau} = \frac{\gamma}{1+\alpha^2}\left(\hat{\boldsymbol{m}} \times \boldsymbol{H} - \alpha\, \hat{\boldsymbol{m}} \times (\hat{\boldsymbol{m}} \times \boldsymbol{H})\right), \tag{2.6}$$

where $\boldsymbol{H} \equiv \boldsymbol{H}(\boldsymbol{r}, t)$ implicitly, $\gamma$ is the gyromagnetic ratio determining the rate of precession of the magnetic moment about the magnetic field and $\alpha$ is the dimensionless Landau-Lifshitz damping constant.

By examining Eqs. 2.5 and 2.6, we see that the rate of change of the reduced magnetization is determined by two terms. The first term is simply the torque exerted on the magnetization by the field $\boldsymbol{H}$. If there was no damping, $\alpha = 0$, the energy of the system would be constant and the magnetization would precess infinitely about $\boldsymbol{H}$ at the Larmor frequency, $\omega = \gamma|\boldsymbol{H}|$. We know that real systems will relax to a steady-state, where the magnetization follows the field, meaning that there must be some dissipation of energy. A natural way of introducing energy dissipation, is by introducing a damping torque, which must be perpendicular to both the torque exerted on the magnetization by $\boldsymbol{H}$, as well as the magnetization itself. The reason for this is that we must require the damping torque to not induce or reduce precession about $\boldsymbol{H}$, also it cannot alter the magnitude of the magnetization, hence it must be perpendicular to both. We see that this is the second term of the Landau-Lifshitz equation. The damping constant $\alpha$ must be determined empirically.

At first glance, it seems like Eq. 2.6 is too simple to capture the subtleties of magnetism at the submicron length scale, where effects like exchange coupling and magnetocrystalline anisotropy become obvious. This is however not the case, if we make the definition

$$\boldsymbol{H}(\boldsymbol{r}, t) \equiv \boldsymbol{H}_{\text{eff}}(\boldsymbol{r}, t) = -\frac{1}{\mu_0}\frac{\delta U[\hat{\boldsymbol{m}}(\boldsymbol{r}, t)]}{\delta \hat{\boldsymbol{m}}(\boldsymbol{r}, t)}, \tag{2.7}$$

where $U[\boldsymbol{m}(\boldsymbol{r}, t)]$ is the potential functional and $\boldsymbol{H}_{\text{eff}}(\boldsymbol{r}, t) \equiv \boldsymbol{H}_{\text{eff}}$ the effective field. The potential functional is related to the total free energy functional through

$$U[\boldsymbol{m}(\boldsymbol{r}, t)] = \frac{\mathrm{d}E[\hat{\boldsymbol{m}}(\boldsymbol{r}, t)]}{\mathrm{d}V}. \tag{2.8}$$

An important aspect of the effective field is that contributions arising from different physical phenomena add, meaning that the effective field is the vector sum of all the individual contributions. The reason for this is that energy adds, and differentiation is a linear operation. In the next section we will show explicit expressions for the energy contributions that make up $E[\hat{\boldsymbol{m}}(\boldsymbol{r}, t)]$. For the sake of keeping notation simple, we will just write $E$ for the total free energy.

A valid question is whether the LL equation is the only dynamical equation that describes magnetization in a material. In fact, the LL equation is universally valid. It can be shown that any first order dynamical equation for the magnetization subject to the micromagnetic constraint, Eq. 2.4, is equivalent to the LL equation [6].

### 2.2.3 Total energy and the effective field

In the previous section, we defined the total energy functional, and its relation to the effective field. The total energy is composed of the following contributions.

- $E_{\text{ext}}$, the energy of the external, applied field, also called the Zeeman energy.
- $E_{\text{demag}}$, the magnetostatic energy, also called demagnetization energy.
- $E_{\text{exch}}$, the exchange energy.
- $E_{\text{anis}}$, the magnetocrystalline anisotropy energy.
- $E_{\text{thermal}}$, the thermal energy.

#### 2.2.3.1 External energy

The external energy is simply the interaction energy between an external, applied field, $\boldsymbol{H}_{\text{ext}}$, and the magnetization, $\boldsymbol{M} = M_S\,\hat{\boldsymbol{m}}$. It is given by

$$E_{\text{ext}} = -\mu_0 M_S \int_V \hat{\boldsymbol{m}} \cdot \boldsymbol{H}_{\text{ext}}\,\mathrm{d}V. \tag{2.9}$$

The integral is carried out over the volume element $V$.

#### 2.2.3.2 Magnetostatic energy

A monodomain ferromagnet will have a macroscopic magnetization, which leads to the formation of a magnetic field outside (and inside) the ferromagnet. This field is often called the demagnetizing field or stray magnetic field, $\boldsymbol{H}_{\text{d}}$, due to the fact that this field opposes the magnetization inside the ferromagnet. For this reason, the magnetostatic energy is sometimes referred to as demagnetization energy. Supporting a large magnetic field outside the ferromagnet is associated with high magnetostatic energy stored in the ferromagnetic sample. Hence, formation of domains in order to minimize $\boldsymbol{H}_{\text{d}}$ leads to a minimization of the magnetostatic energy. Of course, introducing domains increases the

exchange energy. The formation of domains can therefore be considered as a competition between exchange and magnetostatic energy minimization.

An explicit expression for the magnetostatic energy can be written as

$$E_{\text{demag}} = -\frac{\mu_0 M_S}{2} \int_V \hat{\boldsymbol{m}} \cdot \boldsymbol{H}_{\text{d}} \, \mathrm{d}V. \tag{2.10}$$

One of the effects of magnetostatic energy minimization is the phenomenon known as shape anisotropy, where the lowest energy magnetic configuration is directly related to the shape of the magnetic material. Consider a ferromagnetic nanowire. By having the magnetization of the nanowire aligned with the long axis of the wire, the stray field is greatly reduced. If the magnetization instead was perpendicular to the long axis, the stray field would be much larger. Generally, the effect of shape anisotropy is a perceived uniaxial magnetic anisotropy which favors magnetic alignment along the largest dimension of the ferromagnet. The effect is however entirely accounted for by the demagnetization energy.

#### 2.2.3.3 Exchange energy

As mentioned above, exchange coupling is an important effect responsible for ferromagnetic ordering. The exchange energy is minimized when all magnetic dipoles point the same way. Conversely, by having domains with different magnetization, the exchange energy of the system is raised. The expression for the exchange energy is given by

$$E_{\text{exch}} = -\frac{\mu_0 M_S}{2} \int_V \hat{\boldsymbol{m}} \cdot \boldsymbol{H}_{\text{exch}} \, \mathrm{d}V, \tag{2.11}$$

where

$$\boldsymbol{H}_{\text{exch}} = \frac{2A_{\text{ex}}}{M_S^2} \nabla^2 \hat{\boldsymbol{m}}. \tag{2.12}$$

$A_{\text{ex}}$ is known as the exchange stiffness, where $A_{\text{ex}} > 0$ signifies that neighboring spins want to align. The units of $A_{\text{ex}}$ are J/m.

#### 2.2.3.4 Magnetocrystalline energy

In ferromagnetic crystals, magnetization tends to align along certain crystallographic directions, known as the easy axes. The least favorable crystallographic directions are conversely named the hard axes. This effect can be contributed to the spin-orbit interaction, which couples the electronic spin to the orbit of the electron. The orbit is of

course coupled to the atomic nuclei, which make up the crystal lattice. Different crystal structures will often exhibit different easy and hard axes.

The most simple form for magnetocrystalline anisotropy is called uniaxial anisotropy. Such systems have a single axis of high symmetry, along which the magnetization would prefer to align. The anisotropy energy of such a system can be expressed to the first order as

$$E_{\text{anis}} = \int_V K_{\text{u1}} \sin^2 \theta \, \mathrm{d}V, \tag{2.13}$$

where $\theta$ is the polar angle between the easy axis and the magnetization, and $K_{\text{u1}}$ is the first order uniaxial magnetocrystalline anisotropy constant.

More complex magnetocrystalline anisotropy exists, for instance the biaxial magnetocrystalline anisotropy exhibited by thin films of LSMO. In such systems there can be several easy axes and hard axes. For LSMO, the easy axes are the $\langle 110 \rangle$-directions and the hard axes the $\langle 100 \rangle$-directions.

#### 2.2.3.5 Thermal energy

The thermal energy is usually defined as $E_{\text{thermal}} = k_B T$, where $k_B$ is the Boltzmann constant and $T$ the temperature. It is however difficult to incorporate thermal excitation in simulations, as the effect of temperature is inherently random. Instead, $E_{\text{thermal}}$ can be used as a reference in order to assess the relative magnitude of the other energies that comprise the total free energy of the system.

## 2.3 Supermagnetism

### 2.3.1 The basics of supermagnetism

Supermagnetism as a phenomenon refers to collective magnetic ordering of ensembles of magnetic structures or particles that are in a state called the superparamagnetic state.

Before we define the different classes of supermagnetic ordering, it is instructive to examine superparamagnetism closer. The fact that when ferromagnetic particles become sufficiently small, they become monodomain was first predicted in 1930 by Frenkel and

Dorfman [5], and further explored analytically by Kittel [30] and Brown [14]. Below the critical size the particle does indeed have ferromagnetic ordering, thus behaving like a single spin, a superspin, which is orders of magnitude larger than a single atomic spin. The particle is said to be superparamagnetic if the thermal energy is sufficient to switch the direction of magnetization, i.e. the direction of the superspin. If the particle exhibits magnetic anisotropy, the thermal energy must be sufficiently large to overcome the energy barrier associated with switching the magnetization.

### 2.3.2 Supermagnetic ordering

When two superparamagnetic particles are brought in proximity of each other, they will experience the dipole-dipole interactions between themselves. The potential energy of two magnetic dipoles $\boldsymbol{m}_1$ and $\boldsymbol{m}_2$ (not to be confused with the reduced magnetization $\hat{\boldsymbol{m}}$) separated by a distance vector $\boldsymbol{r}$ [5] is given by

$$E_{\text{dipole}} = \frac{\mu_0}{4\pi r^3}\left(\boldsymbol{m}_1 \cdot \boldsymbol{m}_2 - \frac{3}{r^2}(\boldsymbol{m}_1 \cdot \boldsymbol{r})(\boldsymbol{m}_2 \cdot \boldsymbol{r})\right). \tag{2.14}$$

By inspection, we see that the dipolar interaction is both long range and inherently anisotropic. It is this interaction that is responsible for supermagnetic ordering, assuming that the superparamagnetic particles are sufficiently separated so that exchange coupling can be ignored. When the dipole-dipole interactions become significant, an ensemble of superparamagnetic particles may form collective, "frozen" states [18]. The three collectively ordered phases are called the superferromagnetic (SFM) state, the superantiferromagnetic (SAF) state and the superspin-glass (SSG) state. The SFM and SAF states are both characterized by certain, specific magnetic order, whereas the SSG state is related to disorder, frustration and randomness.

### 2.3.3 Superspin-glass

The SSG state, while not ordered, is characterized by a collective freezing of the superspins in the ensemble, at a distinct temperature, known as the glass temperature $T_g$. Each superspin in the superparamagnetic particle ensemble becomes increasingly aware of its neighboring superspins as the temperature approaches $T_g$, and at $T_g$ the fluctuations in the superspin structure of the ensemble come to a halt. This marks the transition into the SSG regime. The fluctuations above $T_g$ were a consequence of e.g. finite temperature, and the transition into the SSG phase marks where the interparticle interactions begin to

dominate over random external and internal perturbations. An illustration of a possible SSG configuration is shown in Figure 2.7. Interestingly, the transition (or relaxation) into the SSG phase takes place asymptotically, and temperature changes below $T_g$ also induce changes in the superspin structure. These changes also happen asymptotically. This gives rise to the memory effect upon aging, i.e. that the superspin structure changes as it is aged, due to the slow relaxation dynamics [38]. This effect is often taken as evidence of spin glass behavior.

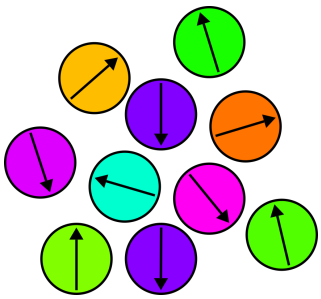

Figure 2.7: An illustration of the SSG phase. The superspin structure is chaotic and frustrated.

A prerequisite for obtaining the SSG state is the possibility of frustrated disorder in the system. One way of obtaining this is by having randomly distributed superspins [42]. If the superspins are regularly distributed in e.g. a 2D lattice, the stacking must allow multiple metastable superspin structures, leading to frustration, otherwise other collective states like the SFM or SAF states might be realized instead.

### 2.3.4 Superferromagnetism and superantiferromagnetism

The SFM state is an ordered state. The ensemble of superspins collectively form one or more ferromagnetically ordered domains, similar to the way atomic spins align in ordinary ferromagnetic materials. An important difference is that magnetic ordering between superspins will be induced by the dipole-dipole interaction, not the exchange interaction (assuming sufficient spacing between superspins). According to Bedanta [5], SFM order requires stronger inter-particle interaction than SSG systems.

For a 2D lattice of superspins, the dipole-dipole interaction does not generally lead to SFM ordering. For disordered 2D lattices, SSG behavior may arise. For infinite ordered 2D dipole lattices, lattices with sixfold symmetry are expected to have a uniform SFM ground state [50, 47], whereas lattices with fourfold symmetry should have zero net magnetization in the ground state. In fact, the vast majority of rhombic dipole lattices (of which the

square and hexagonal ones are special cases) have been shown to form SFM ordered ground states [23]. For finite lattices, the expected ground state is non-uniform, i.e. with for instance domains and vortices. In some cases, SFM ordering may also exist as a metastable state in lattices that should generally present SAF ordering, and vice versa [23, 31]. The SAF state is similar to an ordinary antiferromagnetic state, where the atomic spins are replaced by the superspins. SAF domains are defined as regions of the superspin lattice that exhibit perfect AF ordering. Both SFM and SAF ordering are illustrated in Figure 2.8.

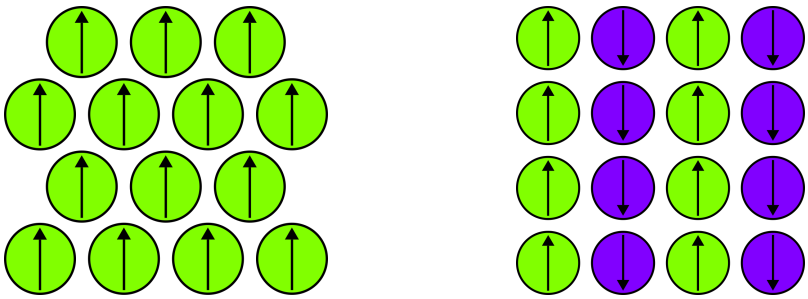

(a) (b)

Figure 2.8: The figure shows illustrations of typical superspin structures of (a) a SFM ordered array and (b) a SAF ordered array. Each circle represents a superparamagnetic particle, acting as a superspin. Typical dimensions of each particle is 1 nm to 100 nm.

Due to the exchange decoupling between superspins, the domain structure of SFM and SAF lattices is expected to be different from the domain structure found in regular ferromagnetic or antiferromagnetic materials. Recalling that exchange coupling is one of the most significant driving forces behind domain formation, and responsible for extended domain walls, we expect domains in SFM and SAF materials to be comparatively smaller than in FM and AF materials, with more abrupt domain walls [64, 63, 26].

Most theoretical work on supermagnetism, more specifically on dipolar lattices, only treats highly idealized systems. In order to further elcudiate how supermagnetism may be manifest in realistic systems, use of the micromagnetic model in conjunction with numerical approaches is warranted.

# Chapter 3

# Modeling and simulations

This chapter focuses on the practicalities of micromagnetic simulations, and some of the specifics of the simulations carried out as part of this work. Section 3.1 outlines different approaches to micromagnetic simulations, as well as some considerations that must be taken. In Section 3.2, we will describe the specific software used to carry out simulations. The model system will be described in Section 3.3. Finally, in Section 3.4, we discuss some of the universal simulation considerations that applied to all our simulations. We emphasize that specific details relating to the individual simulations will be presented in conjunction with results and discussion in Chapters 4 and 5.

## 3.1 Micromagnetic simulations

The Landau-Lifshitz equation, Eqs. 2.5 and 2.6, can only be solved analytically for a limited number of systems [28, 39, 8]. In order to explore realistic systems, the equation must be solved numerically.

One of the most common ways of numerically evaluating the LL equation is through the use of the finite-difference method. In this approach, the system of interest is spatially discretized in a 2D (or 3D) array of cells. The underlying assumption is that the magnetization is uniform in each cell. This assumption leads to a coupled set of ordinary differential equations that can be numerically integrated using appropriate time-stepping techniques. The alternative approach is the finite-element method, which offers greater flexibility, but is more computationally expensive.

In order to ensure that the magnetization can indeed be assumed uniform in the discretization cells, one must assure that the spatial dimensions of the cell are sufficiently

small. In order to determine a reasonable threshold for the cell size, we use the exchange length. The exchange length, $l_{\text{ex}}$, measures the relative strength of the exchange and demagnetizing energies [1]. For length scales smaller than $l_{\text{ex}}$, the exchange energy dominates, so that magnetization can be assumed uniform. The exchange length is defined as

$$l_{\text{ex}} = \sqrt{\frac{2A_{\text{ex}}}{\mu_0 M_S^2}}. \tag{3.1}$$

By keeping the cell size smaller than $l_{\text{ex}}$, the underlying assumption holds.

It is important that the finite-difference scheme utilized preserves the magnetization magnitude, as this is the fundamental micromagnetic constraint. This can be achieved through choosing appropriate numerical integration schemes [7].

In this work, simulations were carried out using MuMax3 [62], an open-source GPU-accelerated micromagnetic simulation program, developed by the DyNaMat group of Prof. Van Waeyenberge at Ghent University. GPU computing offers a speed-up of approximately two orders of magnitude compared to CPU-based simulations, enabling simulations of larger and more complex systems without the use of a supercomputer. These advances have opened up the possibility of efficiently exploring and simulating the magnetic microstructure of magnetic materials at length scales that are also experimentally available.

## 3.2 MuMax3

MuMax3 uses the finite-difference method, as described in Section 3.1, to model the magnetization dynamics of a specified system. The geometry of the system is discretized into a 2D (or 3D) mesh of orthorhombic cells. The program uses material regions in order to limit memory usage. This means that each cell is assigned to a region, with its own specific material parameters. Up to 257 different regions can be defined, providing great flexibility. Geometries are defined through the "Constructive Solid Geometry"-method, where basic shapes like ellipsoids and cuboids are used, together with translation, rotation, scaling and boolean combination.

The type of material that is modeled is realized through the material parameters shown in Table 3.1. As before-mentioned, different material regions can have different material parameters so that systems consisting of different materials can be modeled.

When doing energy minimization problems (i.e. finding magnetic ground state config-

Table 3.1: The table shows the material parameters used in MuMax3 to define the type of material being modeled.

| Material parameter | Symbol | Units |
|---|---|---|
| Exchange stiffness | $A_{\text{ex}}$ | J/m |
| Saturation magnetization | $M_S$ | A/m |
| Landau-Lifshitz damping constant | $\alpha$ | 1 |
| Uniaxial anisotropy constant | $K_{\text{u1}}$ | J/m$^3$ |
| Cubic anisotropy constant | $K_{\text{c1}}$ | J/m$^3$ |
| Uniaxial anisotropy direction | $\boldsymbol{U}$ | 1 |
| Cubic anisotropy directions | $\boldsymbol{C}_1$ & $\boldsymbol{C}_2$ | 1 |

urations), the value of $\alpha$ is unimportant, as damping only affects the dynamics of the system. The values of the anisotropy constants are defined so that $K_{\text{u1}}, K_{\text{c1}} > 0$ leads to $\boldsymbol{U}$, $\boldsymbol{C}_1$, $\boldsymbol{C}_2$ and $\boldsymbol{C}_1 \times \boldsymbol{C}_2$ being easy axes, while the opposite leads to the axes being hard axes.

The cell size must be defined in all three spatial directions. We generally use the exchange length, Eq. 3.1, as upper bound for the cell size. Since there must be an integer number of cells in every direction, the cell size may deviate from the exchange length, in which case one should choose a smaller cell size than the exchange length. In addition, MuMax3 has been shown to run significantly faster when the number of cells in every direction is a power-of-two integer. Hence, for large simulations, it may be beneficial to use smaller cell dimensions in order have a power-of-two number of cells in every direction.

For the case of 2D simulations of e.g. thin films, it is common to use the exchange length as guide for cell size for the in-plane dimensions, while setting the number of cells in the out-of-plane dimension to one. By doing this, we assume the magnetization to be constant in the out-of-plane dimension. This assumption is based on the fact that the out-of-plane magnetization of thin films is generally close to zero, due to the very large demagnetizing field created by having out-of-plane magnetization [55]. In such cases, using an out-of-plane cell size larger than the exchange length can be justified, and is the conventional way of simulating thin films.

One of the problems of micromagnetic simulations is implementing finite temperature. Although MuMax3 has a module to emulate temperature, through a stochastically varying thermal field based on work by Brown [13], this module will often in practice lead to convergence problems when doing energy minimizations. Therefore, the most common

way to simulate different temperatures, at least when energy minimization is concerned, is by tuning the material parameters.

The results of simulations can be saved in tabular format, in which case spatial averages are saved. Quantities such as average magnetization, energy densities, effective field, magnetic torque and error estimates are readily available as output parameters. In addition, spatially varying output quantities such as the magnetization profile can be saved in the "OVF" data format, and converted to image format. An example is shown in Figure 3.1.

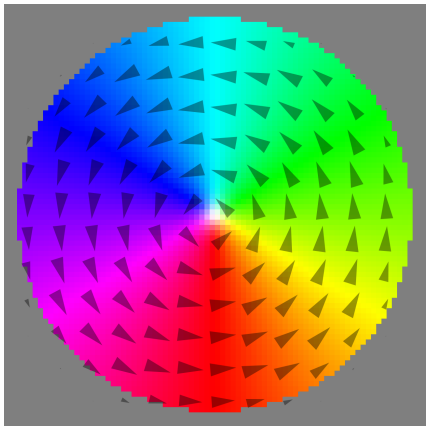

Figure 3.1: An example of how output images from MuMax3 looks. This structure is a circular disk of LSMO, with diameter 150 nm and thickness 10 nm. The structure exhibits the characteristic vortex ground state, a fully flux-closed magnetic profile. The arrows and color profile indicate the direction of magnetization. The gray areas outside the circular magnet are non-magnetic.

As can be seen in Figure 3.1, the circular shape has step-like edges, which is a result of the fact that each discretization cell belongs to a single material region. These discrete edges would lead to issues when structures are sufficiently small, if it was not for the possibility to introduce edge smoothing. MuMax3 allows the user to control volume sampling in each cell, so that the volume of structures such as this circle is accurately calculated, even if edges appear jagged. This means that energy densities are accurately calculated, so that the effective field is correct. In this project, we used the value 3 for the edge smoothing variable. This means that each cell was sampled $2^3 = 8$ times in order to determine the volume of the magnetic region.

## 3.3 The model system

In this work, we have explored magnetism in patterned (100)-oriented thin films of LSMO using micromagnetic simulations as our tool. LSMO is a half-metallic oxide, with a bulk Curie temperature around 380 K, and can be grown in thin films using e.g. pulsed-laser deposition (PLD) [49]. Experiments on epitaxial thin films of LSMO have shown that the magnetic anisotropy is dominated by stress effects at room temperature [54], with biaxial easy axes in the $\langle 110 \rangle$-directions and hard axes in the $\langle 100 \rangle$-directions. The system has been modeled as 2D, as described in the previous section.

Patterning of LSMO thin films can be achieved through the use of electron beam lithography in combination with ion implantation [57], so that ferromagnetic nanometer-sized LSMO islands can be formed, embedded in a paramagnetic LSMO matrix. This method allows for vastly different geometries and high precision, and is made possible because the magnetic properties of LSMO are so interconnected with the atomic structure of the material.

### 3.3.1 Material parameters

As shown in Table 3.1, only a few parameters are needed in order to carry out micromagnetic simulations. Since LSMO thin films exhibit biaxial magnetic anisotropy, the uniaxial anisotropy constant as well as direction can be set to zero. This leaves only five parameters needed to accurately simulate our model system. Of these five parameters, two are temperature dependent, namely $M_S$ and $K_{c1}$.

When doing energy minimization, the value of $\alpha$, the Landau-Lifshitz damping constant, is unimportant, since this constant only governs the dynamical behavior of the system. The value used for the temperature-independent exchange stiffness was $1.7 \times 10^{-12}$ J/m. The values of $M_S$ and $K_{c1}$ were chosen according to Figures 3.2 and 3.3 respectively, and the values of $K_{c1}$ were chosen based on the blue curve in Figure 3.3. For temperatures above the range of the data portrayed in the graph, $K_{c1}$ was chosen to be $100\,\mathrm{J/m^3}$. For temperatures below 50 K, $M_S$ was fixed at 600 kA/m.

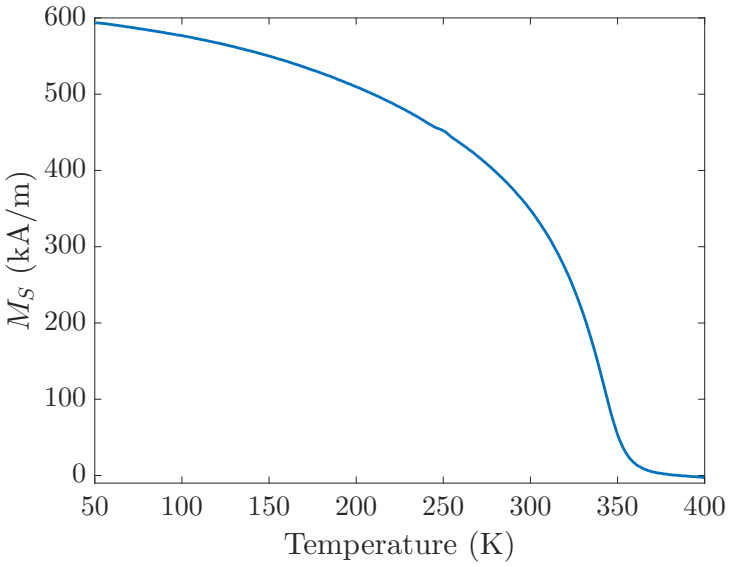


Figure 3.2: The figure shows the value of $M_S$ for a thin film of LSMO as function of temperature, as measured on a Versalab vibrating sample magnetometer.

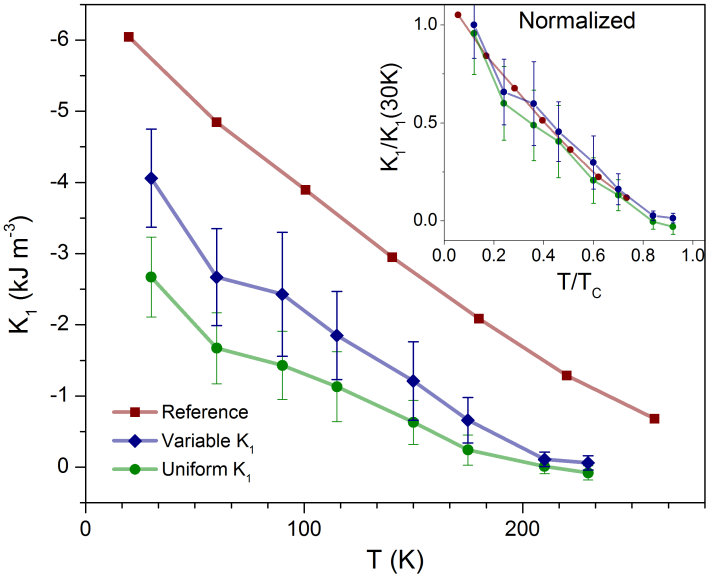


Figure 3.3: The figure shows the value of $K_{c1}$ for a thin film of LSMO as function of temperature. The anisotropy constant was measured along the [100]-direction. The graph is taken from work by Lee et. al [37]. For this work, the blue line was chosen as reference.

## 3.4 Simulation procedures

In this work, we have only been concerned with energy minimization problems, hence no dynamical simulations were carried out. When performing energy minimizations to find magnetic ground states, the general approach can be summarized as follows.

- Define the system by choosing appropriate material parameters and geometry.
- Initialize the system to the wanted magnetic configuration. We often choose a random configuration, which is the simulation equivalent of raising the temperature above the Curie temperature in an experiment. Other choices include magnetically saturated states, or more complicated magnetic configurations.
- Run a numerical scheme to identify the magnetic configuration that minimizes the free energy of the system.

Modern simulation software, such as MuMax3, is extremely well suited for such simulations, and can accurately calculate magnetic properties of a plethora of systems with high accuracy [62]. Care must however be taken when considering systems with complex magnetic free energy landscapes. Patterned thin films of LSMO are expected to belong to this class of systems. They are characterized by non-uniqueness of magnetic ground states, or equivalently, a free energy landscape dominated by many local minima, so that the final configuration depends on the road taken. In order to ensure that the simulated results are as accurate as possible, some precautionary steps can be taken.

Firstly, ensuring that simulation grid size was sufficiently large, or equivalently that the simulation cell size was sufficiently small, was important. This consideration was not unique to systems with complex free energy landscapes, but was indeed universal, and nonetheless very important. The exchange length should be used as upper bound for the cell size. Using Eq. 3.1, together with the material parameters of LSMO, as given in Section 3.3.1, the calculated value of $l_{\text{ex}}$ for LSMO ranged from 2.7 nm at temperatures below 25 K to approximately 4.7 nm at room temperature. Hence, we decided to set the upper bound for the cell size (regardless of temperature) to 2.0 nm. The grid sizes were in general chosen to be a power-of-two integer in all spatial directions, due to performance considerations.

The second consideration was more specific to the systems of interest in this work. The process of energy minimization from random configurations is designed to mimic the experimental method of heating the magnetic material to enter the paramagnetic regime, followed by cooling, so that the true magnetic ground state can be found. The reason is of course the intrinsic irreversibility of magnetic systems (i.e. the memory effect previously mentioned). When doing simulations it may therefore be worthwhile to try and emulate realistic cooling processes, to ensure that the results are as realistic as possible. The specific way we implemented this relaxation process was through step-wise energy minimizations. The magnetic ground state of the simulated systems were hence identi-

fied by allowing the system to relax at decreasing temperatures, until the wanted ground state was found. In practice, this meant tuning the saturation magnetization and magnetocrystalline anisotropy constant for each step. This method of identifying the magnetic ground state will later be referred to as *temperature relaxation*. The opposite approach is to tune the magnetic properties to emulate the exact temperature that is wanted, and perform an energy minimization directly from a random configuration. In experimental terms, this would be equivalent to a very fast quenching of the magnetic material, hence we will refer to the procedure as *quenched relaxation*.

# Chapter 4

# Magnetic properties of single LSMO nanomagnets

In this chapter, we will investigate the magnetic properties of single LSMO nanomagnets. As before-mentioned, a prerequisite for supermagnetism being manifest in a system, is superparamagnetism. Hence, the aim is to identify the size range where thin structures of LSMO exhibit superparamagnetism. In Section 4.1, we will give a thorough description of the simulations that were carried out on single LSMO nanomagnets. The results will be presented and discussed in Section 4.2. A summary of the most important findings of this chapter is given in Section 4.3.

## 4.1 Simulating single LSMO nanomagnets

The starting point of our investigations was determining the size range for which nanometer-sized magnets of LSMO exhibit superparamagnetic behavior. In order to eliminate any magnetic shape anisotropy effects, the geometry was chosen to be circular, as shown in Figure 4.1. The magnets were aligned so that the easy axes were in the horizontal and vertical directions. The thickness of the circular nanomagnets was determined by the chosen film thickness.

Our chosen film thicknesses were 5 nm, 10 nm and 15 nm, with diameters in the range 20 nm to 150 nm with increments of 10 nm. These dimensions were chosen because they are in the range of typical sizes that are possible to fabricate using e.g. PLD for film growth and state-of-the-art electron beam lithography for patterning. The nanomagnets were simulated using material parameters corresponding to two different temperatures,

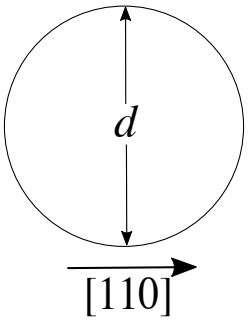


Figure 4.1: The figure illustrates the geometry chosen to investigate the superparamagnetic size range of LSMO nanomagnets. The ⟨110⟩-directions are the easy axes of the magnet, with [110] as shown by the arrow.

50 K and 300 K. The simulation cell sizes were chosen to be 2 nm for both the in-plane dimensions.

In order to ensure that the ground states of the magnets of each size were accurately identified, we initialized the magnet to a random configuration (i.e. a configuration where the magnetization of each cell points in a random direction) and relaxed it 50 times for each size. Temperature relaxation, as described in Section 3.4, was the method of choice.

In order to quantify whether the final magnetic configuration was monodomain, polydomain or a vortex (flux-closed) state, we used the absolute average reduced magnetization of the magnetic region. Recalling that the reduced magnetization is the unit vector field that describes the magnetic microstructure, a perfect monodomain particle would show $|\langle \hat{\boldsymbol{m}} \rangle| = 1$, whereas a perfect vortex state would show $|\langle \hat{\boldsymbol{m}} \rangle| \simeq 0$. To allow for some imperfection, we chose $|\langle \hat{\boldsymbol{m}} \rangle| \geq 0.95$ as the threshold for classifying a particle as monodomain. Conversely, the limit $|\langle \hat{\boldsymbol{m}} \rangle| \leq 0.05$ was chosen as the threshold for a vortex ground state. Any particles falling outside both regimes were classified as polydomain.

## 4.2 Results and discussion

### 4.2.1 The magnetic ground states of single LSMO nanomagnets

After simulating single LSMO nanomagnets at different thicknesses, diameters and temperatures, we wanted to identify the typical magnetic ground states. The most prevalent magnetic ground states of single LSMO nanomagnets were by far the monodomain and vortex ground states. The monodomain ground state was typically the most stable for

thin magnets, and below some critical diameter, where exchange interactions dominated over the magnetostatic forces. The vortex ground state was more often observed for thicker magnets and at larger diameters.

In addition, we found two polydomain ground states that typically showed up in transition regimes between monodomain and vortex ground states. These were the "edge vortex" and "S-shape" ground states. Examples of all four ground states are shown in Figure 4.2. At 300 K, only the monodomain and vortex ground states were present, except for one case of the edge vortex state. The reason for this was most likely that the magnetocrystalline anisotropy was very low at room temperature, and that the two polydomain ground states were results of competition between magnetocrystalline anisotropy and exchange interaction, whom most likely favored monodomain ground states, and the magnetostatic energy, which favored a vortex state. Typical values of absolute average reduced magnetization were in the range $|\langle \hat{\boldsymbol{m}} \rangle| \gtrsim 0.95$ for the monodomain state, $|\langle \hat{\boldsymbol{m}} \rangle| \lesssim 0.05$ for the vortex state, $|\langle \hat{\boldsymbol{m}} \rangle| \sim 0.6$ for the edge vortex state and $|\langle \hat{\boldsymbol{m}} \rangle| \sim 0.8$ for the S-shape state, but there were exceptions.

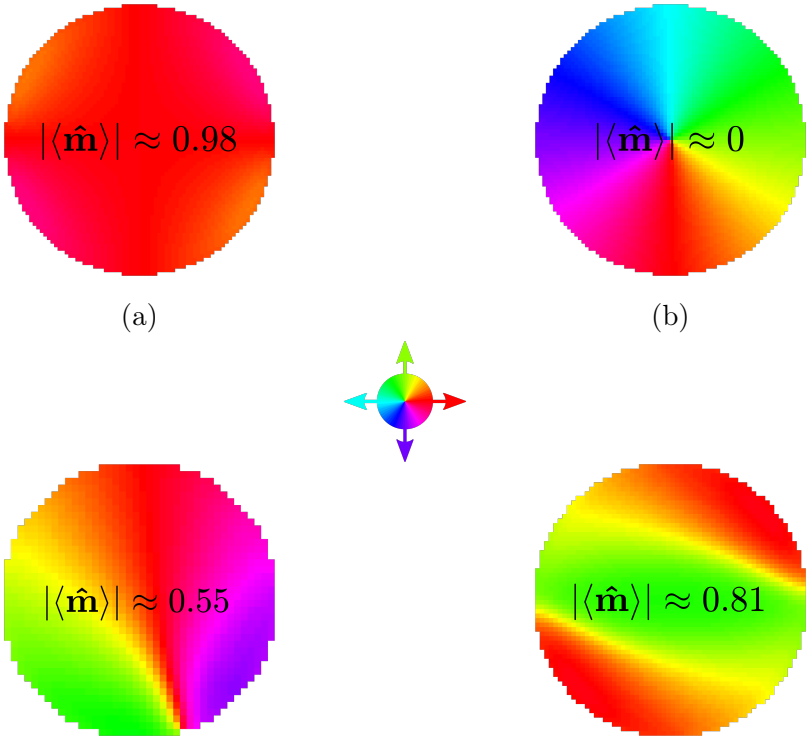


Figure 4.2: Examples of (a) the monodomain ground state, (b) the vortex ground state, (c) the edge vortex ground state and (d) the S-shape ground state. The absolute average reduced magnetization is noted on each ground state. The direction of magnetization is given by the color legend in the middle.

### 4.2.2 Probability of monodomain ground state

A total of 4200 energy minimizations were carried out in order to explore the parameter range where single LSMO nanomagnets exhibited superparamagnetism. A prerequisite for superparamagnetic behavior was of course that the magnetic ground state was the monodomain state. In order to estimate the probability of having a monodomain ground state, we plotted the fraction of monodomain ground states to the total number of simulations for each size, thickness and temperature. The results for $T = 50\,\mathrm{K}$ are given in Figure 4.3a, whereas the results for $T = 300\,\mathrm{K}$ are shown in Figure 4.3b.

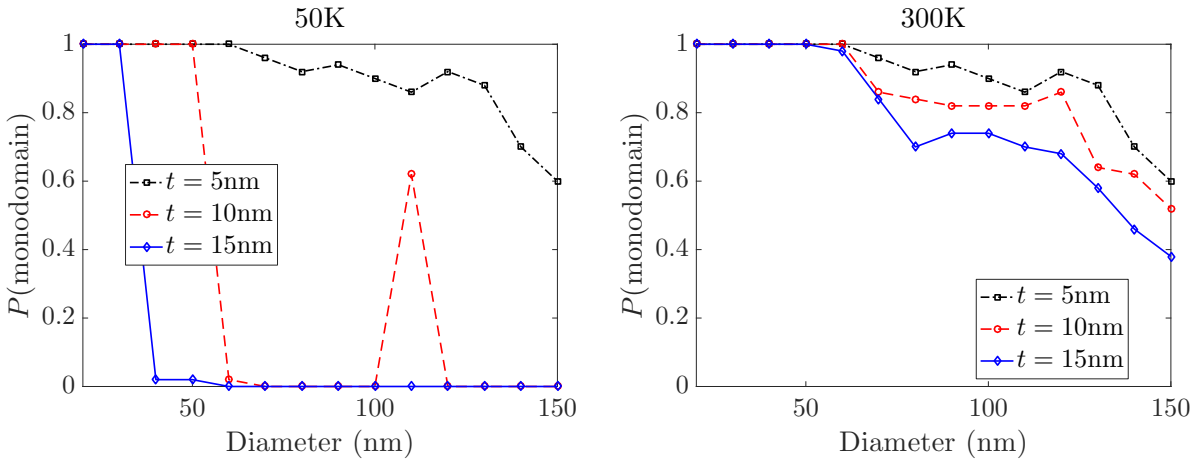


Figure 4.3: The fraction of circular nanomagnets that exhibited monodomain ground state at (a) 50 K and (b) 300 K. A total of 50 simulations were run for each diameter and thickness $t$.

In general, we saw that the probability of obtaining a monodomain ground state increased as both the thickness and diameter of the nanomagnets decreased. This was as expected, since smaller dimensions of the nanomagnet lead to the exchange interaction and possibly the magnetocrystalline anisotropy dominating over the demagnetizing contribution to the free energy of the system. The results for 50 K, Figure 4.3a, did show a peculiar peak for $t = 10\,\mathrm{nm}$, in addition to abrupt transitions from approximately 100% monodomain ground state to approximately 0%. This was due to formation of polydomain ground states. At a diameter of 110 nm, the monodomain state was stable again, leading to a large fraction of monodomain ground states. This particular ground state was however in a critical regime between a monodomain and polydomain state, or a quasi-monodomain state. One possible explanation was that the magnetic free energy landscape of such nanomagnets is very sensitive to change in size, due to the complex and dynamic interactions of the magnetocrystalline anisotropy, exchange interaction and magnetostatic

energy at this length scale. A small increase in monodomain ground states was also observed at diameters of 110 nm to 120 nm at 300K for the 10nm thick nanomagnets. This peak may have been caused by the same effects that were responsible for the peak observed at 50K.

It was interesting that for $t = 5$ nm, the fraction of monodomain ground states was very similar for both temperatures. It was likely that at this thickness, the exchange interaction dominated over the magnetocrystalline anisotropy and magnetostatic self-interaction, so that formation of polydomain ground states was suppressed.

### 4.2.3 The free energy of different ground states

In order to assess which magnetic ground state was the most stable, we also made plots of average free energy density versus diameter for the different thicknesses and temperatures. It was not given that the individual ground states found by MuMax were indeed the most stable ones. It was possible that the some of the ground states were metastable ones, and by comparing energy densities, we could identify the most energetically favorable ground state. The results for a thickness of 5 nm at 50 K and 300 K are shown in Figures 4.4a and 4.4b respectively. Similar plots for thicknesses of 10 nm and 15 nm can be found in Appendix B.1. The reason for only emphasizing the results for the 5 nm case, was that this thickness exhibited the largest range of diameters where the monodomain ground state was the most stable.

We saw that at 50 K, the critical diameter of the nanomagnets was around 60 nm to 70 nm. The critical diameter referred to the diameter at which the energy density of the monodomain ground state was equal to either the vortex or polydomain ground states. By choosing a thickness of 5 nm, the monodomain ground state was the most energetically favorable for dimensions up to approximately 120 nm at 300 K. Keeping the magnets thin seemed to favor formation of monodomain ground states throughout the entire range of temperatures we explored.

### 4.2.4 Identifying the dominant magnetic interactions

The total free energy density is a useful quantity for assessing which ground states were the most stable ones, but in order to determine which magnetic effects were the dominant ones for the different ground states, we looked closer at the different contributions to the free energy density. For single nanomagnets in zero applied field, the free energy is

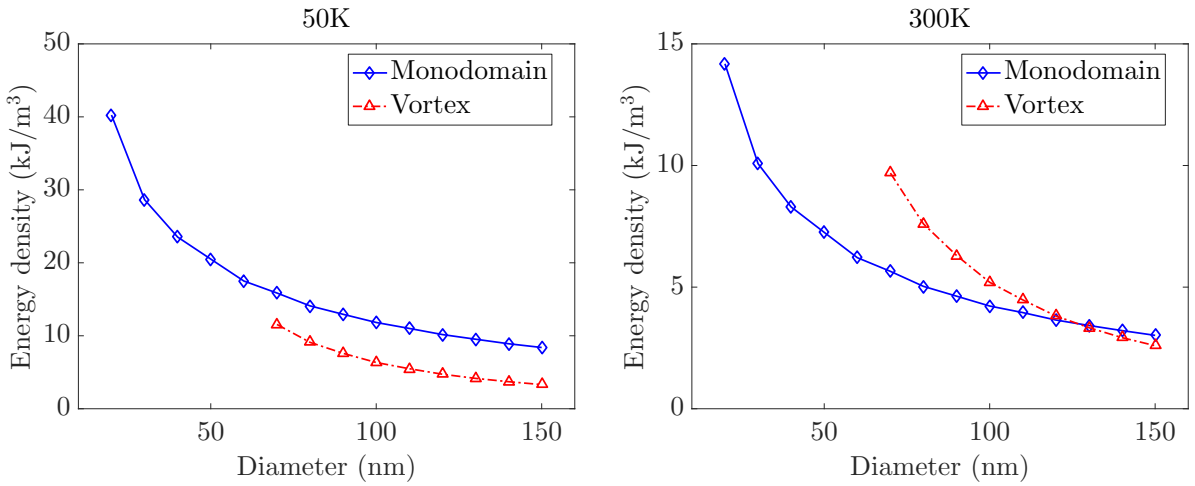


(a) (b)

Figure 4.4: Average energy density of circular LSMO nanomagnets grouped after type of ground state. The thickness of the nanomagnets was 5 nm and the temperature (a) 50 K and (b) 300 K. The reason for the average energy density of the vortex state not being plotted below a diameter of 70 nm in (a) and (b) was that only monodomain ground states were present.

composed of $E_{\text{demag}}$, $E_{\text{anis}}$ and $E_{\text{exch}}$, as described in Section 2.2.3. The relative free energy densities were defined as $\mathcal{E}_i = E_i/E_{\text{total}}$, $i$ = demag, anis or exch, so that $\sum_i \mathcal{E}_i = 1$.

The different free energy contributions are shown in Table 4.1 for 50 K and 300 K. The idea behind this approach was that the composition of the free energy density of the magnetic ground states would show which of the magnetic effects were the most important for the formation of the specific ground state. Since the different effects scale differently with both size and temperature, the evolution of their relative strengths was expected to be non-trivial.

Starting at 50 K in Table 4.1, we saw that the free energy of the monodomain ground state was almost only composed of the demagnetization free energy for all thicknesses. The contributions from magnetocrystalline anisotropy and exchange interactions were very small in comparison, which meant that these effects were dominant for the formation of the monodomain ground state. This could be inferred from the fact that both exchange and anisotropy free energy had been minimized, meaning that the effective fields created by these effects were comparatively stronger than the demagnetizing field. The free energy of the polydomain ground state showed a somewhat more even distribution between demagnetization and exchange free energy, as well as minor contributions from the magnetocrystalline anisotropy. This was in accord with the type of polydomain ground state

Table 4.1: The average relative free energy density contributions of all single LSMO nanomagnets, grouped after magnet thickness and type of ground state at 50 K and 300 K. The relative energy density contributions were calculated by normalizing the different free energy densities to total energy density for each individual simulation. N/A meant that there were no occurrences of the particular ground state.

| | | 50 K | | | 300 K | | |
|---|---|---|---|---|---|---|---|
| Thickness (nm) | | 5 | 10 | 15 | 5 | 10 | 15 |
| Monodomain | $\mathcal{E}_{\text{demag}}$ | 0.98 | 0.99 | 0.99 | 0.98 | 0.99 | 0.99 |
| | $\mathcal{E}_{\text{anis}}$ | $\sim 0$ | $\sim 0$ | $\sim 0$ | $\sim 0$ | $\sim 0$ | $\sim 0$ |
| | $\mathcal{E}_{\text{exch}}$ | 0.02 | 0.01 | 0.01 | 0.02 | 0.01 | 0.01 |
| Polydomain | $\mathcal{E}_{\text{demag}}$ | N/A | 0.82 | 0.83 | N/A | 0.14 | 0.26 |
| | $\mathcal{E}_{\text{anis}}$ | N/A | 0.02 | 0.01 | N/A | $\sim 0$ | $\sim 0$ |
| | $\mathcal{E}_{\text{exch}}$ | N/A | 0.16 | 0.16 | N/A | 0.86 | 0.74 |
| Vortex | $\mathcal{E}_{\text{demag}}$ | 0.13 | 0.12 | 0.13 | 0.13 | 0.12 | 0.12 |
| | $\mathcal{E}_{\text{anis}}$ | 0.08 | 0.08 | 0.07 | $\sim 0$ | $\sim 0$ | $\sim 0$ |
| | $\mathcal{E}_{\text{exch}}$ | 0.79 | 0.80 | 0.80 | 0.87 | 0.88 | 0.88 |

most observed, i.e. the S-shape ground state, which would still have a large demagnetizing field. This domain structure was likely formed due to increased importance of the demagnetizing field compared to the exchange field as sizes of magnets increased.

The direct effect of the magnetocrystalline anisotropy was hard to assess, but it did most likely stabilize the S-shape ground state, since it contributed so little to the total free energy density of the polydomain ground states. For the vortex ground state, the free energy density was mostly composed of the exchange free energy, as expected, with significant contributions from both anisotropy and demagnetization fields. This was in line with our understanding of the vortex ground state as a configuration which minimized magnetostatic self-interaction.

At 300 K the trends were similar, except for smaller contributions from the magnetocrystalline anisotropy (which was very weak at this temperature), and a different composition of the free energy density for the polydomain ground state. We saw that the relative contributions of the demagnetization field and the exchange interaction to the free energy energy density was approximately opposite to what was found at 50 K. This meant that the type of polydomain ground state at higher temperatures was more dominated by the magnetostatic interactions than exchange and magnetocrystalline anisotropy. Since the "edge vortex" ground state was the most observed polydomain ground state at this

temperature, this result seemed reasonable. We could therefore conclude with the fact that the edge vortex ground state was a result of competition between the magnetostatic self-interaction and exchange interaction.

### 4.2.5 The effect of magnetocrystalline anisotropy

The effect of the magnetocrystalline anisotropy was perhaps more subtle than the other exchange and magnetostatic effects. The anisotropy constant ranged from $100\,\mathrm{kJ/m^3}$ to $4100\,\mathrm{kJ/m^3}$ for LSMO in the temperature range we simulated. At 300 K, it should have been virtually unimportant, and contributed very little to the total free energy density of the nanomagnets. It was however not possible to determine whether this was because of minimization of the effective field created by the magnetocrystalline anisotropy, or because the magnetocrystalline anisotropy was negligible.

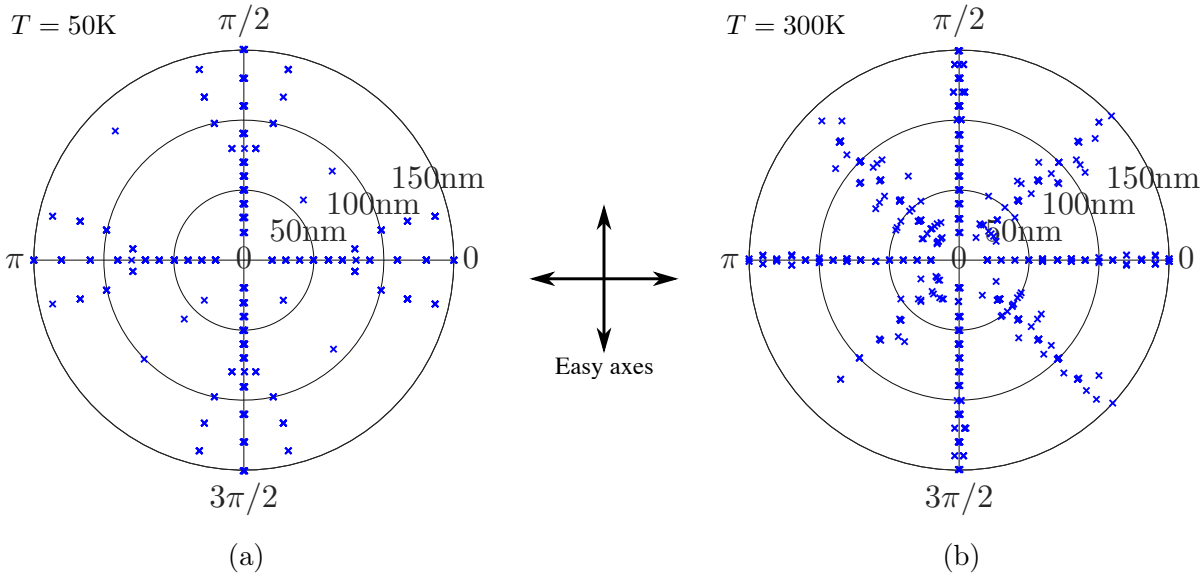


Figure 4.5: The direction of magnetization of single, monodomain circular LSMO nanomagnets at (a) 50 K and (b) 300 K. The radial axis indicates diameter of the nanomagnets in nanometer. The nanomagnets were 5 nm thick, with easy axes at 0, $\pi/2$, $\pi$ and $3\pi/2$ radians, and hard axes at $\pi/4$, $3\pi/4$, $5\pi/4$ and $7\pi/4$ radians.

In order to assess the effect of the magnetocrystalline anisotropy on the direction of magnetization for single, monodomain LSMO nanomagnets, we made polar plots of the angle of magnetization versus the diameter of the nanomagnets. The plots for 5 nm thick nanomagnets are shown in Figure 4.5. At 50 K, the majority of the monodomain magnetic ground states conformed to one of the easy axes of the system until a diameter of 80 nm was reached. At this point, also monodomain states with magnetization slightly off-axis

from the easy axis were stable. With increasing diameter, larger off-set angles were stable as well. After inspecting the magnetic profiles of these ground states, we saw that they were in a transition regime between the monodomain and "S-shape" ground states. Their average absolute reduced magnetization was however above 0.95, so they were closer to monodomain than "S-shape". A few simulations also resulted in magnetization along the hard axes. There were however few of these, and it is likely that they were metastable ground states, and that they would not have been present at finite temperature, due to thermal jostling.

At 300 K, the monodomain ground states conformed in roughly equal proportions to the eight directions given by the easy and hard axes, at least for smaller diameters. Recalling that the magnetocrystalline anisotropy was very small at this temperature, this supported the notion that the magnetocrystalline anisotropy was not of critical importance at higher temperatures. The fact that such a large amount of monodomain ground states conformed to the hard axes was most likely a numerical artifact. Since the effective field created by the magnetocrystalline anisotropy depends on the derivative of the anisotropy free energy, the effective field is close to zero around both the easy axes and the hard axes. If finite temperature was introduced (i.e. thermal jostling), it is likely that much fewer ground states would have conformed to the hard axes, if any.

### 4.2.6 Comparison of thermal energy to switching energy

In order to have superparamagnetic nanomagnets, not only is a monodomain ground state a prerequisite, the thermal energy must also be of the same order as the energy required for switching the direction of magnetization. For circular nanomagnets, the only source of anisotropy is the magnetocrystalline anisotropy. Therefore, the energy barrier associated with switching the direction of magnetization from one easy axis to another easy axis (by uniform rotation) is $K_{c1}V$. For the circular nanomagnets we simulated, the requirement for superparamagnetism was then $K_{c1}V \sim k_BT$. In Figure 4.6 we plotted the diameter at which $K_{c1}V = k_BT$ for different thicknesses and temperatures. This gave an indication of the size range where a monodomain nanomagnet would also be superparamagnetic. If considering a thickness of 5 nm, we saw that the thermal energy was equal to the switching energy for diameters from approximately 10 nm at 50 K to over 100 nm at 300 K. Since the effect of temperature is inherently random, we would expect superparamagnetic behavior for nanomagnets with somewhat larger diameters or thicknesses than what is indicated by Figure 4.6.

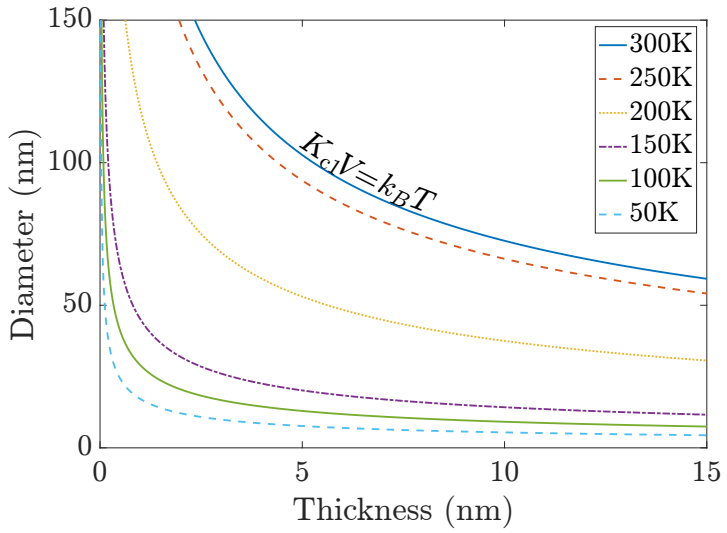


Figure 4.6: The graph shows the diameter of a circular LSMO nanomagnet at which $K_{c1}V = k_BT$ for different thicknesses and temperatures.

Having superparamagnetic nanomagnets was important if we wanted to achieve supermagnetic ordering. Therefore, choosing the right dimensions was critical. Assuming that supermagnetic ordering was strictly driven by dipole-coupling between superparamagnetic nanomagnets, we wanted to maximize the volume of these nanomagnets. The reason for this was that the dipole-dipole energy, Eq. 2.14, is dependent on the total magnetic dipole moment of each magnet, which was directly related to the volume of the magnet. Since volume scales quadratically with the diameter of a cylinder, and only linearly with thickness, a good approach would be to increase diameter before thickness. We also saw from the results that thinner nanomagnets yielded a larger range of diameters and temperatures at which superparamagnetic behavior should be present.

## 4.3 Summary of findings

In this chapter, we have investigated the magnetic properties of single LSMO nanomagnets. The geometry we chose was that of thin cylinders, to exclude shape anisotropy effects on in-plane magnetization. We simulated ground state magnetization of these nanomagnets for thicknesses from 5 nm to 15 nm and diameters in the range 20 nm to 150 nm. Two temperatures were investigated, 50 K and 300 K. We found four types of magnetic ground states, namely the monodomain ground state, the vortex ground state and two polydomain ones; the S-shape and edge vortex ground states. The two former were the most prevalently encountered ones.

We then estimated the probability of obtaining the monodomain ground state by calculating the fraction of monodomain ground states for all diameters and thicknesses. For the 5 nm thick nanomagnets, we saw that the probability of obtaining a monodomain ground state was approximately unity up to diameters of 60 nm throughout the temperature range, and the probability never fell below 0.6.

To assess the stability of the ground states of the nanomagnets and identify the dominant magnetic interactions responsible for them, we looked at the total free energy density of the different ground states, and the relative contributions from different physical phenomena. We found that the monodomain ground states for the 5 nm thick magnets were the most energetically favorable ground state up to diameters of 60 nm to 70 nm at 50 K and 120 nm to 140 nm at 50 K. The thicker nanomagnets exhibited in general lower probabilities of monodomain ground state, and larger fractions of polydomain nanomagnets. The monodomain ground state was found to be a result of exchange interaction and possibly magnetocrystalline anisotropy dominating over the magnetostatic self-interaction, whereas the opposite was true for the vortex ground state. The polydomain ground states were results of the complex competition between exchange interaction, magnetocrystalline anisotropy and the demagnetizing field. The effect of magnetocrystalline anisotropy was found to be less significant at higher temperatures.

Thermal energy was compared to the energy required to switch the direction of magnetization for the entire parameter range of simulations. This was done to evaluate whether monodomain nanomagnets would also exhibit superparamagnetism at the relevant temperatures. For 5 nm thick magnets, the diameter at which $E_{\text{thermal}} \sim E_{\text{anis}}$ ranged from approximately 10 nm at 50 K to over 100 nm at 300 K. From this, it could be inferred that the 5 nm thick LSMO nanomagnets should exhibit superparamagnetism in the range of diameters from 20 nm to over 100 nm at experimentally available temperatures.

# Chapter 5

# Supermagnetism in patterned LSMO thin films

The purpose of this chapter is to demonstrate and characterize supermagnetic ordering and phenomena in ordered arrays of LSMO nanomagnets. Section 5.1 is dedicated to the description of the specific simulation procedures we utilized, and Section 5.2 to results and discussion. In Sections 5.2.1 to 5.2.4, we will examine the supermagnetic ground states of the arrays. Effects of stacking, exchange decoupling and finite size will be discussed. Sections 5.2.5 to 5.2.8 focus on the response of the arrays to applied fields and magnetization dynamics. Finally in Section 5.3, we summarize the most important findings in this chapter.

## 5.1 Simulating arrays of LSMO nanomagnets

After exploring the magnetic properties of circular LSMO nanomagnets, we wanted to investigate supermagnetic ordering in arrays of LSMO nanomagnets, as well as the magnetic properties of such arrays.

We investigated two different two-dimensional Bravais lattices, namely the square lattice and the hexagonal lattice. The reason for this was that the latter has been predicted to exhibit superferromagnetic ordering, whereas the former has been predicted to show superantiferromagnetic ordering, with no net magnetization.

The square lattice is illustrated in Figure 5.1. The parameters used for the array were $d = 50\,\text{nm}$ and $|\boldsymbol{a}_1| = |\boldsymbol{a}_2| = 60\,\text{nm}$, so that the interparticle spacing was $10\,\text{nm}$. Needless

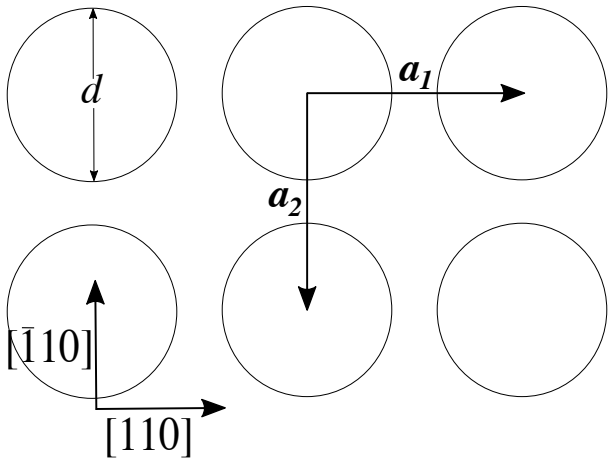


Figure 5.1: An illustration of the square Bravais lattice of LSMO nanomagnets with primitive lattice vectors $\boldsymbol{a}_1$ and $\boldsymbol{a}_2$. Each magnet was centered on a lattice point. The easy axes of the magnets were in the $\langle 110 \rangle$-directions, i.e. parallel to both $\boldsymbol{a}_1$ and $\boldsymbol{a}_2$.

to say, $\boldsymbol{a}_1 \perp \boldsymbol{a}_2$. The thickness of the magnets was 5 nm. These choices were based on results from the simulations of single nanomagnets, as well as wanting to keep in-plane dimensions as large as possible, in order to ensure that the structures were feasible to manufacture in the laboratory.

The entire array consisted of 30 magnets in both directions, i.e. 900 magnets in total, meaning that the square array measured 1.8 µm along both edges. The simulation grid was $1024 \times 1024$ cells. Unless otherwise stated, the material parameters were chosen to corresponding to a temperature of 250 K. The reason for choosing 250 K was that we expected stronger interparticle coupling at this temperature, due to a larger value of $M_S$, but we would still be well within the superparamagnetic regime of the individual nanomagnets. We first performed quenched relaxations, and later temperature relaxations, to see whether the relaxation scheme would affect the supermagnetic ground state.

The hexagonal array is illustrated in Figure 5.2. Once again we chose to use $d = 50$ nm, $|\boldsymbol{b}_1| = |\boldsymbol{b}_2| = 60$ nm and a thickness of 5 nm. The angle between $\boldsymbol{b}_1$ and $\boldsymbol{b}_2$ was 60°. Each row of magnets in the direction of $\boldsymbol{b}_1$ consisted of 30 magnets, and the entire array consisted of 34 rows, arranged in a zig-zag configuration, i.e. with every row displaced by $\boldsymbol{b}_2$ and every other row displaced by an additional $-\boldsymbol{b}_1$. This yielded an approximately square array with dimensions of 1.8 µm × 1.8 µm. We chose to use a simulation grid of $1024 \times 1024$ here as well.

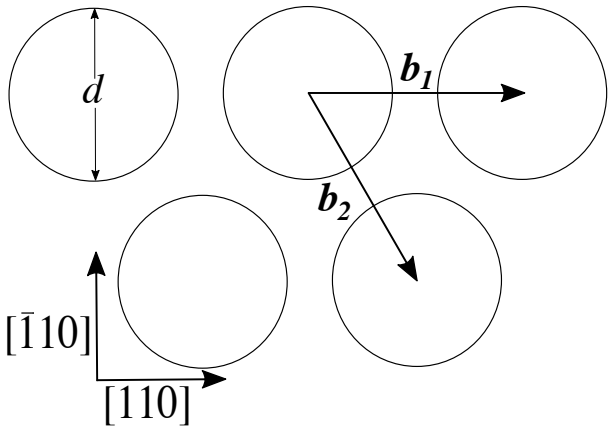


Figure 5.2: An illustration of the hexagonal Bravais lattice of LSMO nanomagnets with primitive lattice vectors $\boldsymbol{b}_1$ and $\boldsymbol{b}_2$. Each magnet was centered on a lattice point. The easy axes of the magnets are in the $\langle 110 \rangle$-directions.

## 5.2 Results and discussion

### 5.2.1 Tailoring supermagnetic ordering through stacking

In order to explore the inherent supermagnetic ordering of the arrays described in Section 5.1, we performed 50 energy minimizations, starting from random configurations. The results from the temperature relaxation of the square array showed that interparticle interactions did indeed favor SAF ordering. Four of the 50 magnetic ground states are shown in Figure 5.3.

As predicted by theory, the finite lattice exhibited non-uniform ground states, with domain structures and defects, such as small regions with SFM ordering instead of SAF ordering. In addition, there was no single ground state, but instead a plethora of magnetic conformations that were all approximately equally stable from a free energy perspective. The average macroscopic magnetization of the 50 square arrays was $\langle |\hat{\boldsymbol{m}}| \rangle = 0.035 \pm 0.019$. The error estimate corresponded to one standard deviation.

Even though the SAF domains took on different shapes and sizes, there were some features that seemed more universal. Due to the finite nature of the lattices, the magnetization tended to align with the edges of the arrays. Also, the vast majority of domain walls were abrupt, and involved either a 90° rotation of magnetization or no rotation at all (i.e. a "SFM stacking fault").

The hexagonally stacked arrays displayed very different magnetic ground states from the square arrays. The material parameters were exactly the same, and the arrays were

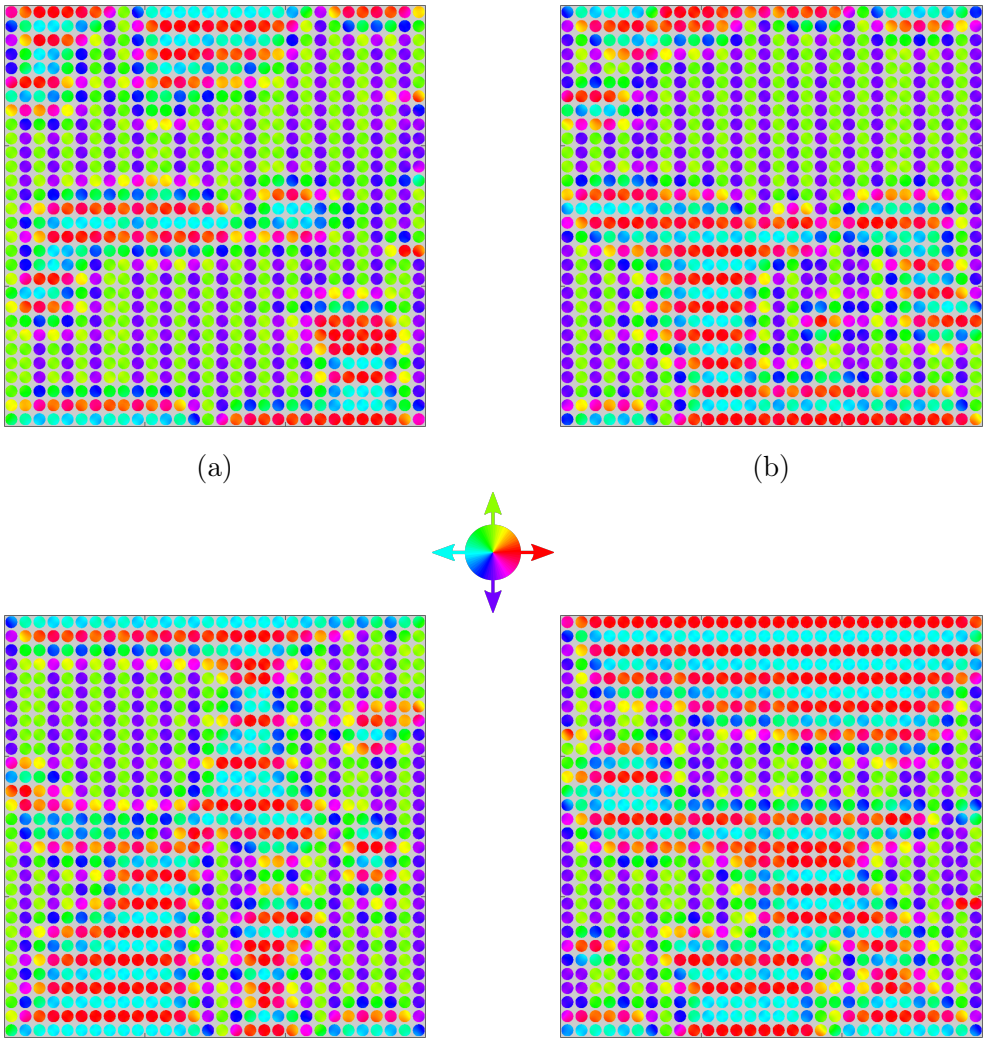


Figure 5.3: Four of the 50 simulated magnetic ground states for the square array. The direction of magnetization is given by the color legend in the middle. The arrays were 1.8 µm × 1.8 µm and 5 nm thick. The $\boldsymbol{a}_1$-direction was along the horizontal edge, and $\boldsymbol{a}_2$ along the vertical edge.

initialized to the same random configurations, so the only significant difference was in fact the stacking pattern.

Four of the 50 magnetic ground states are shown in Figure 5.4. The average magnetization of the hexagonal arrays was $\langle|\hat{\boldsymbol{m}}|\rangle = 0.086 \pm 0.051$, which was not significantly different from the magnetization of the square stacked arrays.

The domain structure of the hexagonally stacked arrays was more reminiscent of that found in a continuous ferromagnetic thin film. There were examples of disordered ground states, as shown in Figure 5.4a, but the most prevalent type of ground state was the

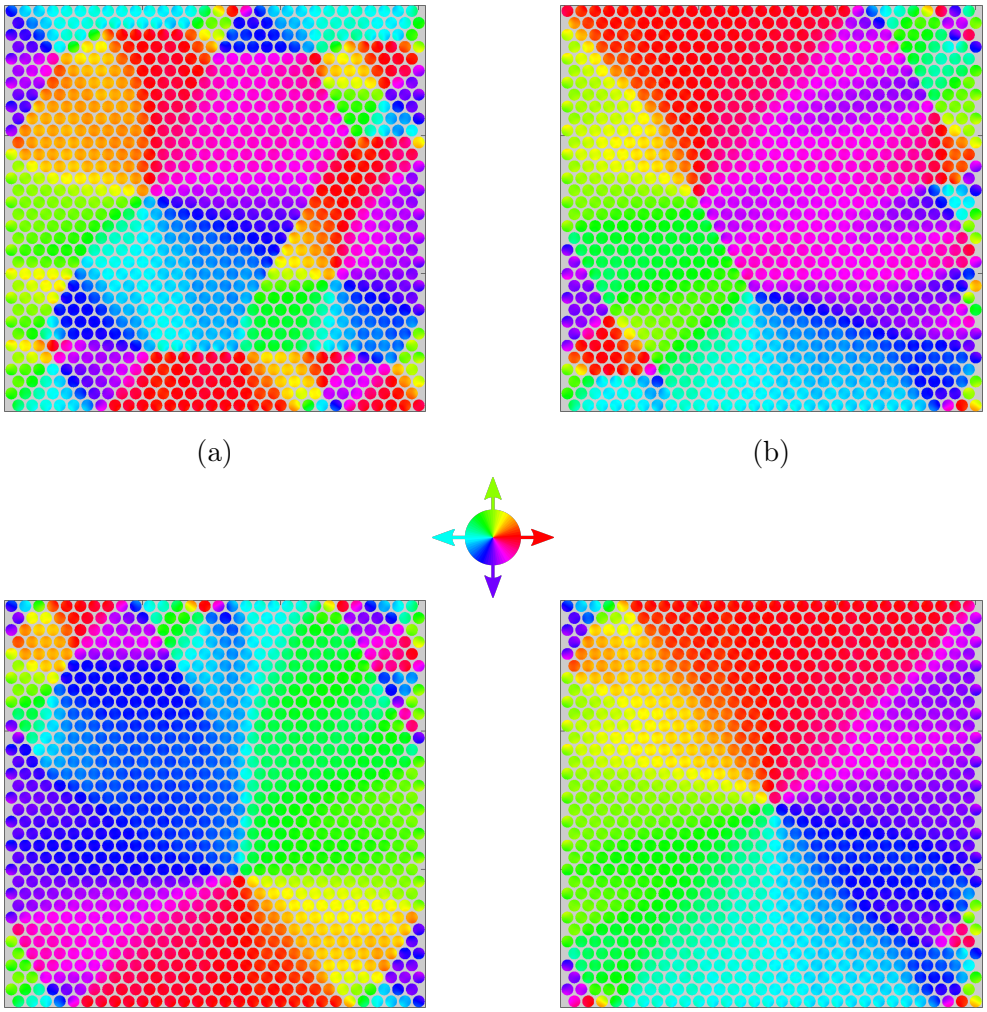

Figure 5.4: Four of the 50 simulated magnetic ground states for the hexagonal array. The direction of magnetization is given by the color legend in the middle. The arrays were approximately 1.8 µm × 1.8 µm and 5 nm thick. The $\boldsymbol{b}_1$-direction was along the horizontal edge.

Landau-like vortex state, of which one example is shown in Figure 5.4d. The quasi-Landau states of the array did however in general exhibit six domains, instead of the classical four of ordinary Landau states (an example of a Landau state in a continuous LSMO thin film is shown in Figure 5.5). One similarity between the two differently stacked arrays was that the magnetization tended to align with the edges of the arrays.

The presence of the six-fold quasi-Landau state meant that the LSMO nanomagnets did not only conform to the easy axes of the individual magnets, but seemed to conform to directions induced by the lattice as well. Hence, there was an apparent superlattice-induced magnetic anisotropy. The strength of the induced anisotropy must have been

of the same order as the magnetocrystalline anisotropy (which was fairly weak, $K_{c1} = 100\,\mathrm{J/m^3}$), since its effect was so pronounced.

The more disordered ground states did exhibit some common features. For instance, most domain walls tended to align with axes of high-symmetry. Abrupt domain walls always took place along one of the primitive directions of the lattice, as illustrated by the oblique middle domain wall in Figure 5.4b, whereas the extended domain walls could form along other axes, such as the vertically aligned domain wall in Figure 5.4c. Abrupt domain walls tended to involve a 180° rotation of the magnetization, whereas the extended walls more often involved a 60° or 90° rotation. This did not mean that there weren't examples of abrupt domain walls with 60° or 90° rotations. Multiple vortex-like structures were also present.

One of the most important differences between these superlattices of nanomagnets and continuous thin films, was the exchange decoupling between separate nanomagnets. We know that the exchange interaction is very important for alignment of magnetic moments and long-range order in continuous films. We have seen that dipolar interactions may also favor aligned magnetic moments, and that it can induce long-range order. To elucidate how exchange decoupling affected the ordering of the arrays, we compared the arrays to a continuous LSMO thin film.

### 5.2.2 The effect of exchange decoupling

The continuous thin film of LSMO we simulated had dimensions $1.8\,\mu\mathrm{m} \times 1.8\,\mu\mathrm{m} \times 5\,\mathrm{nm}$, with the same material parameters as the arrays. We also used the same relaxation procedures. The result is shown in Figure 5.5.

The continuous film exhibited four large domains with magnetization along the easy axes of the system. The magnetocrystalline easy axes were in the horizontal and vertical directions, and we see that the magnetization aligned with these directions. This also meant that the magnetization aligned with the edges of the film, which is preferential for the minimization of the stray field. There were clearly defined, although somewhat extended, domain walls. The domain structure is a good example of a Landau state. The magnetic ground states of the hexagonal array resembled the continuous film case, but the hexagonal array exhibited more disorder and chaos.

One of the most obvious effects of exchange decoupling was then that the length scales necessary for disorder and non-unique ground states were greatly reduced. No conven-

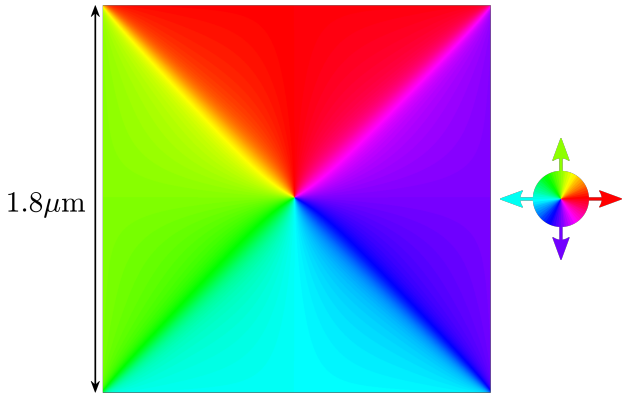


Figure 5.5: The magnetic ground state of a 1.8 µm × 1.8 µm square shaped continuous LSMO thin film. The thickness of the film was 5 nm. The magnetic domain structure was a good example of a typical Landau state. Direction of magnetization was according to the color legend to the right.

tional ferromagnetic material would show the type of magnetic ground state exhibited by the square arrays, whereas the hexagonal arrays could be said to resemble continuous thin films of LSMO, but for much larger thin films (i.e. typical blanket film magnetization). The combination of exchange decoupling and different superlattice structures may open for the possibility of engineering specific and novel magnetic spin textures at length scales that were previously unavailable.

### 5.2.3 Statistically quantifying interparticle coupling

In the previous sections, we presented a qualitative description of the simulated magnetic ground states of the two arrays we defined. We also wanted to develop a method to quantitatively analyze the magnetic ground states. The method is described in Appendix A.1, and was based on calculating average one dimensional Fourier power spectra of the magnetization along the primitive lattice directions of the nanomagnet arrays. The method was useful for quantifying periodicities in the magnetic texture.

The average Fourier power spectra of the perpendicular components of the magnetization for the square array along the $\boldsymbol{a}_1$- and $\boldsymbol{a}_2$-directions, as specified in Figure 5.1, is shown in Figure 5.6. The spectra of the parallel components of the magnetization are given in Appendix B.2. They showed that the average parallel component of the magnetization was non-zero. In addition, there was nearest-neighbor periodicity, indicating that the parallel components of the magnetization typically took on a head-to-tail configuration.

The spectra of the perpendicular components of $\hat{\boldsymbol{m}}$, Figures 5.6a and 5.6b, showed no

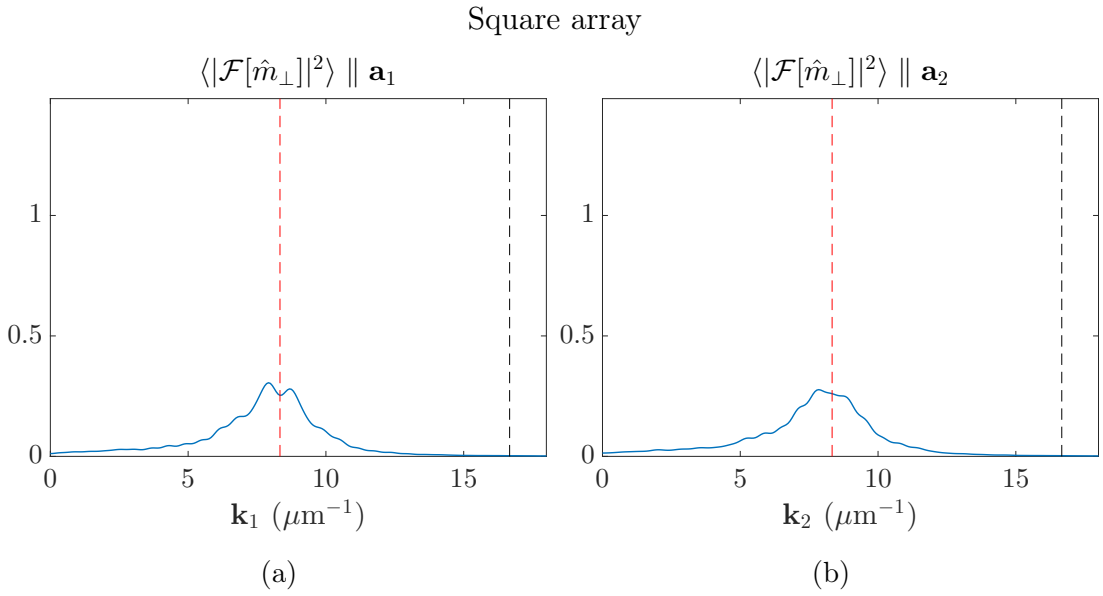


Figure 5.6: Average Fourier power spectra of the perpendicular components of the magnetization of the square array along (a) $\boldsymbol{a}_1$ and (b) $\boldsymbol{a}_2$ exhibited peaks centered at $\boldsymbol{k} = 8.33\,\mu\text{m}^{-1}$, indicated by the red, vertical dashed line. These peaks corresponded to a periodicity of 120 nm.

DC peak, indicating that the average perpendicular components of the magnetization was zero. This was consistent with how the biaxial anisotropy of the system did not favor the $\boldsymbol{a}_1$-direction over $\boldsymbol{a}_2$ or vice versa, so that average perpendicular magnetization should be zero. The only significant peak in these spectra was the one centered around $\boldsymbol{k} = 8.33\,\mu\text{m}^{-1}$, indicating a periodicity of 120 nm, or equivalently, a next-nearest-neighbor periodicity. Both peaks showed signs of splitting, indicating deviation from perfect ordering. From this, we could infer that the perpendicular components of the magnetization were on average opposite in every other nanomagnet. The Fourier power spectra reflected the observed magnetic structure, i.e. superantiferromagnetic ordering made up of alternating dipolar chains, but with multiple domains.

We wanted to quantify the average interparticle coupling for the hexagonal arrays as well, and therefore we performed Fourier analysis of the 50 magnetic ground states. The parallel and perpendicular components were analyzed along the primitive directions of the lattice, i.e. the $\boldsymbol{b}_1$- and $\boldsymbol{b}_2$-directions as defined in Figure 5.2. The Fourier power spectra of the perpendicular components are shown in Figure 5.7, whereas the spectra of the parallel components are given in Appendix B.2. The characteristics of the parallel components of the magnetization were similar to that of the square array, except there were signs of peak splitting, indicative of multiple domains. This meant that the parallel components of the magnetization typically aligned in a head-to-tail fashion, but that

the length of these dipolar chains were generally shorter than the array. This was in agreement with observations.

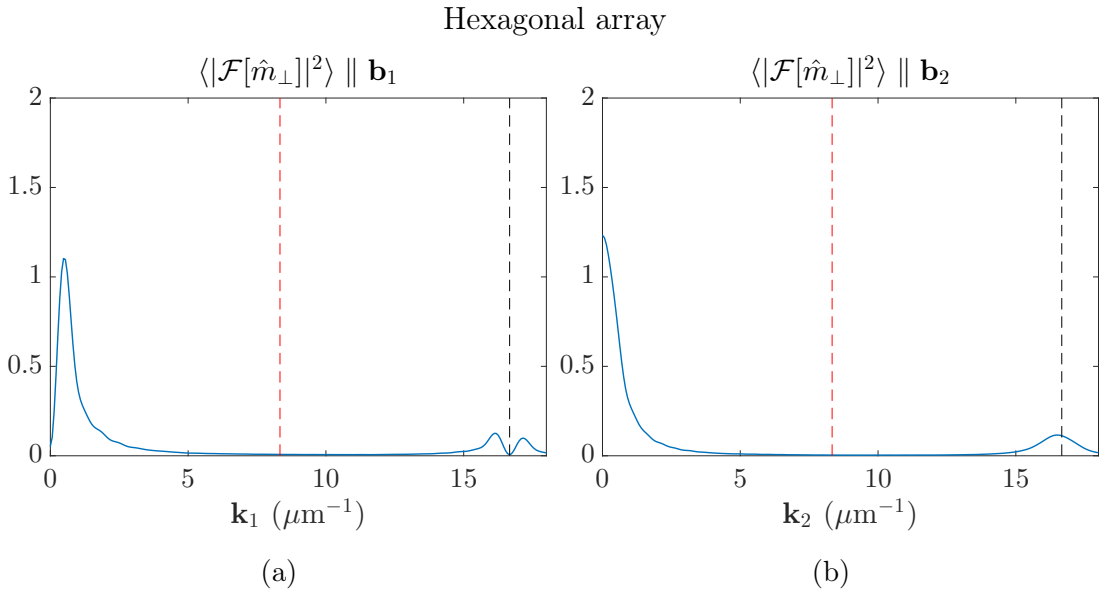


Figure 5.7: Average Fourier power spectra of the perpendicular components of the magnetization of the hexagonal array along (a) $\boldsymbol{b}_1$ and (b) $\boldsymbol{b}_2$ exhibited peaks or split peaks centered at $\boldsymbol{k} = 16.67\,\mu\text{m}^{-1}$, indicated by the black, vertical dashed line. The difference between the two latter spectra was that the first case did not exhibit a significant DC peak at zero, but instead a peak at $\boldsymbol{k}_1 = 0.48\,\mu\text{m}^{-1}$, whereas the latter had a DC peak centered at zero.

The main feature of the average Fourier power spectra of the hexagonal array was the fact that the periodicity of the magnetization was predominantly of the nearest-neighbor kind, with some long-wave or DC contributions, which was suggestive of SFM ordering. The spectrum of $\hat{m}_\perp$ along $\boldsymbol{b}_1$, Figure 5.7a, had both a split DC-peak, with near-zero amplitude at $\boldsymbol{k}_1 = 0$, and a split nearest-neighbor peak. Hence, the average perpendicular magnetization to $\boldsymbol{b}_1$ was close to zero, and multiple domains were present. Since the magnetocrystalline easy axes of the nanomagnets were parallel and perpendicular to $\boldsymbol{b}_1$, and the array was otherwise symmetric about $\boldsymbol{b}_1$, this result was not surprising. The average perpendicular magnetization should indeed be zero. The difference from SAF ordering is obvious, since the periodicity of the perpendicular magnetization was of the nearest-neighbor kind, not next-nearest-neighbor.

The spectrum of $\hat{m}_\perp$ along $\boldsymbol{b}_2$, Figure 5.7b, did not exhibit split peaks. The perpendicular component of the magnetization with respect to $\boldsymbol{b}_2$ was therefore not on average zero, but the nature of the periodicity was otherwise similar. This may be a result of the fact

that the array of nanomagnets was asymmetric about the $\boldsymbol{b}_2$-direction, both with respect to array shape and magnetocrystalline easy axes.

Using Fourier power spectra to quantitatively determine the nature of the average interparticle coupling yielded results that enforced our conclusions from the qualitative analysis of the magnetic ground states of both arrays, but the method was not suited for assessing e.g. the strength of coupling between particles, and it didn't provide a single quantity that could be used as order parameter. We also hoped that the spectra would provide information about average sizes of domains, but that was unfortunately not the case.

### 5.2.4 Identifying finite size effects on supermagnetic ground state

All previous simulations of both the square and hexagonally stacked arrays were done on finite arrays, i.e. arrays that terminated at the edges of the simulation box. In order to investigate the effects of finite size, we performed the same simulations with periodic boundary conditions. Note that we did not introduce the typical infinite periodic boundary conditions, but instead a single extra image of the arrays on the four edges of the arrays. This choice was based on the assumption that infinitely repeating boundary conditions would lead to an idealized situation that could not be realized experimentally.

Two of the ground states for the square array with periodic boundary conditions, and two for the hexagonal array with periodic boundary conditions are shown in Figure 5.8.

For the square array with periodic boundary conditions, Figures 5.8a and 5.8b, the ground states exhibited close to perfect SAF ordering. Not all magnetic ground states were this ordered, but they were in general more ordered than the ground states of the finite arrays. The average magnetization of all 50 simulated ground states for the square arrays was $\langle|\hat{\boldsymbol{m}}|\rangle = 0.023 \pm 0.017$, which was somewhat smaller than for the square arrays without periodic boundary conditions. One possible reason could be the fact that the nanomagnets at the edges no longer had any reason to align their magnetization with the edge, leading to less disorder, which lowered the average magnetization.

It would be instructive to examine the Fourier spectra of the magnetization profiles of Figures 5.8a and 5.8b, since these were the two ground states that ended up the closest to perfect ordering. The Fourier power spectra of the vertical components of the magnetization in Figure 5.8a, and similarly for the horizontal components of the

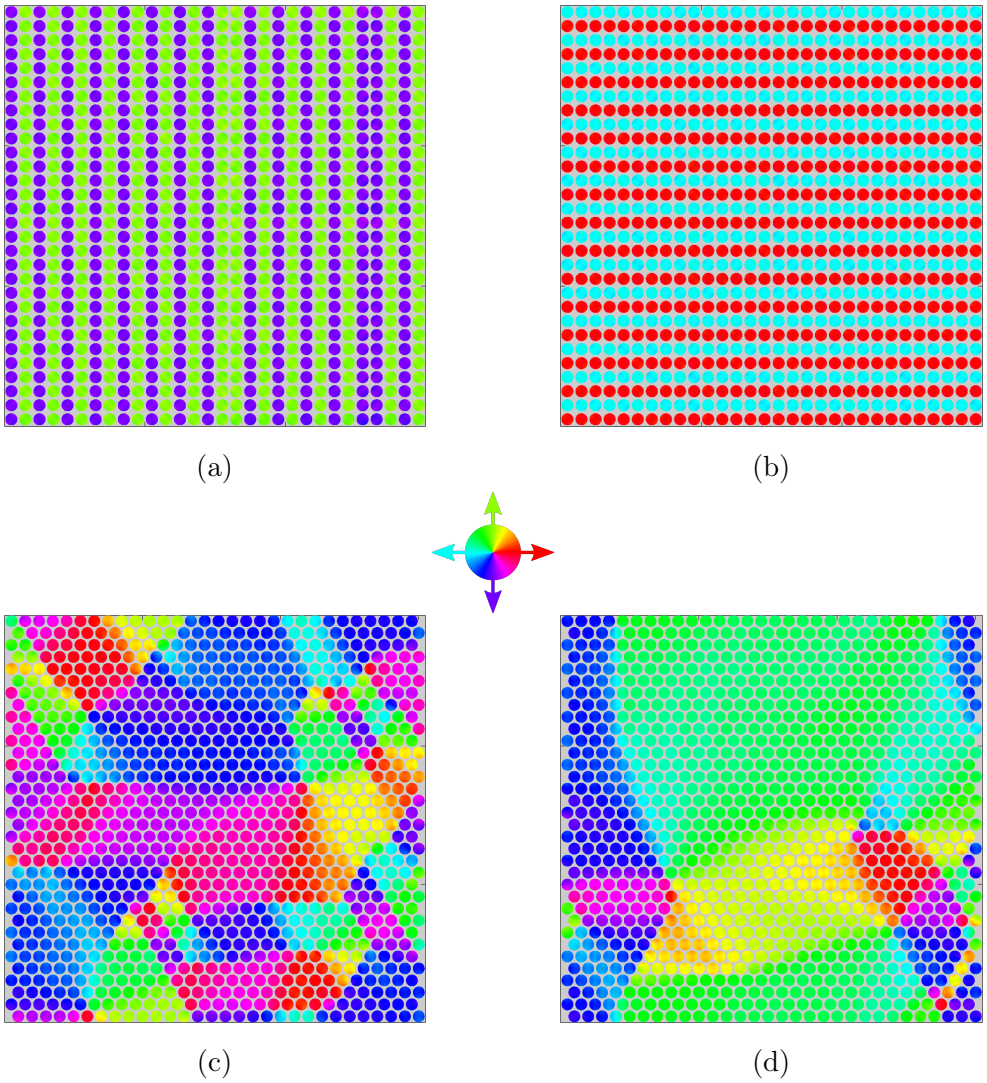


Figure 5.8: The magnetic ground states of randomly initialized arrays with periodic boundary conditions. The square stacked arrays, (a) and (b), exhibited near-perfect SAF ordering. The hexagonally stacked arrays, (c) and (d), showed more disordered magnetic ground states than what was exhibited by the hexagonal arrays without periodic boundary conditions. The dimensions of the arrays were approximately $1.8\,\mu\text{m} \times 1.8\,\mu\text{m}$. The nanomagnets were 5 nm thick.

magnetization in Figure 5.8b, are given in Figures 5.9 and 5.10, respectively. The Fourier power spectra of the other components of the magnetization showed no significant peaks, meaning that the these were very close to zero throughout the arrays.

We saw that the Fourier power spectra of Figure 5.8a, shown in Figure 5.9, closely resembled the average power spectra of the arrays without periodic boundary conditions in Figure 5.6, except the peaks were narrower, and the next-nearest neighbor peak splitting was more pronounced. The splitting arose because of the SFM stacking faults in Figure

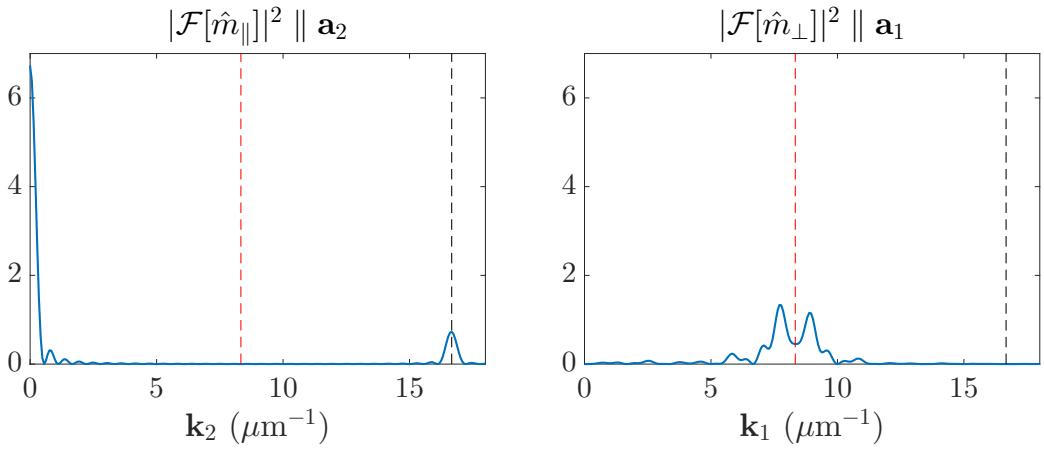


Figure 5.9: Fourier power spectra of the vertical components of the magnetization in Figure 5.8a. The spectrum of $\hat{m}_{\parallel}$ along $\boldsymbol{a}_2$ (a) exhibited typical DC and nearest-neighbor peaks, and the spectrum of $\hat{m}_{\perp}$ along $\boldsymbol{a}_1$ a split next-nearest neighbor peak.

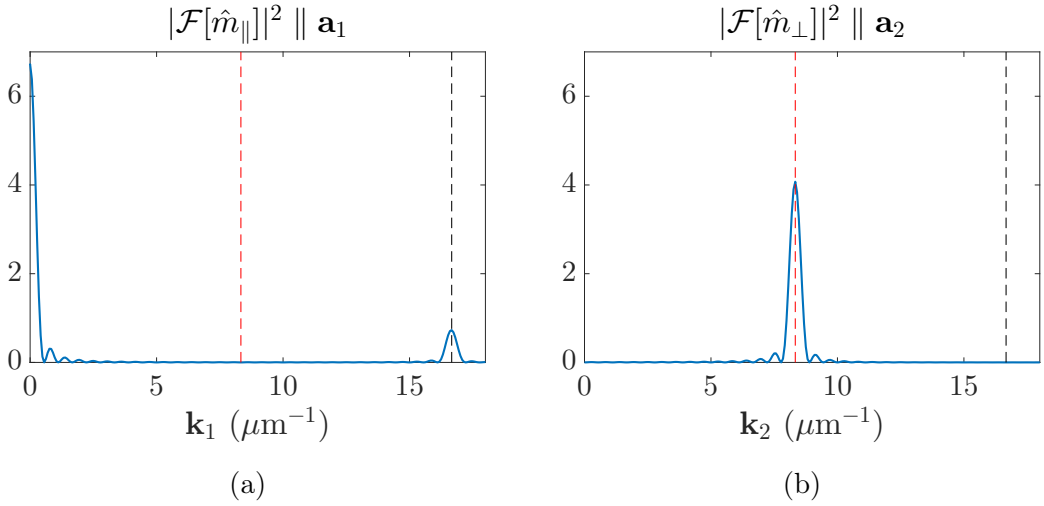


Figure 5.10: Fourier power spectra of the horizontal components of the magnetization in Figure 5.8b. The spectrum of $\hat{m}_{\parallel}$ along $\boldsymbol{a}_1$ (a) exhibited typical DC and nearest-neighbor peaks, and the spectrum of $\hat{m}_{\perp}$ along $\boldsymbol{a}_2$ a next-nearest neighbor peak.

5.8a, enforcing our interpretation of split peaks as a sign of multiple domains. The spectra of Figure 5.8b in Figure 5.10 exhibited the DC and nearest-neighbor peaks for the parallel magnetization, and the next-nearest neighbor peak for the perpendicular components. These two spectra illustrated nicely how the Fourier power spectra of perfect SAF ordering would look.

For the hexagonally stacked arrays, Figures 5.8c and 5.8d, the magnetic ground states were more disordered than the ones of the finite lattices. The tendency for the magne-

tization to align with the edges was less pronounced. This was reflected in the average magnetization of the arrays, which was $\langle|\hat{\boldsymbol{m}}|\rangle = 0.25 \pm 0.11$. This may have been a result of larger domains, as seen in Figure 5.8d, and suggests that the more ideal the hexagonal lattice becomes (i.e. closer to the infinite, idealized situation), the larger the magnetization becomes as well.

An important difference between the square stacked and hexagonally stacked arrays was that whereas the former seemed to become more ordered when periodic boundary conditions were introduced, the opposite was true for the latter. The hexagonal lattice exhibited typical blanket film magnetization when periodic boundary conditions were applied. A possible explanation was that the increased order was a result of how the forces behind ordering of the square lattice was of a short-ranged nature, whereas the opposite was true for the hexagonal array. To illustrate this point, consider a nanomagnet in the middle of the square array. The magnetic field from another nanomagnet a couple of unit cells away would not influence the first nanomagnet significantly, due to the cancelling effect of alternating directions of magnetization. For the hexagonal array, there was typically much less cancelling effects from alternating directions of magnetization. Hence, a nanomagnet in the middle of the hexagonal array would be influenced by a much larger neighborhood of other nanomagnets. This would increase the propensity for frustrated magnetic ground states, which we saw was realized through more disorder.

### 5.2.5 Tuning the supermagnetic ground state by applying a field

To investigate how the magnetic ground states of the arrays could be controlled by applying a field, we found the ground states of the arrays after they had been magnetically saturated in different directions. The square array was completely saturated along two different directions, the $[\bar{1}10]$- and the $[\bar{1}00]$-directions. These were chosen because the former constituted an easy axis of the entire array, since each particle had magnetocrystalline easy axes in the $\langle 110\rangle$-directions, whereas the latter saturation direction was a hard axis for the array, because of the hard axes of each particle. The hexagonal array was saturated along the same axes as the square array, for similar reasons. Even though the $[\bar{1}10]$-direction was an easy axis for the nanomagnets, it was not a direction of high-symmetry for the hexagonal array, so the axis could not be considered a true easy axis.

The two magnetic ground states of the square stacked array after saturation are shown in Figure 5.11. The array initialized along the $[\bar{1}10]$-direction, Figure 5.11a (the green

arrow if referring to the color legend), exhibited a large degree of SAF ordering. Two large SAF domains formed with magnetization perpendicular to the initial direction of magnetization. The two domains were off-set by one row, so that they had opposite magnetization along the horizontal direction. The formation of these domains was most likely initiated by the large demagnetizing fields at the horizontal edges of the array. The array initialized along the $[\bar{1}00]$-direction, Figure 5.11b, exhibited a multidomain, albeit ordered, SFM ground state. This was one example where the square stacked array exhibited SFM ordering. The magnetization followed the edges of the array, somewhat reminiscent of a Landau state. The big difference between a Landau state and this one was of course that this state was not flux-closed since there were large demagnetizing fields at the top left and bottom right corners.

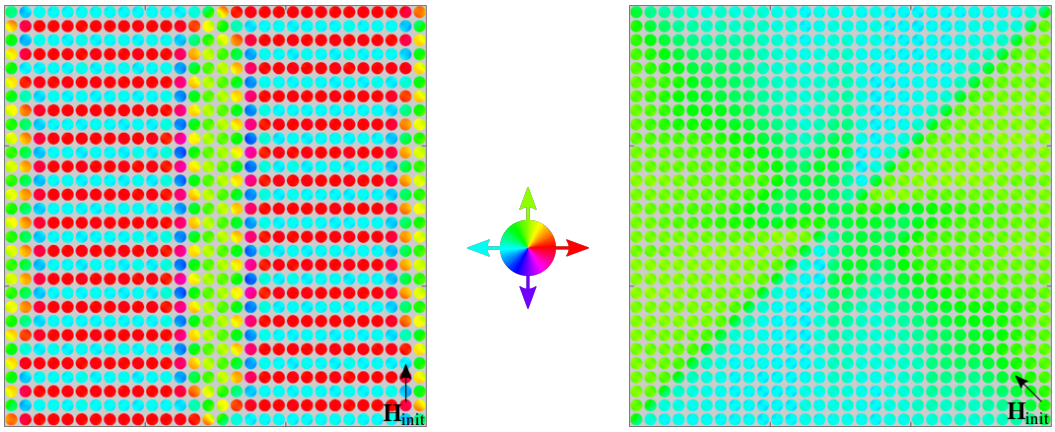


(a) (b)

Figure 5.11: The magnetic ground states of the square stacked array after it was magnetically saturated in the (a) $[\bar{1}10]$-direction and (b) the $[\bar{1}00]$-direction, as indicated by the black arrows. The resulting $|\hat{\boldsymbol{m}}|$ was (a) 0.15 along the $[\bar{1}10]$-direction and (b) 0.83 along the $[\bar{1}00]$-direction.

For the hexagonally stacked array, the magnetic ground states of the initially saturated arrays are shown in Figure 5.12. The one initialized along the $[\bar{1}10]$-direction is shown in Figure 5.12a. Multiple domains formed in this array, once again probably initiated by the demagnetizing fields at the horizontal edges. The hexagonal stacking was reflected in the domain structure, which exhibited a quasi-hexagonal symmetry (domain walls roughly followed the primitive lattices of the hexagonal array). The array initialized along the $[\bar{1}00]$-direction, Figure 5.12b, resembled the magnetic profile of the square stacked array in Figure 5.11b, but with less sharp domain walls. Interestingly, all the magnetic ground states portrayed in Figures 5.11 and 5.12 exhibited inversion symmetry.

These simulations were effectively investigations of the remanent states of the ordered

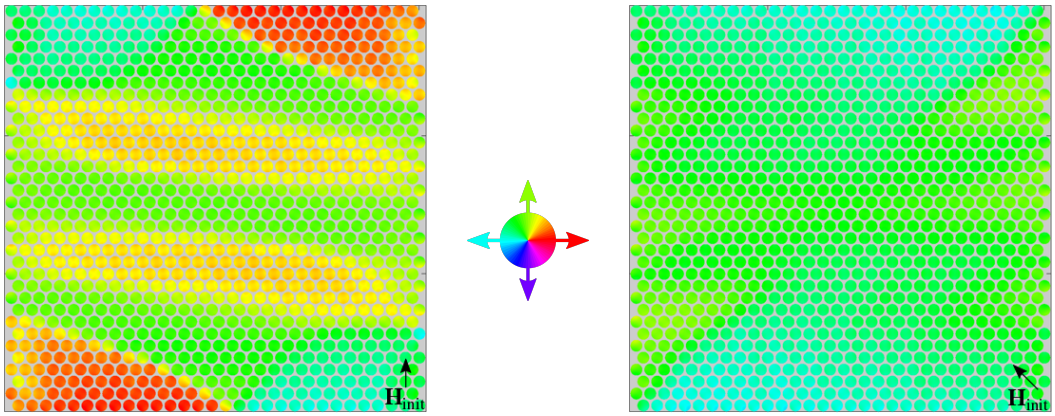


(a) (b)

Figure 5.12: The magnetic ground states of the hexagonally stacked array after it was magnetically saturated in the (a) $[\bar{1}10]$-direction and (b) the $[\bar{1}00]$-direction, as indicated by the black arrows. The resulting $|\hat{\boldsymbol{m}}|$ was (a) 0.79 at an angle of $-6^\circ$ with respect to the $[\bar{1}10]$-direction and (b) 0.92 at an angle of $-1^\circ$ with respect to the $[\bar{1}00]$-direction.

arrays. The final direction and magnitude of magnetization for the square arrays showed that initialization along the easy axes of the array lead to a small remanent magnetization along the easy axes ($|\hat{\boldsymbol{m}}| = 0.15$), and initialization along the hard axes lead to much larger magnetization along the hard axes ($|\hat{\boldsymbol{m}}| = 0.83$). There was no considerable rotation of the final magnetization with respect to the initial magnetization. The large difference in final magnetization was of course caused by the difference in supermagnetic ordering for the differently initialized arrays. The conclusion was therefore that by using an applied field, we could switch between SAF and SFM ordering in the square array.

For the hexagonal array, the remanent magnetization was larger. The $[\bar{1}10]$-initialized array exhibited $|\hat{\boldsymbol{m}}| = 0.79$ rotated by $-6^\circ$ with respect to the initial direction of magnetization, and correspondingly $|\hat{\boldsymbol{m}}| = 0.92$ rotated by $-1^\circ$ for the $[\bar{1}00]$-initialized array. Hence, the remanent magnetization of the hexagonal array was generally greater, accompanied by small rotations. This was most likely caused by the fact that the axes of high symmetry did not coincide with the initial directions of magnetization.

### 5.2.6 The effect of superlattice symmetry on the hysteretic behavior of supermagnetic arrays

In order to further characterize the magnetic response of the two different arrays to an applied field, we simulated hysteresis curves of both arrays. The geometries and material parameters of the two arrays were exactly as before.

First, we simulated hysteresis loops with an applied field along the [110]-direction. The applied field ranged from $-20\,\mathrm{mT}$ to $20\,\mathrm{mT}$, with steps of $0.25\,\mathrm{mT}$. Both arrays were first temperature relaxed, as described in Section 3.4, in zero field, before the external field was applied. The magnetization profiles and average magnetization were saved at each point.

The hysteresis loop of the square array is shown in Figure 5.13. Similarly, the hysteresis loop of the hexagonal array is shown in Figure 5.14. Calculated values of $\boldsymbol{H}_c$ and $\boldsymbol{M}_r$ for these two cases are given in Table 5.1.

The characteristics of the full hysteresis loop of the square array, Figure 5.13a, were interesting, as it exhibited well defined steps. In order to properly understand why these steps appeared, we looked closer at the magnetic microstructure of the arrays at different points of the hysteresis loop. These points are indicated by the roman numerals I-VI in Figure 5.13a, and the corresponding magnetic microstructures are shown in Figures 5.13b through 5.13g.

Starting in the top right corner of the hysteresis loop, the array was completely saturated towards the right, i.e. completely red if referring to the color legend. As the applied field was lowered, the magnetization followed the blue curve towards point I. The SAF domains nucleated along the vertical edges, and grew steadily up until this point. The difference in applied field between points I and II, as well as II and III, was only $0.25\,\mathrm{mT}$, but over this small interval, the magnetic microstructure changed to the one portrayed in Figure 5.13d, which was similar to the ground state of the square array shown in Figure 5.11a. This lead to the large decrease in $\boldsymbol{M}$. As the applied field was reduced further, so that it became negative, the domain structure changed gradually till point IV, after which it switched quite rapidly to the configuration at point V. This domain structure was maintained throughout most of the step at point V. The small decrease in magnetization along the step stemmed from gradual 90° rotation of the vertically aligned superspins. The transition from the step at V to the step at VI was a result of the red rows at the top and bottom of Figure 5.13f switching, so that the domain structure was as shown in Figure 5.13g. The final transition into the fully saturated state involved the

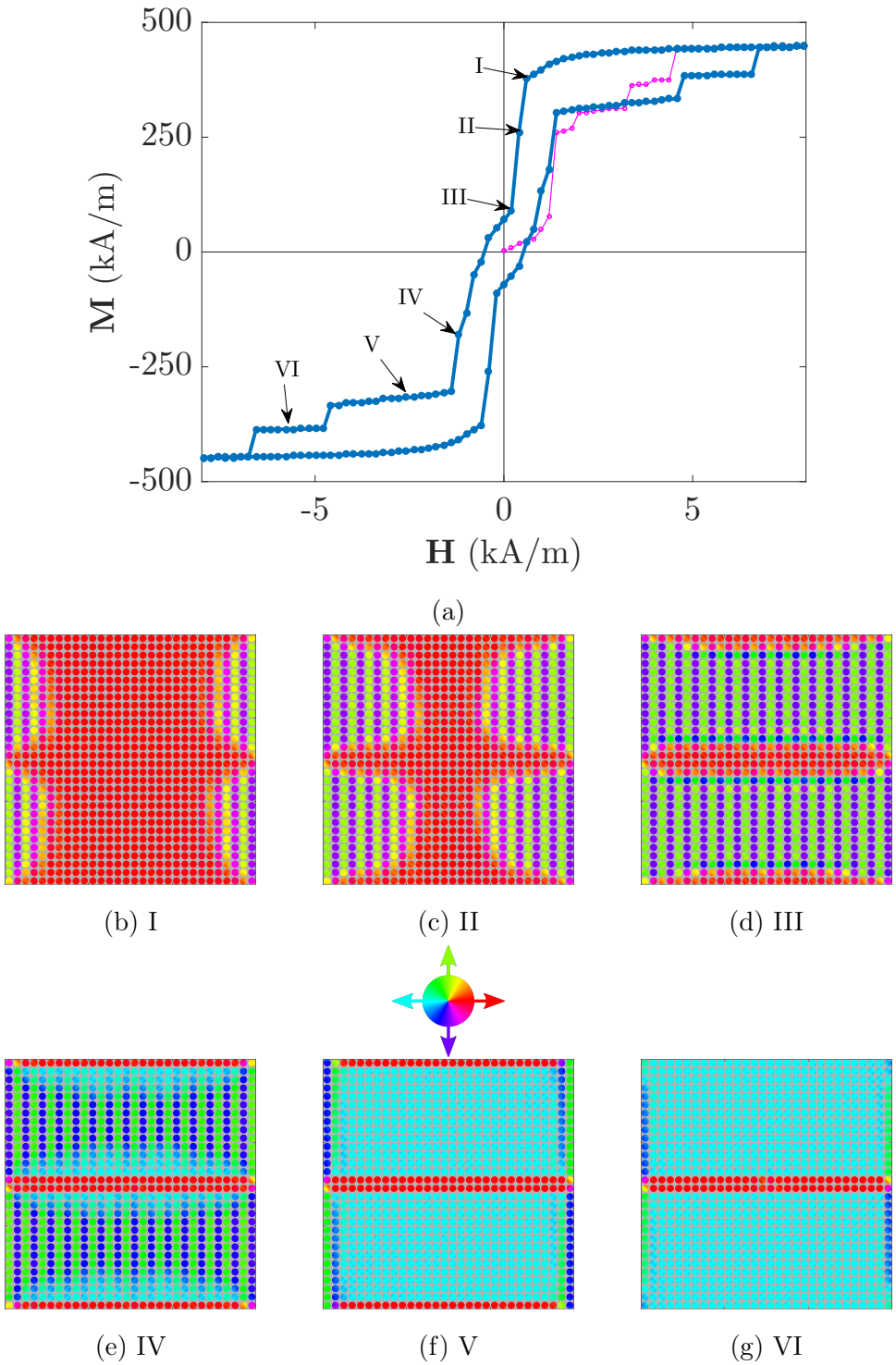


(a)

(b) I (c) II (d) III

(e) IV (f) V (g) VI

Figure 5.13: Hysteresis of the square array along the [110]-direction (a) with the magnetic profile of the array at different points of the hysteresis loop (b-g). The pink curve in the hysteresis loop was the virgin magnetization curve.

switching of the last two red rows.

The hysteresis loop of the hexagonal lattice, Figure 5.13a, did not exhibit the same

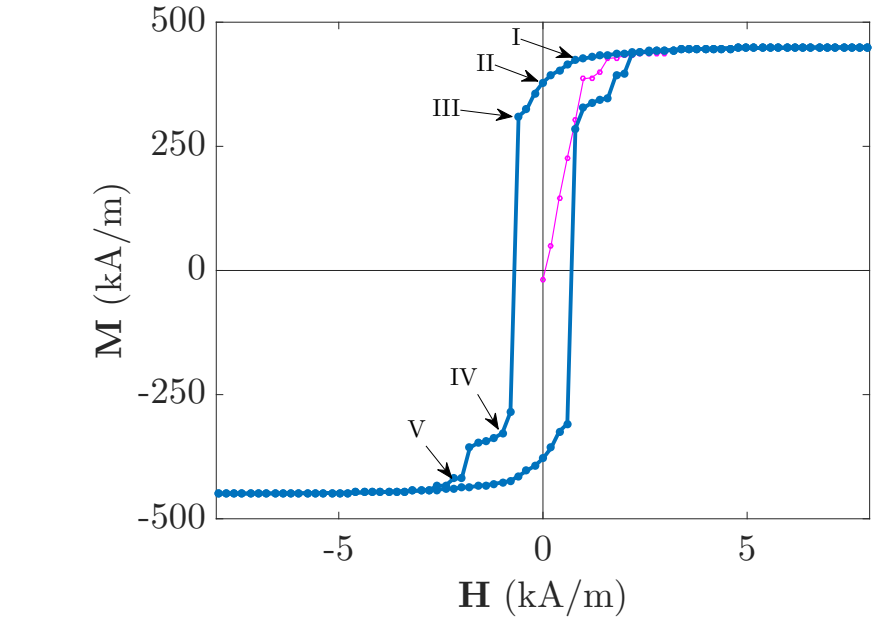


(a)

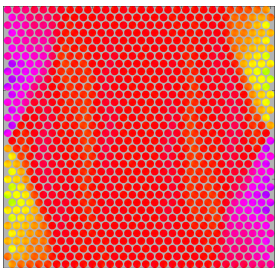

(b) I

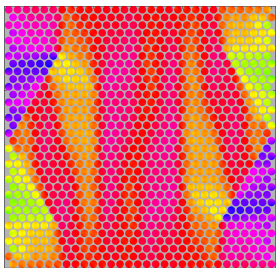

(c) II

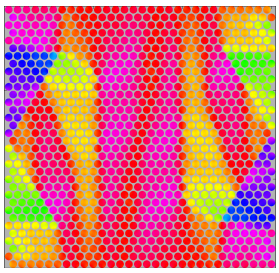

(d) III

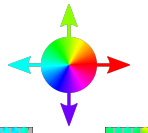

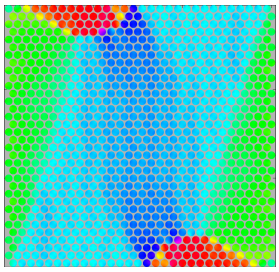

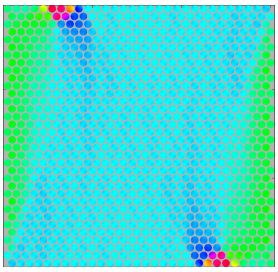

(e) IV (f) V

Figure 5.14: Hysteresis of the hexagonal array along the [110]-direction (a) with the magnetic profile of the array at different points of the hysteresis loop (b-f). The pink curve in the hysteresis loop was the virgin magnetization curve.

number of steps, and was in general more similar to the hysteresis loop of typical soft magnetic materials. A very abrupt transition from magnetization in the [110]-direction to the $[\bar{1}\bar{1}0]$-direction was found. Once again, we looked at the magnetic profile to understand

Table 5.1: The coercive field and remanent magnetization along the [110]-direction for the square and hexagonally stacked arrays respectively.

| | $\boldsymbol{H}_c$ (kA/m) | $\boldsymbol{M}_r$ (kA/m) |
|---|---|---|
| Square | 0.518 | 70.276 |
| Hexagonal | 0.700 | 378.609 |

what was going on. The magnetic microstructure at points I-V in Figure 5.14a are shown in Figures 5.14b-5.14f. The pink curve was the virgin magnetization curve.

Starting with the fully saturated array (not portrayed here) in the top right corner of Figure 5.14a, and moving towards point I, the domains nucleated and formed along the vertical edges. The magnetic structure clearly showed that the hexagonal array imposed some magnetic anisotropy. Moving to points II and III, the magnetic profile became more chaotic, until a sudden shift occurred between points III and IV. The small plateau close to point IV transitioned into point V by 180° rotation of the red areas in Figure 5.14e, and growth of the left-pointing domains.

The mechanism of magnetization reversal for the hexagonal array seemed to be composed of both domain wall motion and single-domain coherent rotation, due to appreciable magnetization perpendicular to [110] around $\boldsymbol{H} = 0$, $\boldsymbol{M}_\perp \approx 45\,\mathrm{kA/m}$. This was not the case for the square stacked array, which showed at most $\boldsymbol{M}_\perp \approx 0.1\,\mathrm{kA/m}$ at $\boldsymbol{H} \approx 0.7\,\mathrm{kA/m}$. Hence, the mechanism of magnetization reversal was domain wall motion (or domain growth), not single-domain coherent rotation. This was apparent in the magnetic microstructure in Figures 5.13b to 5.13d. The type of domain nucleation and growth exhibited by the square lattice has also been called antiferromagnetic fanning [22], and was demonstrated in simulations of rectangular grids of magnetic permalloy nanoparticles. It was explained in terms of the multistability of the system, where metastable intermediate states were formed with successively reversed dipole-chains. The mechanisms of magnetization reversal for the square lattice were therefore very different from the ones present in the hexagonal lattice.

The discrete steps of the hysteresis loop of the square lattice were a characteristic not usually encountered in continuous magnetic materials. Steplike hysteresis curves have been found in theoretical work on 1D Ising spin chains with antiferromagnetic interactions [4]. Ising models in multiple dimensions with mixed interactions generally exhibit first-order transitions [20, 19], and magnetic ordered phases commensurate with the underlying lattice. Self-similar hysteresis curves with step-like behavior have been calcu-

lated theoretically for Ising models [65, 24], and have also been identified in simulations of dipole-dipole coupled square lattices [22]. Hence, our square stacked array shared some of the its characteristics with Ising models, making it an interesting objective of study also for fundamental physics purposes. Our simulated arrays were however more complex than Ising models, since each magnetic element had an uncountable number of possible states (i.e. magnetization in any possible direction), but in practice, most elements typically took on one of four states (magnetization in the up/down/right/left direction), which partly explained its hysteretic similarity with Ising model systems.

The step-like behavior could also be understood in terms of phase transitions, from the SAF phase to the SFM phase, which is metastable on the square lattice [23]. The symmetry of the two different phases belong to different fundamental groups, hence the phase transition between the two must be of the first order, which in turn could explain the abrupt shifts in magnetic structure between the steps in the hysteresis loop.

For the hexagonal lattice, no such phase transitions took place. The SAF ordered phase was not stable (nor metastable) on the hexagonal lattice, hence the hysteresis loops exhibited no sharp transitions, apart from the large transition from point III to IV in Figure 5.14a, attributed to magnetization reversal by coherent rotation. The steps that took place between points IV, V and the saturated states were more likely a result of domain pinning, due to the finite size of the array.

We have seen that the symmetry of the superlattice can have profound effects on the exhibited hysteresis of the system. The phase transition from SAF ordered to SFM ordered magnetization in the square lattice may have been aided by the fact that the symmetry of the applied field coincided with the superlattice symmetry. Therefore, we simulated hysteresis loops along axes that were not high-symmetry ones, to see what effect this had on the hysteretic properties of the arrays. We chose the [010]-direction, since this was a hard axis for the nanomagnets and an axis of low symmetry for the arrays in general. For the square array, this was precisely the diagonal of the array, but that was not the case for the hexagonally stacked array, since it was only approximately square. All parameters were otherwise the same as for the previous hysteresis simulations. Calculated values of $\boldsymbol{H}_c$ and $\boldsymbol{M}_r$ along these directions are given in Table 5.2.

The hysteresis loop of the square array along the given axis is shown in Figure 5.15a. Multiple points, I-VI, are marked on the hysteresis loop, and the corresponding magnetic microstructures are given in Figures 5.15b-5.15g.

Starting at the bottom left of the hysteresis loop, the array was completely saturated

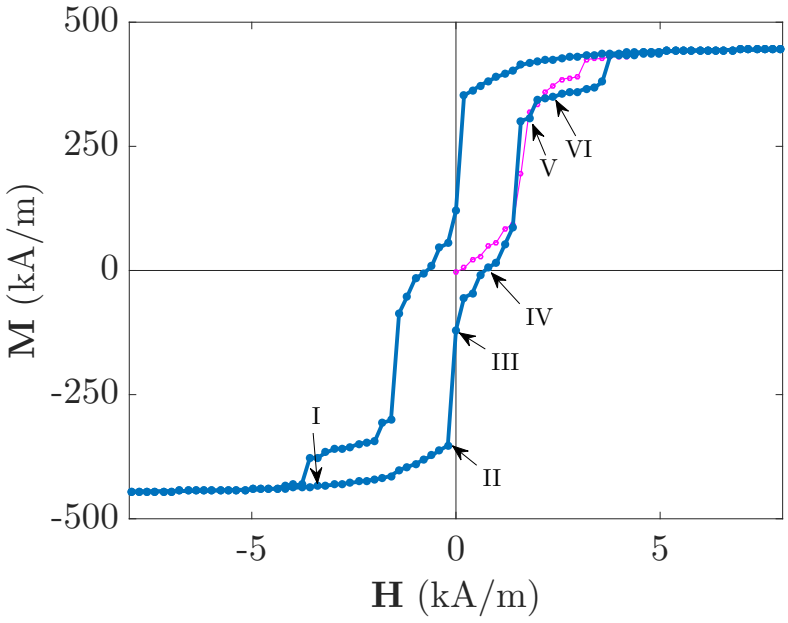


(a)

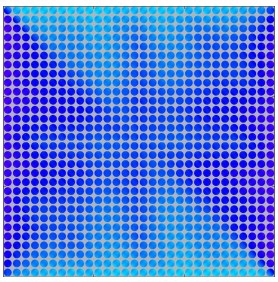

(b) I

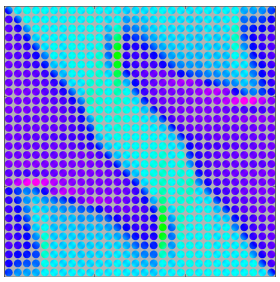

(c) II

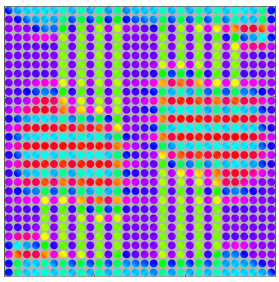

(d) III

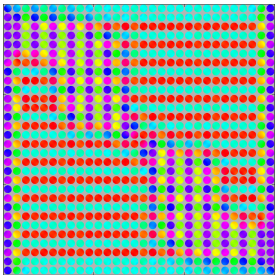

(e) IV

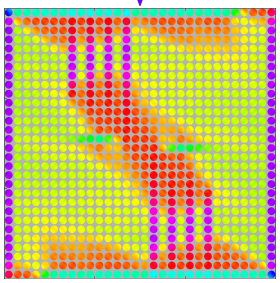

(f) V

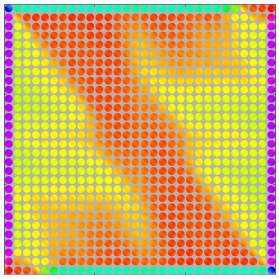

(g) VI

Figure 5.15: Hysteresis of the square array along the [010]-direction (a) with the magnetic microstructure at different points of the hysteresis loop (b-g). The pink curve in the hysteresis loop was the virgin magnetization curve.

towards the bottom left corner of the array. As the field was gradually increased through point I and all the way to point II, a rather interesting domain structure emerged. The

"Z-domain" has previously been reported in thin, square micromagnets of LSMO [58], but in that case, the thin film was continuous. The change in applied field between points II and III was only 0.25 mT, but a large reduction of the magnetization took place nonetheless. This was accompanied by a transition from mostly SFM coupling between the nanomagnets, to mostly SAF coupling. Moving on to point IV, the newly formed domains grew. The horizontally aligned domains seemed to grow more than the vertically aligned ones. The large transition after point IV to points V and VI involved reformation of the Z-domain, first in a flawed fashion, illustrated in V, and then a more complete Z-domain, as shown in VI. The array saturated after the final step after point VI.

Table 5.2: The coercive field and remanent magnetization along the [010]-direction for the square and hexagonally stacked arrays respectively.

| | $\boldsymbol{H}_c$ (kA/m) | $\boldsymbol{M}_r$ (kA/m) |
|---|---|---|
| Square | 0.709 | 120.172 |
| Hexagonal | 0.362 | 409.787 |

The magnetic microstructure of the square array during hysteresis showed evidence of the same types of phase transition from a SFM ordered phase at large applied fields, to a SAF ordered phase at lower fields, as was observed during the previously described hysteresis simulations. Transition from the SFM ordered (multidomain) Z-domain state in Figure 5.15c to the mostly SAF ordered state in Figure 5.15d happened by antiferromagnetic fanning. The SAF domains nucleated at critical points of the Z-domain, i.e. in the neckings of the Z and the sharp corners of the ends of the Z. Since the applied field was not parallel to one of the primitive directions of the lattice, the metastable intermediate states did not involve subsequent switching of whole dipole chains, but instead formation of a polydomain SAF state, with magnetization aligned in horizontal and vertical directions. Nevertheless, subsequent switching of partial dipole chains did occur, which lead to the non-linear nature of the hysteresis curve between points II and VI. This seemed to suppress the pronounced step-like hysteretic behavior previously observed (i.e. larger steps with approximately constant magnetization). The plateau around point VI in Figure 5.15a occurred due to delayed switching of the edge rows and columns of magnets, which may have been a finite size effect.

Hysteresis of the hexagonal array along the [010]-direction is shown in Figure 5.16a, with corresponding magnetic microstructures in Figures 5.16b-5.16e. The shape of the hysteresis curve was similar to that shown in Figure 5.14a, but with more abrupt transitions. The hysteresis loop was not completely symmetric about $\boldsymbol{H} = 0$.

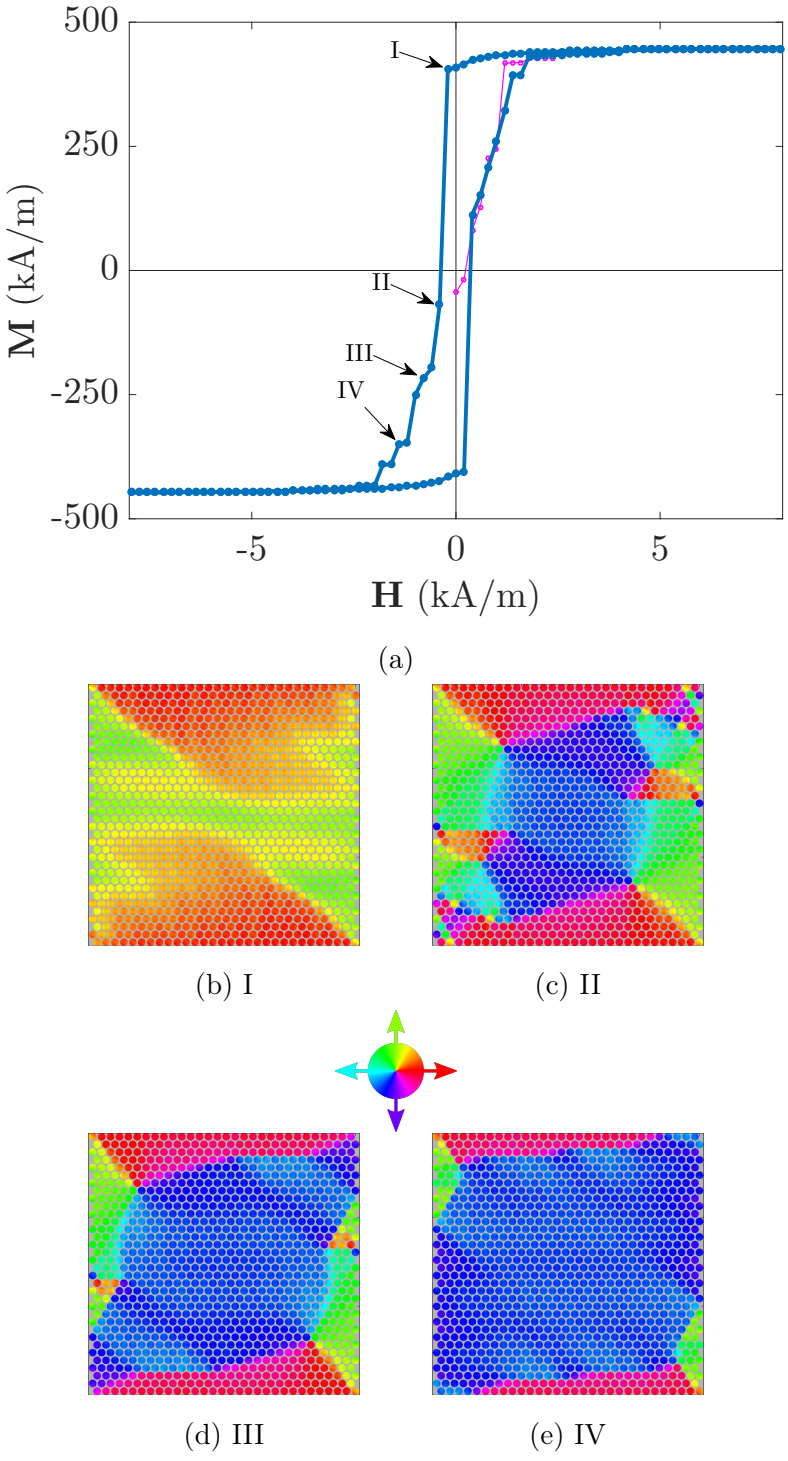


(a)

(b) I

(c) II

(d) III

(e) IV

Figure 5.16: Hysteresis of the hexagonal array along the [010]-direction (a) with the magnetic microstructure at different points of the hysteresis loop (b-e). The pink curve in the hysteresis loop was the virgin magnetization curve.

Starting in the top right corner of the hysteresis loop, the array was completely saturated towards the top right corner. Moving towards point I, a quasi-Z-domain formed. Unlike the Z-domain shown in Figure 5.15c, this Z-like domain did not have as well defined

borders, and a broken neck. The reason for this may have been the lattice-induced magnetic anisotropy, which seemed to stabilize magnetization along all the six directions of high-symmetry for the array. The square array clearly showed only four preferential directions of magnetization, i.e. the primitive lattice vectors, which were also the easy axes of the LSMO nanomagnets.

After point I, a sharp transition took place, leading to points II and III. Here, the central part of the array had flipped its direction of magnetization by approximately 180°. The magnetization was further reduced by growth of the flipped domain, until point IV was reached. At this point, most of the array had a magnetization towards the bottom left corner, with small opposing domains on the top left and bottom right corners of the array. After point IV, the array saturated, by shrinkage of the opposing domains.

The broken neck of the quasi-Z-domain exhibited by the hexagonal array, Figure 5.16b, was probably caused by the superlattice-induced anisotropy. The easy axes of the nanomagnets favored the horizontal and vertical directions, but a significant part of the array exhibited magnetization in directions other than these four. Comparing it to the Z-domain of the square lattice, Figure 5.15c, we saw that in the latter case, the entire Z-domain exhibited the same direction of magnetization, which coincided with one of the primitive directions of the lattice. In the hexagonal lattice, there was a gradual rotation of the magnetization within the Z-like domain. Another important feature was the asymmetry of the hysteresis loop. Whereas the [010]-direction was precisely the diagonal of the square lattice, it was not for the hexagonal array, since the full array was only approximately square. This was most likely the reason for the asymmetric switching behavior. The mechanisms of magnetization reversal were assumed to be unchanged.

### 5.2.7 Indications of glassy dynamics from quenched disorder

When simulating the magnetic ground states of the two different arrays, we performed both temperature relaxations and quenched relaxations. The two different simulation procedures yielded quite different results.

Two of the magnetic ground states of the square array are shown in Figure 5.17. Figure 5.17a shows the magnetic ground state of the array after quenched relaxation, whereas Figure 5.17b shows the magnetic ground state of the array after temperature relaxation. Both arrays were initialized to the same random configuration, so the only difference was the relaxation scheme. The quenched relaxed array exhibited a much higher degree of disorder, with polydomain and vortex state nanomagnets, compared to the temperature

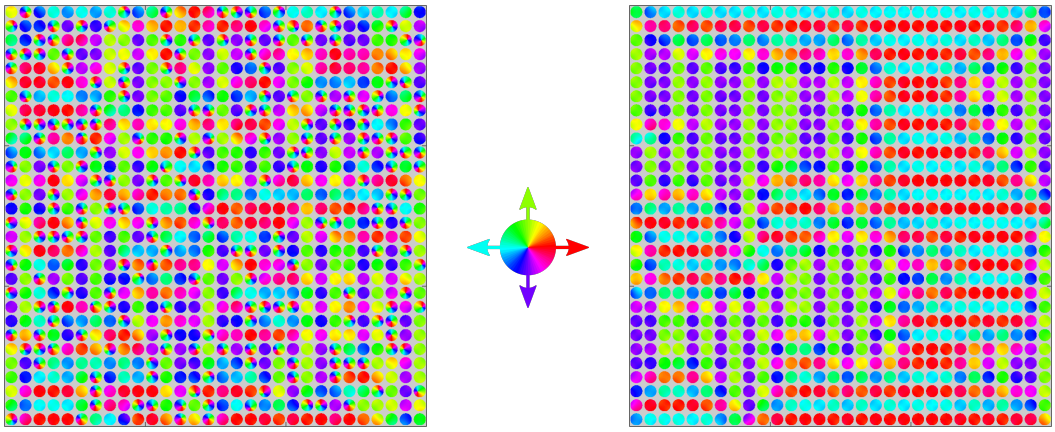

(a) (b)

Figure 5.17: The magnetic ground state of the square array after (a) quenched relaxation and (b) temperature relaxation. Both arrays had the exact same material parameters and geometry, and were initialized to the same random configuration. The arrays were $1.8\,\mu m \times 1.8\,\mu m$, with 5 nm thick nanomagnets.

relaxed array. This was indicative of glassy dynamics, since the final ground state was dependent on the specific path taken through phase space. Equilibration of spin-glasses has been explained in terms of stochastic motion in phase space combined with a hierarchical distribution of free energy barriers [60]. The effect of the hierarchical distribution of free energy barriers is a wide range of characteristic time scales [45, 34], where relaxation of one part of the system depends on the state of the rest of the system. Although we cannot say that our system exhibits such features with certainty, there is definite indication of glassy dynamics in the square lattice. The quenched relaxation did after all lead to a ground state of significant frustration and disorder. We know from Chapter 4 that single LSMO nanomagnets of the relevant size exhibited the monodomain ground state as the most stable magnetic ground state. Such prevalence of single magnet vortex ground states could be taken as evidence of metastability and hierarchical constrained dynamics. To illustrate the concept, consider one of the vortex state nanomagnets in Figure 5.17a. Each vortex was typically surrounded by nanomagnets with magnetization in different directions. The vortex was prohibited from relaxing to the more stable monodomain state before the surrounding nanomagnets had relaxed to a more ordered SAF state (i.e. formed dipolar chains), but the slow dynamics of the transition meant that it was blocked on the time scale of the simulation. Therefore, a metastable and disordered ground state was realized, instead of the more ordered ground state in Figure 5.17b.

One quenched and one temperature relaxed ground state for the hexagonal array are shown in Figure 5.18. Both were initialized to the same random configuration. The

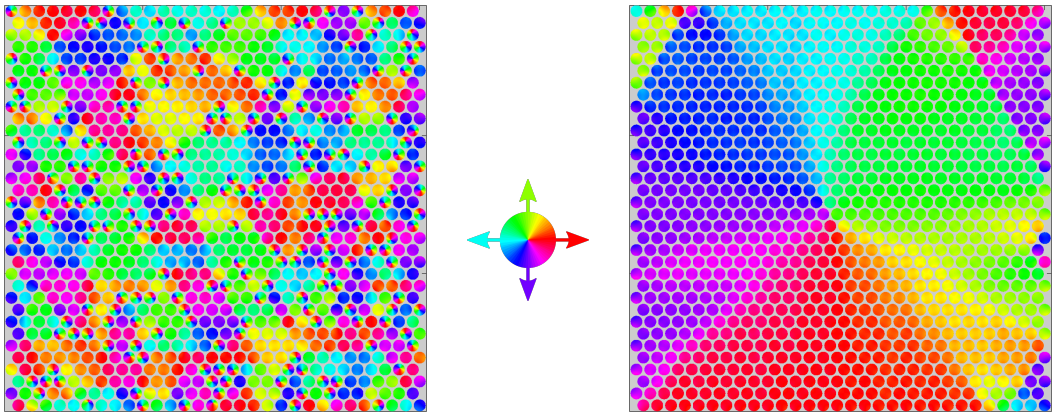

(a) (b)

Figure 5.18: The magnetic ground state of the hexagonal array after (a) quenched relaxation and (b) temperature relaxation. Both arrays had the exact same material parameters and geometry, and were initialized to the same random configuration. The arrays were 1.8 µm × 1.8 µm, with 5 nm thick nanomagnets.

quenched array, Figure 5.18a, exhibited significantly more disorder than the temperature relaxed one in Figure 5.18b. Clusters of SFM ordered nanomagnets did form, and some long-range order seemed to be present by inspection, but the temperature relaxed array exhibited a highly ordered quasi-Landau state, without any single magnet vortices. The difference was remarkable. The reasons for the difference in ground state was assumed to be the same as for the square array. Investigations into the spin-glass dynamics of the two arrays seemed then like the next natural step.

### 5.2.8 Field-cooled and zero-field-cooled magnetization as evidence of spin-glass dynamics

The field-cooled and zero-field-cooled magnetization are well suited quantities for discerning how magnetic behavior changes with temperature. Most importantly, these quantities are used to characterize spin-glass behavior [27]. Typical spin-glass-like behavior includes irreversibility, magnetic relaxation or aging, and certain characteristics in the ac susceptibility.

In order to investigate the possible spin-glass properties of the arrays, we performed simulations to find the zero-field cooled (ZFC) magnetization, as well as the field-cooled magnetization measured during cooling (FCC) and the field-cooled magnetization measured during warming (FCW). These quantities were denoted $M^{\mathrm{ZFC}}$, $M^{\mathrm{FCC}}$ and $M^{\mathrm{FCW}}$

respectively.

The procedure for simulating $M^{\mathrm{ZFC}}$ was as follows. First, the sample was temperature relaxed, as described in Section 3.4, from a random configuration to a temperature of 25 K in zero applied DC magnetic field. Following the cooling, a weak DC magnetic field was applied in order to probe the magnetization of the array. We performed two different simulations with applied fields $\mu_0 H = 1\,\mathrm{mT}$ and 5 mT along the $[\bar{1}10]$-direction. The average magnetization was measured along the same axis as the applied field while the temperature was gradually increased by adjusting $M_S$ and $K_{\mathrm{c1}}$ and performing energy minimizations.

The simulation procedures for $M^{\mathrm{FCC}}$ and $M^{\mathrm{FCW}}$ were similar, except that the field was applied during the initial cooling process. When measuring $M^{\mathrm{FCC}}$, the average magnetization was recorded as the sample was cooled, whereas for $M^{\mathrm{FCW}}$, the array was first cooled in the same fashion as for $M^{\mathrm{ZFC}}$, and average magnetization was recorded as the system was gradually heated.

The results from simulating FCC, FCW and ZFC magnetization curves of the square array are shown in Figure 5.19. At a field of 1 mT, Figure 5.20a, a large irreversibility between FCC/FCW and ZFC magnetization was observed. The irreversibility did in fact persist throughout the entire temperature range of simulations. This was more obvious in the normalized plots, given in Appendix B.4. Nevertheless, $M^{ZFC} \approx M^{FCC} \approx M^{FCW}$ for temperatures of 340 K and above. This was very close to the paramagnetic limit of LSMO, and it was in fact observed that the FCC simulation exhibited a fully superparamagnetic array at 360 K, where even the external field was insufficient to induce magnetic ordering. This was not the case for the FCW simulation, most likely due to memory effects. In the FCC case, the nanomagnets were aligned prior to increasing the temperature to 360 K, as opposed to the FCC case, where the nanomagnets were relaxed from a random configuration in the applied field at 360 K.

In fact, irreversibility was also observed between the FCC and FCW curves. This hysteretic behavior is indeed indicative of spin-glass-like behavior. Irreversibility between FCC and FCW magnetization has been observed for superconducting $YBa_2Cu_3O_{7-\delta}$ (YBCO) single-crystals [66]. The phenomenon was explained in terms of the properties of semiconducting spin-glasses, which indicated that the system exhibited weak and short-ranged spin-glass coupling. Although LSMO is a very different material from YBCO, the hysteretic behavior of the field-cooled magnetization does suggest such weak and short-ranged spin-glass coupling. This explanation of the irreversibility can be further supported by the nature of the finite square lattice, which enforces short-ranged order

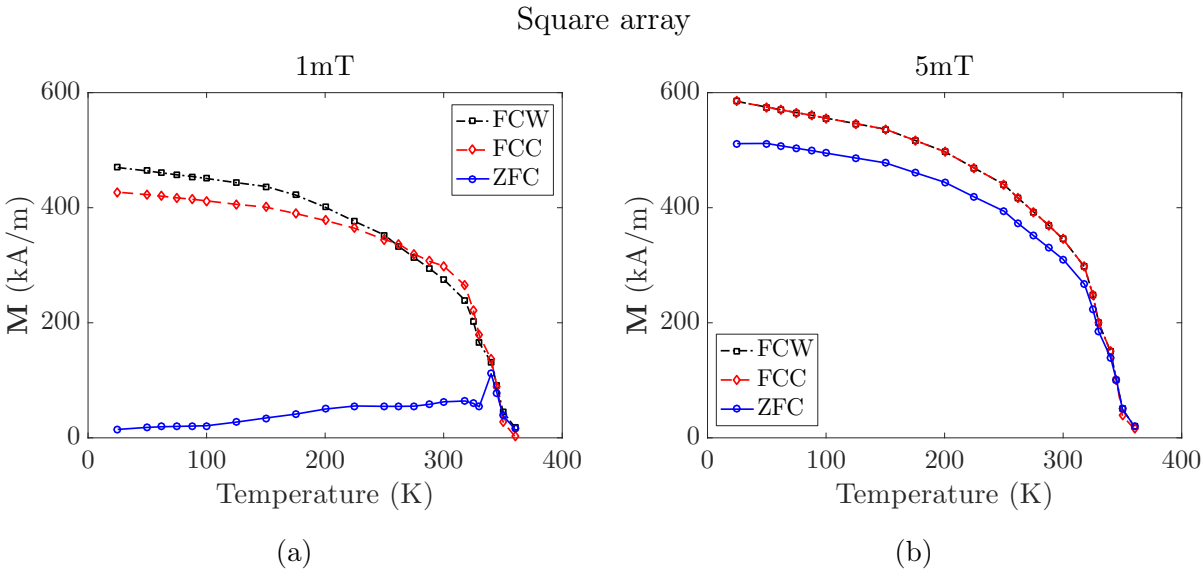


Figure 5.19: Plots of the "zero-field cooled" (ZFC), "field-cooled measured upon cooling" (FCC) and "field-cooled measured upon warming" (FCW) magnetization of the square lattice. The applied fields were (a) $\mu_0 H = 1\,\mathrm{mT}$ and (b) $\mu_0 H = 5\,\mathrm{mT}$.

and metastability.

The peak in the ZFC magnetization at 340 K indicated that the dipolar interactions between the particles were insufficient to induce supermagnetic ordering at this point. A peak in the ZFC magnetization is typical for metastable magnetic system, and usually suggestive of either superparamagnetic or spin-glass behavior [48]. If canonical spin-glass behavior was present, the peak in the ZFC magnetization would however be accompanied by a local minimum in the field-cooled magnetization [5], which was not the case here.

Results from simulations with the stronger field, Figure 5.19b, also showed irreversibility of the ZFC versus FCC and FCW magnetization. The onset temperature of irreversibility was approximately equal. Significantly higher magnetization was achieved here. The square array was in fact far from completely saturated with the weak probing field, which was a finite size effect, but with the stronger probing field, full saturation was reached approximately at the irreversibility temperature.

The resulting FCC, FCW and ZFC magnetization of the hexagonal array is shown in Figure 5.20, for both fields. At a field of 1 mT, Figure 5.20a, the zero-field-cooled versus field-cooled magnetization exhibited similar irreversibility as exhibited by the square array with the weak field. One peculiarity was the first measuring point at 25 K, where the magnetization was negative. This was most likely a random effect, since the array was

relaxed from a random configuration in zero field. The interesting part was that the applied field was unable to induce a positive magnetization, which indicated that the array was blocked. When inspecting the magnetic ground state of the array at 25 K, there was definite SFM order, and the subsequent ground states at higher temperatures displayed similar order, but with incrementally increasing magnetization along the applied field. There did not seem to be appreciable motion of domains, supporting the notion that the magnetization of the array was blocked at low temperatures. There was virtually no irreversibility of the FCW versus FCC magnetization.

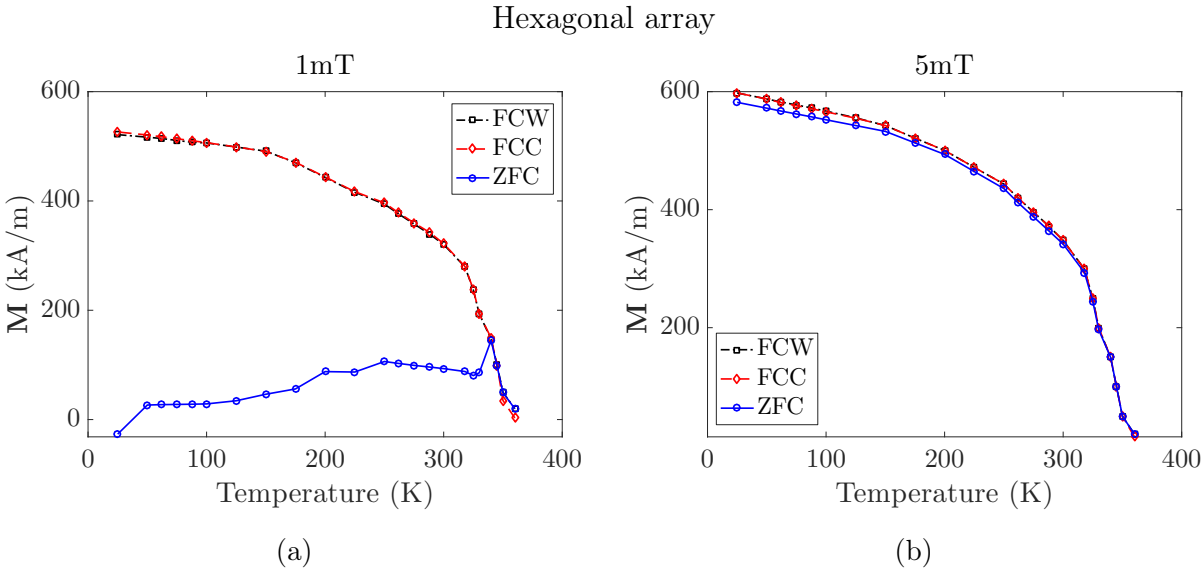


Figure 5.20: Plots of the "zero-field cooled" (ZFC), "field-cooled measured upon cooling" (FCC) and "field-cooled measured upon warming" (FCW) magnetization of the hexagonal lattice. The applied fields were (a) $\mu_0 H = 1\,\mathrm{mT}$ and (b) $\mu_0 H = 5\,\mathrm{mT}$.

The temperature of irreversibility was somewhat lower for the 5 mT probing field, but not by more than 10 K to 20 K. The difference in magnetization between the zero-field-cooled magnetization and either of the field-cooled ones was very small, but the characteristics were similar to the square array. The important difference was that the magnitude of the magnetization induced in the hexagonal array was larger, meaning that the hexagonal array had a larger susceptibility.

The ZFC, FCC and FCW magnetization of the square array did show spin-glass-like behavior, but they did not provide ample grounds for discerning the underlying reason of this behavior. It does seem unlikely that this behavior arose from a true SSG phase, since the square array was completely regular in the structural sense. Therefore, it may seem more likely that the spin-glass-behavior was caused by weak, short-range spin-glass coupling, forming between clusters of superspins. Cluster-glass-like properties have been

reported for ferromagnetic systems [33], where the magnetocrystalline anisotropy was identified as the underlying reason. The irreversibility of the magnetization did however persist up to temperatures above 300 K, where the magnetocrystalline anisotropy was very weak. It is possible that a superlattice-induced anisotropy could be involved in this behavior, but we were not able to pursue this idea further, due to the limited time-frame of this work.

Seemingly, spin-glass-like behavior was also present for the hexagonal array. In particular the irreversibility of ZFC versus FCC or FCW magnetization was as pronounced in the hexagonal array as in the square, at low fields. The higher susceptibility of the hexagonal array lead to a larger degree of magnetization, but phenomenologically, there was no particular reason to assume that the underlying mechanism behind this behavior was different in the hexagonal array compared to the square one. In fact, in the hexagonal array seems like a more likely candidate for cluster-glass behavior, since the SFM ordered domains, in combination with the strong magnetocrystalline anisotropy, may introduce the necessary disorder and frustration to realize the glassy traits of a cluster-glass. Our simulations were however not comprehensive enough to say anything for certain.

## 5.3 Summary of findings

Based on our findings in Chapter 4, we chose to use 5 nm thick nanomagnets, with a diameter of 50 nm for the regular arrays discussed in this chapter. The choice was based on two considerations. Firstly, we wanted to maximize the probability of achieving supermagnetic ordering in the arrays, and secondly, we wanted to keep dimensions as large as possible so that the structures were feasible to manufacture in the laboratory.

Supermagnetic ordering and the magnetic properties of ordered nanomagnet arrays was explored. We first investigated how the supermagnetic ground states of ordered arrays could be tailored by controlling the stacking of the arrays. We simulated two types of regular, finite lattices, namely the square lattice and the hexagonal lattice. The former exhibited SAF ground states and the latter SFM ground states. The ground states were however characterized by disorder and non-uniqueness. The superlattice structure had direct effects on the directions of magnetization, through an apparent lattice-induced magnetic anisotropy. Especially the SFM ground states were reminiscent of the type of magnetization exhibited by significantly larger thin films of LSMO (i.e. blanket film magnetic texture). This phenomenon was attributed to the exchange decoupling between individual nanomagnets.

We used Fourier analysis to statistically quantify the interparticle coupling in the two different arrays. On average, the interparticle coupling of the square array was of the superantiferromagnetic character, with alternating dipole-chains. The dipole-chains were arranged head-to-tail, with neighboring chains in opposite directions. The finite size of the lattices lead to multiple domains. The average interparticle coupling of the hexagonal array was of the superferromagnetic kind, where neighboring nanomagnets were aligned (although with multiple domains present).

We saw that the analysis method we developed based on Fourier analysis was well suited for characterizing the periodicities in the magnetization of the arrays. The method clearly separated SFM from SAF ordering. Information on domain sizes or strength of coupling was however not obtainable using the method. We did not achieve a single quantity that could be used as an order parameter either, as we initially hoped.

Simulations of arrays with periodic boundary conditions showed that the SAF order of the square array increased when finite size effects were excluded, whereas the opposite was true for the SFM ordered hexagonal array. This was explained by the nature of the forces responsible for the supermagnetic ordering of the arrays. Based on a heuristic argument, we deduced that the interparticle interactions were of the short-ranged kind in the square array and long-range in the hexagonal array.

An investigation of how an applied field could be used to control the supermagnetic ground state was performed. We saw that especially the square array was sensitive to the initial conditions, and could form remanent states with high or low macroscopic magnetization based on which direction the array was magnetically saturated. This was explained by switching between SAF and SFM ordering of the array, which was dependent on the initial direction of magnetization.

We explored the hysteretic behavior of the ordered arrays along high-symmetry axes. We saw that the symmetry of the superlattice had profound effects on the shape of the hysteresis curve. The square array exhibited well-defined discrete steps in the magnetization. The result was explained in terms of 2D Ising spin-lattices and supermagnetic phase transitions. The symmetry of the SFM and SAF phases on the square lattice belonged to different fundamental groups, therefore we argued that the phase transition must be of the first order. No such phase transitions took place in the hexagonal array during hysteresis simulation. The hysteresis loop resembled those of typical soft magnetic materials. The abrupt changes in magnetization were attributed to magnetization reversal by coherent rotation in combination with domain pinning because of the finite nature of the array. The mechanism of magnetization reversal for the square array was

found to be antiferromagnetic fanning in combination with the before-mentioned phase transitions.

Hysteresis along low-symmetry axes was simulated to further classify the effects of the superlattice structure on the hysteretic properties. The square lattice exhibited phase transitions and an interesting multidomain SFM state called the "Z-domain" state (a Z-domain-like state also formed in the hexagonal array). The fact that the applied field did not coincide with the primitive directions of the superlattice seemed to suppress the formation of the pronounced, discrete steps previously observed for the square array. The hexagonal array exhibited similar hysteretic properties as previously observed. The most interesting feature was the asymmetry of switching, which was explained by the fact that the hysteresis direction was not the true diagonal of the hexagonal array (as it was for the square array).

Finally, spin-glass properties of the arrays were explored. Comparison of quenched relaxations to temperature relaxations of the two arrays indicated the presence of glassy dynamics, due to the significantly increased magnetic disorder of the quenched relaxed arrays. The large difference in ground state for the two simulation procedures was explained in terms of spin-glass dynamics, i.e. hierarchical constrained dynamics.

Field-cooled and zero-field cooled magnetization simulations of the two arrays were then performed to further characterize the spin-glass behavior of the systems. Both arrays exhibited irreversibility between field-cooled and zero-field cooled magnetization, which was suggestive of spin-glass behavior, but no local minima in the field-cooled magnetization was found. Therefore, we concluded that no canonical superspin-glass phase formed, but that the behavior may have arisen from cluster-glass interactions or possibly magnetocrystalline and super-lattice induced anisotropy. The square array also exhibited irreversibility between FCC and FCW magnetization. This feature was reminiscent of semiconducting spin-glasses, which suggested that weak and short-ranged spin-glass interactions were present in the square array. Supermagnetic ordering persisted to well above room temperature.

# Chapter 6

# Conclusions and outlook

We have investigated how supermagnetism may be manifest in patterned thin films of LSMO. First, we explored the superparamagnetic regime of single LSMO nanomagnets. We found superparamagnetism in 5 nm thick, cylindrical LSMO nanomagnets, with diameters from 20 nm to 140 nm. Based on our results, we designed ordered arrays of LSMO nanomagnets of the relevant thickness, where each nanomagnet had a diameter of 50 nm. Two superlattice structures were investigated, namely the two-dimensional square and hexagonal Bravais lattices. The former exhibited superantiferromagnetic ordering, and the latter superferromagnetic ordering. We discussed effects of finite size, exchange decoupling, and the response to applied fields. Hysteresis simulations showed step-like hysteretic behaviour for the square lattice, explained by supermagnetic phase transitions. The hexagonal lattice exhibited more conventional hysteresis, similar to that of soft magnetic materials. Quenched disorder and magnetic irreversibility during simulation of field-cooled and zero-field-cooled magnetization was suggestive of spin-glass dynamics in the arrays. Supermagnetic ordering was found to persist to well above room temperature. Based on our investigations, we conclude that LSMO thin film systems seem like a good candidate for fabricating and experimentally exploring supermagnetism and supermagnetic ordering in solid state systems.

This explorative study of supermagnetism in patterned thin films of LSMO has elucidated some of the possibilities of engineering magnetic materials with an unprecedented control over macroscopic magnetic properties, and materials with properties that do not exist in nature may also be within reach. The study was inspired by research articles by Varón et. al [64, 63] and Jordanovic et. al [26]. While these studies simulated arrays of magnetic particles under the assumption that each particle was in fact monodomain, and could be treated as a superspin, we made no such simplifying assumptions. In addition,

we explored phenomena beyond the scope of their studies, and we performed a large number of simulations for all our systems, to ensure that our results were not caused by randomness. We argue that this lends extra credibility to our study, especially since our results agree with and can be explained in terms of previous results.

Conventional magnetic material engineering is typically limited by the intrinsic properties of the magnetic material. The strength of the exchange interaction and the magnetocrystalline anisotropy cannot be controlled unless by chemically altering the material, and the results are not easily predicted. By creating superstructures of nanomagnetic elements, a much larger set of parameters can be controlled.

By controlling the size, shape and orientation of the individual array elements, the magnetodynamic properties of each elements can be fine-tuned [21]. For instance, by making elliptic nanomagnets, instead of circular ones, a perceived uniaxial magnetic anisotropy can be engineered. By combining control of individual elements with control over the superstructure of the ordered arrays, it is possible to create novel materials for technical applications, but also for research purposes.

2D dipolar lattices have previously been a subject of theoretical studies [31, 24], but may now be experimentally realized in a controlled manner. Work by Fraerman [23] has shown that the dipolar interactions in regular dipole lattices mimic the typical magnetic interactions observed for continuous magnetic materials. It was shown that the long wave approximation of the dipolar tensor of 2D orthorhombic dipole lattices could be expanded into pseudo-anisotropy, -magnetostatic and -exchange terms. This may be a possible approach to a macroscopic continuum description of magnetic metamaterials.

Unlike theoretical dipolar arrays, which tend to become disordered even at temperatures close to zero, our simulated arrays exhibited supermagnetic ordering to above room temperature.

Supermagnetic systems may also provide a route for fundamental research into condensed matter physics. The shared characteristics between the arrays we simulated and e.g. 2D Ising models suggest that such systems may be used for probing concepts that were previously experimentally unavailable. In fact, creating artificial spin systems using nanomagnetic elements may help further explore several model systems of condensed matter physics [46].

Among the possible applications of supermagnetic phenomena are of course several magnetoelectrical devices, from data storage to sensing devices. Care must be taken if using single nanomagnets for data storage, as formation of collectively ordered magnetic phases

may compromise the independence of stored information. Hence, supermagnetism may not be used to directly overcome the superparamagnetic effect in the conventional sense, but could be utilized in novel approaches to data processing and storage. The interesting properties of supermagnetic arrays, such as the step-like hysteresis of the square array could possibly be utilized for new devices, such as multi-level memory.

Even though we obtained some results on spin-glass behavior, we could not with certainty say that the system of study exhibited glassy dynamics. Performing dynamical simulations of e.g. the ac susceptibility of the arrays would have provided clearer evidence, but was beyond the scope of this work. Further study of the spin-dynamics in such superlattices of nanomagnets would presumably open for other applications as well. It seems likely that the ordered arrays of nanomagnets could act as magnonic crystals, and hence be used as a basis for spintronic devices.

Further work should include simulations of magnetic ground states of unexplored 2D arrays, more specifically how the magnetic ground state changes with the rhombic angle of the array. Effects of array shape, and asymmetry of stacking should also be further explored, so that the full impact of superlattice structure may be understood. Very specific domain structures could most likely be realized by introducing regions of different stacking, or differently shaped nanomagnets. Studies of the dynamics of e.g. the SAF to SFM phase transitions would provide useful insight into dynamical behavior of supermagnetic arrays.

# Appendix A

# Methodology

## A.1 Fourier analysis of magnetization profiles

In order to quantitatively analyze the periodicities of the magnetic ground states of the different systems we have simulated in this work, we devised a method using the discrete Fourier transform (DFT). The definition of the DFT is given by

$$\hat{f}_k = \sum_{n=0}^{N-1} f_n \exp\left(\frac{-2\pi i k n}{N}\right), \tag{A.1}$$

where a sequence of complex numbers $f_n$, $n = 0...N-1$, is transformed into the N-periodic sequence of complex numbers $\hat{f}_k$, $k = 0...N-1$. The sequence of numbers, $f_n$, will in our case correspond to the discrete sampling points of the reduced magnetization, $\hat{\boldsymbol{m}}$. The (discrete) Fourier transform of $\hat{\boldsymbol{m}}$, $\mathcal{F}[\hat{\boldsymbol{m}}]$ is then the numbers $\hat{f}_k$. The Fourier power spectrum is defined as $|\mathcal{F}[\hat{\boldsymbol{m}}]|^2/N$.

The aim of the method is being able to find the average coupling between neighboring nanomagnets, by finding the average Fourier power spectrum of the parallel and perpendicular components of the magnetization along the primitive vectors of the arrays. The method is illustrated in Figure A.1. All analysis was performed using Matlab.

The two components of the magnetization were imported as numerical matrices in Matlab. In order to obtain the average spectrum, one dimensional DFTs were performed along each row, illustrated by the red arrows in Figure A.1a, and then all rows were averaged in the direction of the blue arrow. An average spectrum for both parallel and perpendicular components of $\hat{\boldsymbol{m}}$ were calculated along both the primitive directions, yielding four spectra that describe the magnetization profile. This procedure could then be repeated

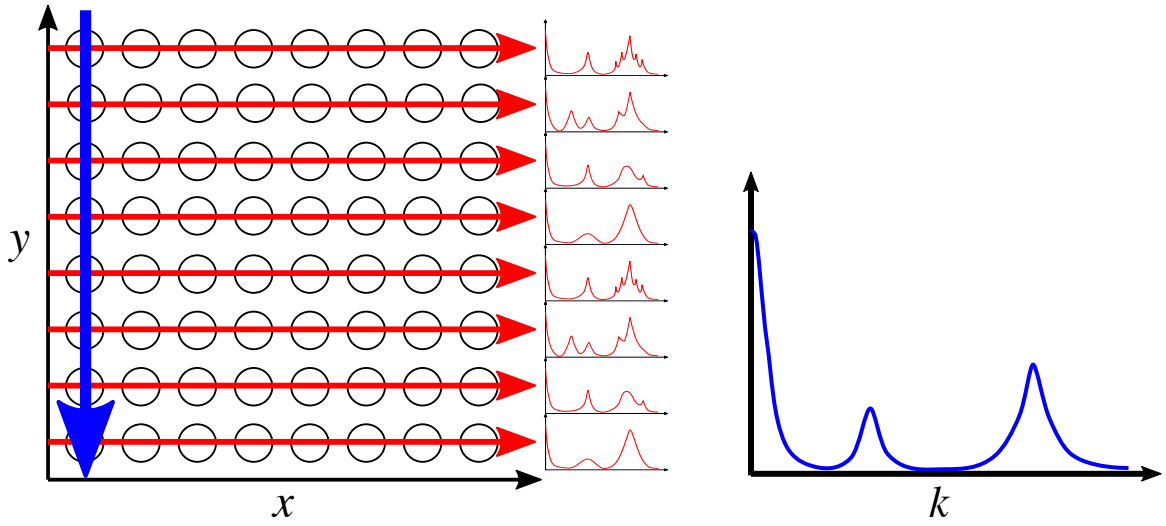


(a) (b)

Figure A.1: An illustration of how the average Fourier spectrum of the magnetization along the $x$-direction was obtained for a square array. One dimensional DFT was performed along each row in (a), illustrated by the red arrows. This yielded as many spectra as there were data points along the $y$-direction. The average spectrum, illustrated in (b), was found by averaging the Fourier spectra along the blue arrow in (a).

for as many magnetization profiles as necessary, and final average spectra could be found for the entire ensemble of magnetic ground states.

For the case of the hexagonally stacked array, the primitive lattice directions were not perpendicular. The $\boldsymbol{b}_1$- and $\boldsymbol{b}_2$-directions, as specified in Figure 5.2, formed an angle of 60°. The $\boldsymbol{b}_1$ was equivalent to the $x$-direction, so calculating the spectra of the parallel and perpendicular components of the magnetization was straightforward in this case. For the $\boldsymbol{b}_2$-direction, the numerical arrays had to be rotated by 60°, before the Fourier spectra could be calculated. The algorithm used to rotate the matrices was Matlabs built-in function `imrotate`, which used bilinear interpolation in order to determine the values of the magnetization at spatial points that didn't coincide with existing sampled points. Even though the array was stacked in a hexagonal Bravais lattice, the magnetization was sampled on a rectangular lattice, so the reciprocal lattice of Fourier transform of the magnetization was also rectangular, not hexagonal.

The frequency resolution of the Fourier spectrum is limited by the number of data points available. The size of the Brillouin zone of the regularly sampled magnetization profile is by definition equal to the inverse of the simulation cell size. Since the objective of this method was to explore the interparticle periodicities, only a small region of the Bril-

louin zone was of interest, i.e. the frequencies corresponding to relatively long wavelength signals (with wavelength equal to or longer than the interparticle spacing). For this purpose, the resolution of the spectra was unsatisfactory. In order to improve the resolution, the magnetization profiles were zero-padded, i.e. extended in both dimensions with only zeroes. This is a method of interpolating values of the Fourier spectrum between the frequency increments given by the original signal [56].

# Appendix B

# Additional results

## B.1 The free energy of different ground states

In this section, we provide the additional results not included in Section 4.2.3. The average free energy of different ground states of single LSMO nanomagnets as function of nanomagnet diameter is shown in Figures B.1 and B.2 for thicknesses of 10 nm and 15 nm respectively.

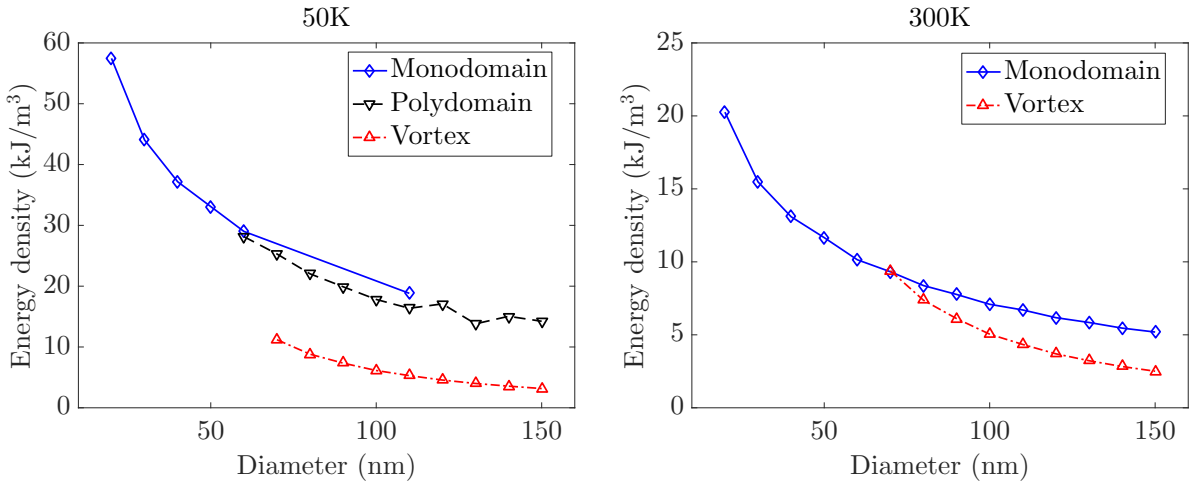


(a) (b)

Figure B.1: Average energy density of circular LSMO nanomagnets grouped after type of ground state. The thickness of the nanomagnets was 10 nm and the temperature (a) 50 K and (b) 300 K.

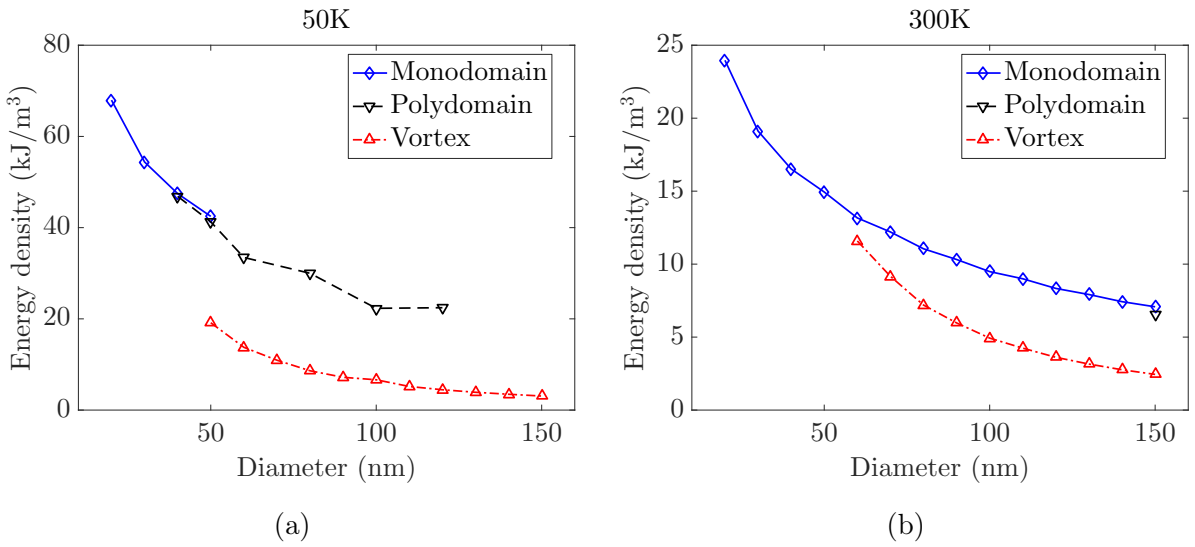


Figure B.2: Average energy density of circular LSMO nanomagnets grouped after type of ground state. The thickness of the nanomagnets was 15 nm and the temperature (a) 50 K and (b) 300 K.

## B.2 Fourier power spectra of the magnetization of the ordered arrays

In this section, we provide the average Fourier power spectra of the parallel components of the magnetization of the square array, Figure B.3, and the hexagonal array, Figure 5.7.

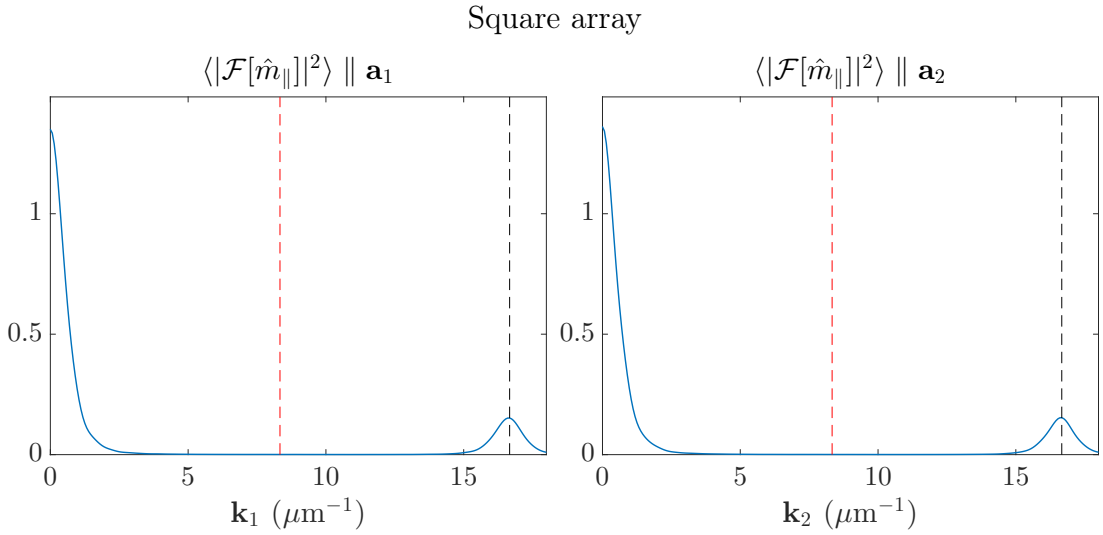


Figure B.3: Average Fourier power spectra of the parallel components of the magnetization along $\boldsymbol{a}_1$ (a) and $\boldsymbol{a}_2$ (b) exhibited DC peaks at $\boldsymbol{k} = 0$ and nearest-neighbor peaks at $\boldsymbol{k} = 16.67$, indicated by the black, vertical dashed lines.

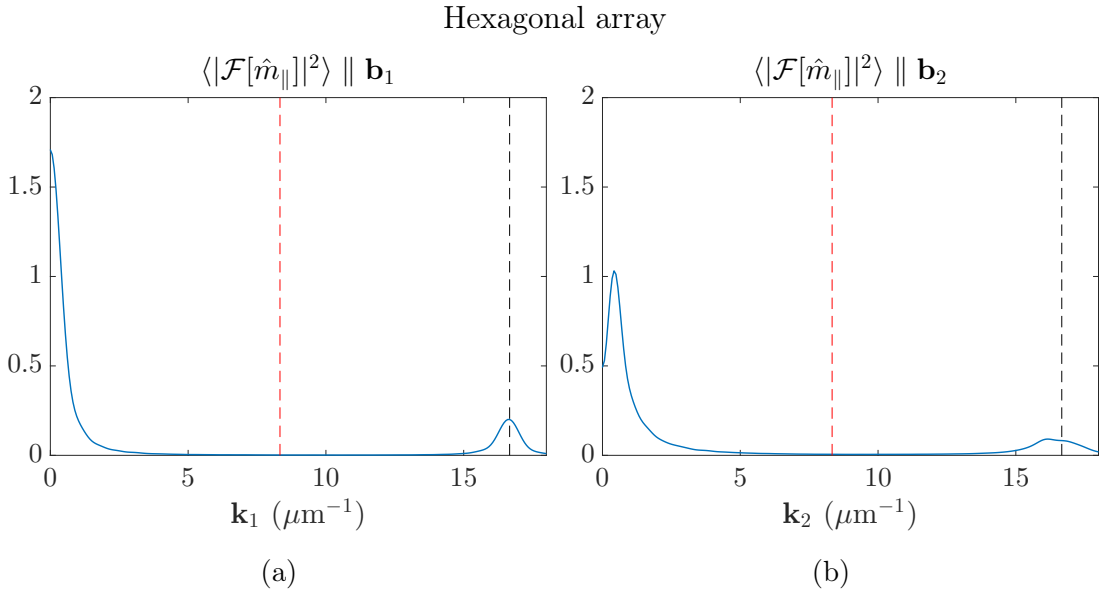


Figure B.4: Average Fourier power spectra of the parallel components of the magnetization along $\boldsymbol{b}_1$ (a) and $\boldsymbol{b}_2$ (b) exhibited DC peaks or split DC-peaks centered at $\boldsymbol{k} = 0$ and nearest-neighbor peaks at $\boldsymbol{k} = 16.67$, indicated by the black, vertical dashed lines.

## B.3 Virgin magnetization curves

In this section we show the magnetic microstructure of the square and hexagonal array and how it changed along the virgin magnetization curves. The virgin magnetization curves of the square array with corresponding magnetic microstructure simulated along the [110]- and [010]-directions are shown in Figures B.5 and B.6 respectively.

Similarly, the virgin magnetization curves of the hexagonal array with corresponding magnetic microstructure simulated along the [110]- and [010]-directions are shown in Figures B.7 and B.8 respectively.

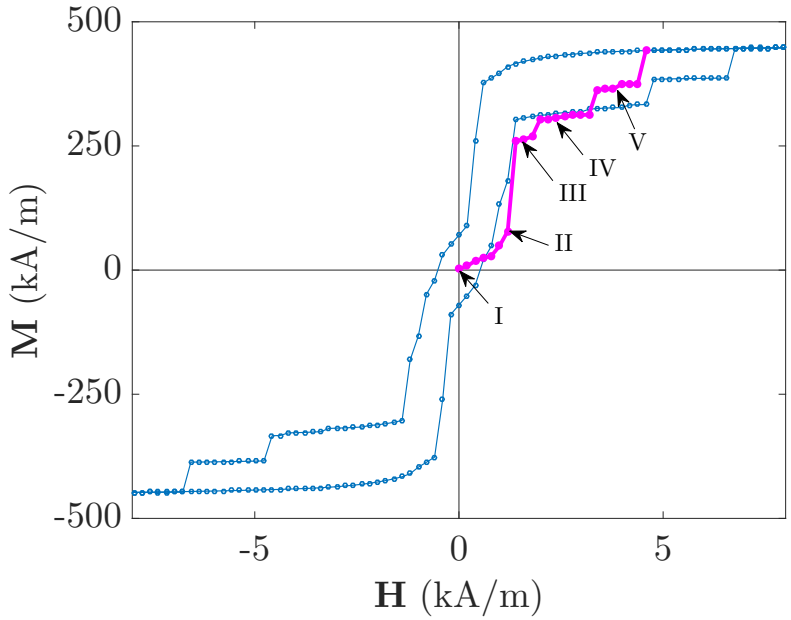


(a)

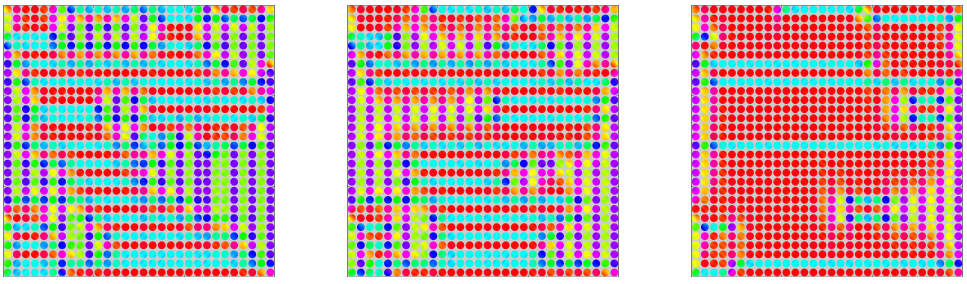

(b) I (c) II (d) III

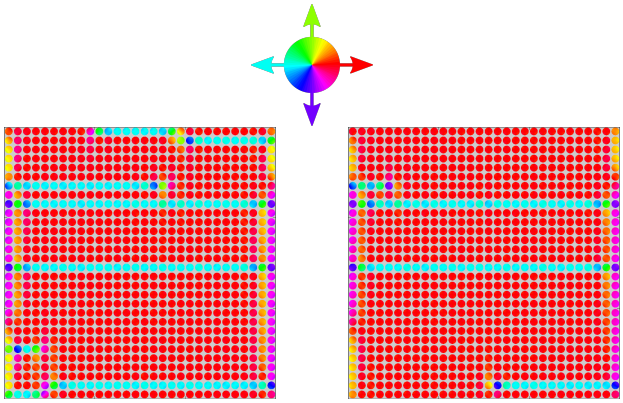

(e) IV (f) V

Figure B.5: Virgin magnetization curve of the square array along the [110]-direction (a) with the magnetic profile of the array at different points of the hysteresis loop (b-f). The blue curve is the full hysteresis loop.

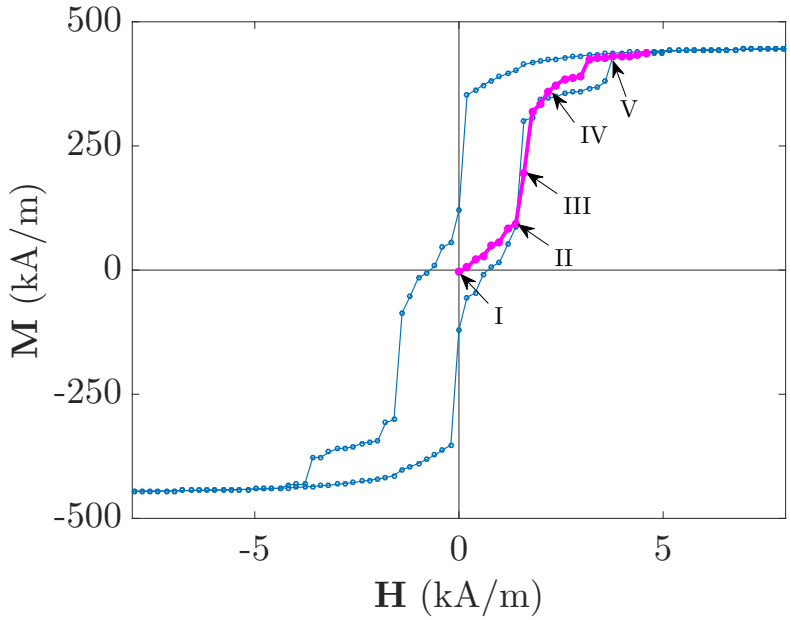


(a)

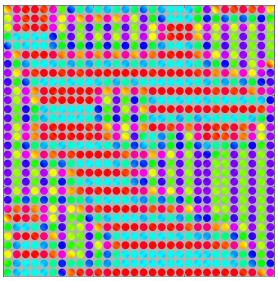

(b) I

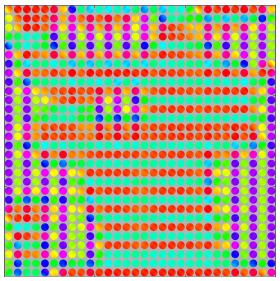

(c) II

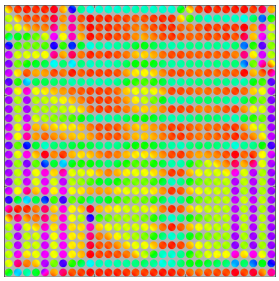

(d) III

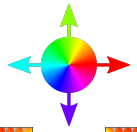

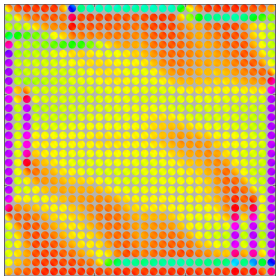

(e) IV

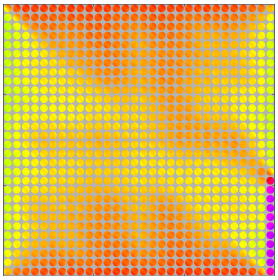

(f) V

Figure B.6: Virgin magnetization curve of the square array along the [010]-direction (a) with the magnetic profile of the array at different points of the hysteresis loop (b-f). The blue curve is the full hysteresis loop.

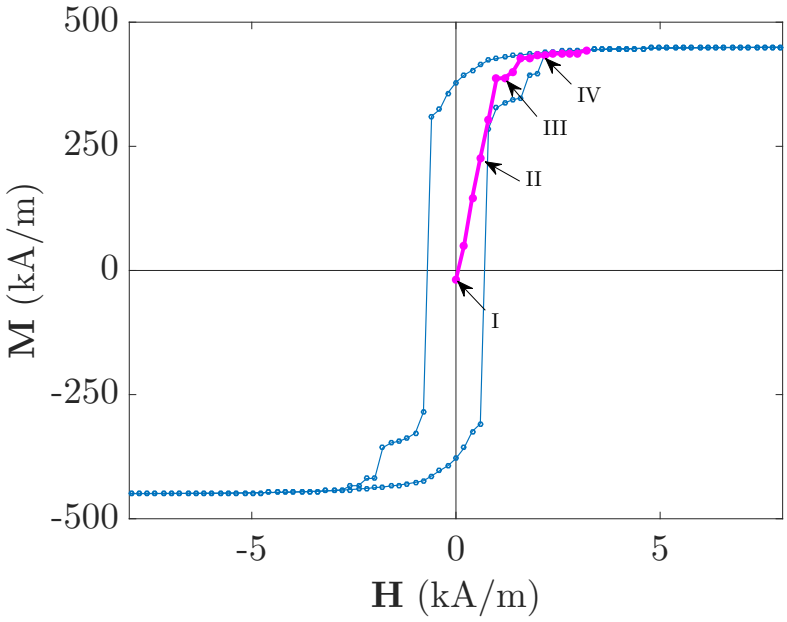


(a)

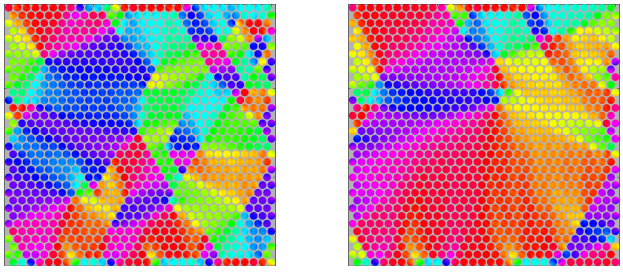

(b) I (c) II

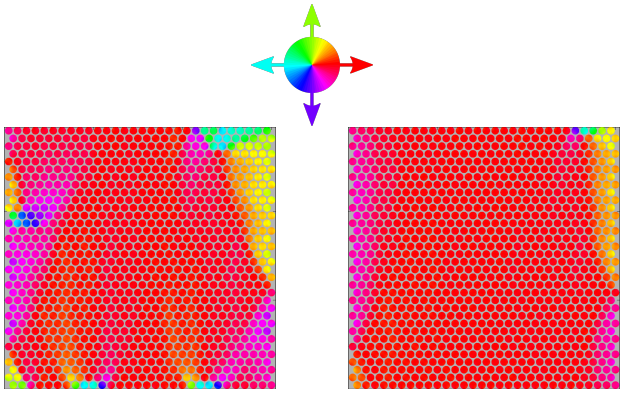

(d) III (e) IV

Figure B.7: Virgin magnetization curve of the hexagonal array along the $\boldsymbol{b}_1$-direction (a) with the magnetic profile of the array at different points of the hysteresis loop (b-e). The blue curve is the full hysteresis loop.

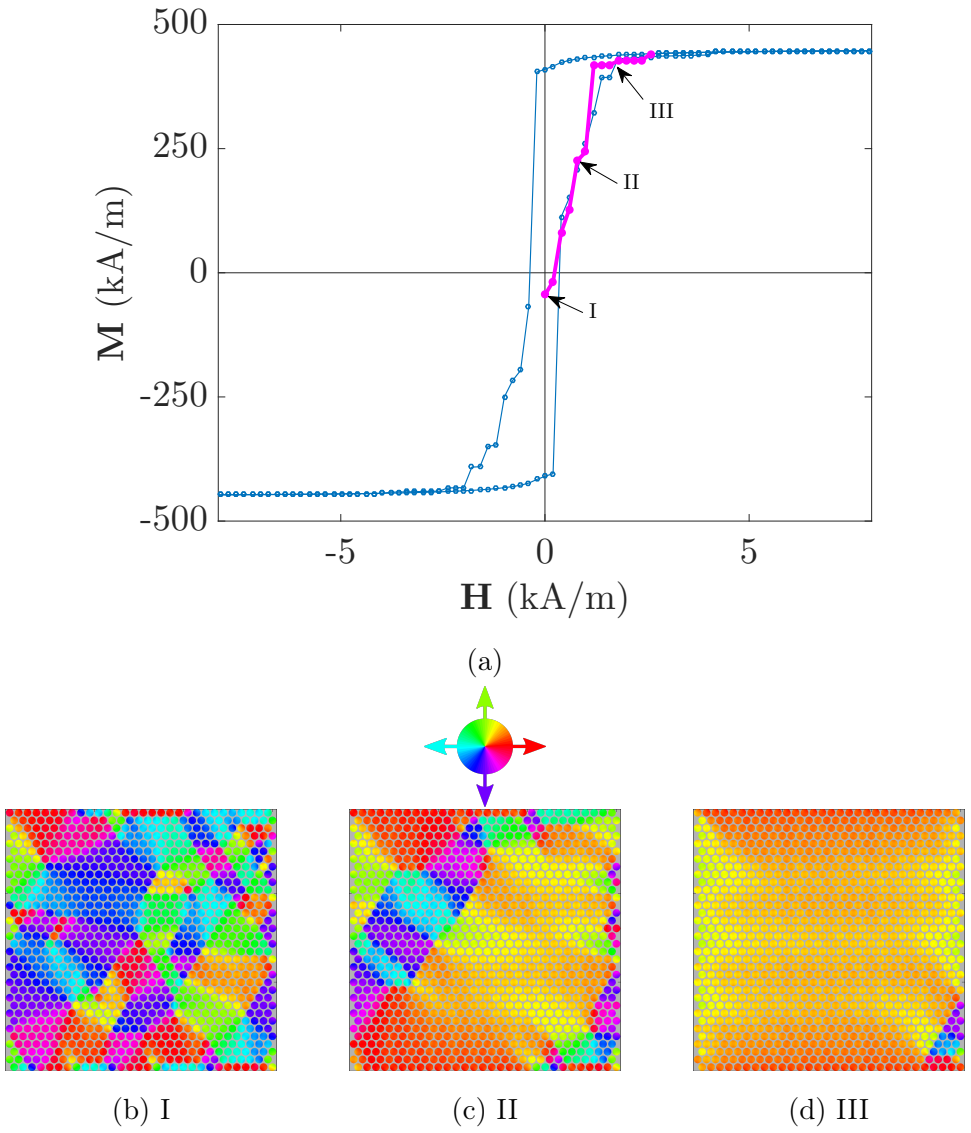


Figure B.8: Virgin magnetization curve of the hexagonal array along the 45° diagonal with respect to the $\boldsymbol{b}_1$-direction (a) with the magnetic profile of the array at different points of the hysteresis loop (b-d). The blue curve is the full hysteresis loop.

## B.4 Normalized field-cooled and zero-field-cooled magnetization

In this section we have included normalized plots of the field-cooled and zero-field cooled magnetization shown in Section 5.2.8. These are shown in Figure B.9 and B.10 for the square and hexagonal arrays respectively.

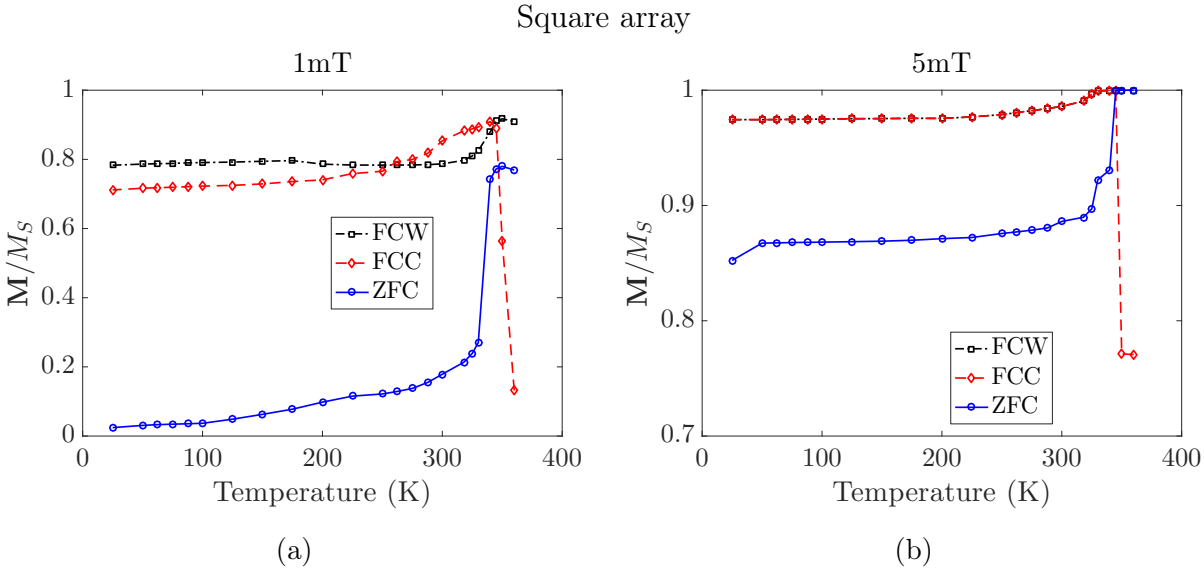


Figure B.9: Normalized plots of the "zero-field cooled" (ZFC), "field-cooled measured upon cooling" (FCC) and "field-cooled measured upon warming" (FCW) magnetization of the square array. The applied probing fields were (a) $\mu_0 \boldsymbol{H} = 1\,\mathrm{mT}$ and (b) $\mu_0 \boldsymbol{H} = 5\,\mathrm{mT}$. Note that the range of the y-axis in (a) is different from (b).

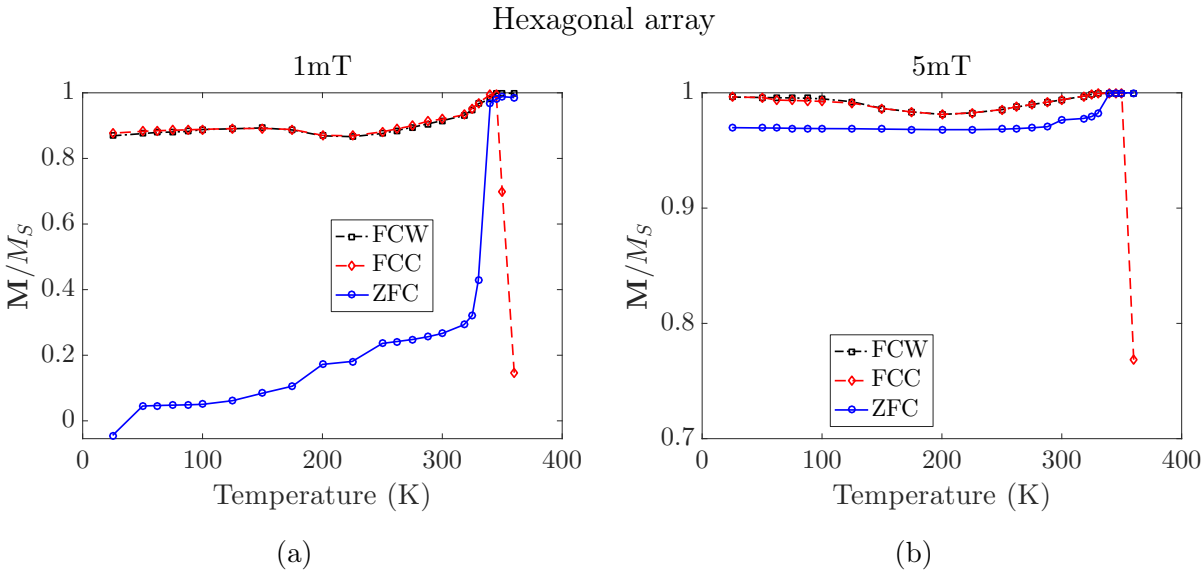


Figure B.10: Normalized plots of the "zero-field cooled" (ZFC), "field-cooled measured upon cooling" (FCC) and "field-cooled measured upon warming" (FCW) magnetization of the hexagonal array. The applied probing fields were (a) $\mu_0 \boldsymbol{H} = 1\,\mathrm{mT}$ and (b) $\mu_0 \boldsymbol{H} = 5\,\mathrm{mT}$. Note that the range of the y-axis in (a) is different from (b).

# References


[1] G. S. Abo, Y. Hong, J. Park, J. Lee, W. Lee, and B. Choi. Definition of Magnetic Exchange Length. *IEEE Transactions on Magnetics*, 49(8):4937–4939, Aug 2013.

[2] A. Aharoni. Micromagnetics: past, present and future. *Physica B: Condensed Matter*, 306(1-4):1–9, Dec 2001.

[3] M. N. Baibich, J. M. Broto, A. Fert, F. N. Van Dau, and F. Petroff. Giant Magnetoresistance of (001)Fe/(001)Cr Magnetic Superlattices. *Physical Review Letters*, 61(21):2472–2475, Nov 1988.

[4] P. Bak and R. Bruinsma. One-Dimensional Ising Model and the Complete Devil's Staircase. *Physical Review Letters*, 49(4):249–251, Jul 1982.

[5] S. Bedanta and W. Kleemann. Supermagnetism. *Journal of Physics D: Applied Physics*, 42(1):013001, Jan 2009.

[6] G. Bertotti, I. D. Mayergoyz, and C. Serpico. Basic Equations for Magnetization Dynamics. In *Nonlinear Magnetization Dynamics in Nanosystems*, pages 21–34. Elsevier, 2009.

[7] G. Bertotti, I. D. Mayergoyz, and C. Serpico. Numerical Techniques for Magnetization Dynamics Analysis. In *Nonlinear Magnetization Dynamics in Nanosystems*, pages 359–400. Elsevier, 2009.

[8] G. Bertotti, C. Serpico, and I. D. Mayergoyz. Nonlinear Magnetization Dynamics under Circularly Polarized Field. *Physical Review Letters*, 86(4):724–727, Jan 2001.

[9] G. Binasch, P. Grünberg, F. Saurenbach, and W. Zinn. Enhanced magnetoresistance in layered magnetic structures with antiferromagnetic interlayer exchange. *Physical Review B*, 39(7):4828–4830, Mar 1989.

[10] N. Bohr. I. On the constitution of atoms and molecules. *Philosophical Magazine Series 6*, 26(151):1–25, Jul 1913.

[11] P. Bright. Intel confirms tick-tock-shattering Kaby Lake processor as Moore's Law falters, Jul 2015. http://arstechnica.com/gadgets/2015/07/intel-confirms-tick-tock-shattering-kaby-lake-processor-as-moores-law-falters/ Accessed: June 13, 2016.

[12] W. F. Brown. Micromagnetics: Successor to domain theory? *Journal de Physique et le Radium*, 20(2-3):101–104, 1959.

[13] W. F. Brown. Thermal Fluctuations of a Single-Domain Particle. *Journal of Applied Physics*, 34(4):1319, 1963.

[14] W. F. Brown. The Fundamental Theorem of Fine-Ferromagnetic-Particle Theory. *Journal of Applied Physics*, 39(2):993, Nov 1968.

[15] W. F. Brown and A. E. LaBonte. Structure and Energy of One-Dimensional Domain Walls in Ferromagnetic Thin Films. *Journal of Applied Physics*, 36(4):1380, 1965.

[16] R. E. Camley and J. Barnaś. Theory of giant magnetoresistance effects in magnetic layered structures with antiferromagnetic coupling. *Physical Review Letters*, 63(6):664–667, Aug 1989.

[17] A. H. Compton. The magnetic electron. *Journal of the Franklin Institute*, 192(2):145–155, Aug 1921.

[18] J. L. Dormann, R. Cherkaoui, L. Spinu, M. Noguès, F. Lucari, F. D'Orazio, D. Fiorani, A. Garcia, E. Tronc, and J. P. Jolivet. From pure superparamagnetic regime to glass collective state of magnetic moments in $\gamma$-$Fe_2O_3$ nanoparticle assemblies. *Journal of Magnetism and Magnetic Materials*, 187(2):L139–L144, Aug 1998.

[19] M. E. Fisher and W. Selke. Errata: Infinitely Many Commensurate Phases in a Simple Ising Model. *Physical Review Letters*, 45(2):148–148, Jul 1980.

[20] M. E. Fisher and W. Selke. Infinitely Many Commensurate Phases in a Simple Ising Model. *Physical Review Letters*, 44(23):1502–1505, Jun 1980.

[21] V. Flovik, F. Macià, J. M. Hernàndez, R. Bručas, M. Hanson, and E. Wahlström. Tailoring the magnetodynamic properties of nanomagnets using magnetocrystalline and shape anisotropies. *Physical Review B*, 92(10):104406, Sep 2015.

[22] A. A. Fraerman, S. A. Gusev, I. M. Nefedov, Y. N. Nozdrin, I. R. Karetnikova, L. A. Mazo, M. V. Sapozhnikov, I. A. Shereshevsky, and L. V. Suhodoev. Magnetization curves for two-dimensional rectangular lattices of permalloy nanoparticles:

experimental investigation and numerical simulation. *Journal of Physics: Condensed Matter*, 13(4):683–689, Jan 2001.

[23] A. A. Fraerman and M. V. Sapozhnikov. Metastable and nonuniform states in 2D orthorhombic dipole system. *Journal of Magnetism and Magnetic Materials*, 192(1):191–200, Feb 1999.

[24] A. A. Fraerman and M. V. Sapozhnikov. Hysteresis model with dipole interaction: Devil's staircase like shape of the magnetization curve. *Physical Review B*, 65(18):184433, May 2002.

[25] B. Friedrich and D. Herschbach. Stern and Gerlach: How a bad cigar helped reorient atomic physics. *Physics Today*, 56(12):53–59, Dec 2003.

[26] J. Jordanovic, M. Beleggia, J. Schiøtz, and C. Frandsen. Simulations of superstructure domain walls in two dimensional assemblies of magnetic nanoparticles. *Journal of Applied Physics*, 118(4):043901, Jul 2015.

[27] P. A. Joy, P. S. A. Kumar, and S. K. Date. The relationship between field-cooled and zero-field-cooled susceptibilities of some ordered magnetic systems. *Journal of Physics: Condensed Matter*, 10(48):11049–11054, Dec 1998.

[28] R. Kikuchi. On the Minimum of Magnetization Reversal Time. *Journal of Applied Physics*, 27(11):1352, May 1956.

[29] E. J. Kim, J. L. R. Watts, B. Harteneck, A. Scholl, A. Young, A. Doran, and Y. Suzuki. Magnetic domain structure of $La_{0.7}Sr_{0.3}MnO_3$ nanoislands: Experiment and simulation. *Journal of Applied Physics*, 109(7):07D712, Mar 2011.

[30] C. Kittel. Theory of the Structure of Ferromagnetic Domains in Films and Small Particles. *Physical Review*, 70(11-12):965–971, Dec 1946.

[31] V. E. Klymenko, V. V. Kukhtin, V. M. Ogenko, and V. M. Rosenbaum. Steady configurations of a square dipole lattice in an external field. *Physics Letters A*, 150(3-4):213–215, Nov 1990.

[32] V. V. Kruglyak, S. O. Demokritov, and D. Grundler. Magnonics. *Journal of Physics D: Applied Physics*, 43(26):264001, Jul 2010.

[33] P. S. A. Kumar, P. A. Joy, and S. K. Date. Origin of the cluster-glass-like magnetic properties of the ferromagnetic system. *Journal of Physics: Condensed Matter*, 10(29):L487–L493, Jul 1998.

[34] D. Kutasov, A. Aharony, E. Domany, and W. Kinzel. Dynamic transition in a hierarchical Ising system. *Physical Review Letters*, 56(21):2229–2232, May 1986.

[35] A. E. LaBonte. Two-Dimensional Bloch-Type Domain Walls in Ferromagnetic Films. *Journal of Applied Physics*, 40(6):2450, Nov 1969.

[36] L. D. Landau and E. Lifshitz. On the theory of the dispersion of magnetic permeability in ferromagnetic bodies. *Phys. Z. Sowjetunion*, 8(153):101–114, 1935.

[37] M. S. Lee, T. A. Wynn, E. Folven, R. V. Chopdekar, A. Scholl, A. T. Young, S. T. Retterer, J. K. Grepstad, and Y. Takamura. Tailoring spin textures in complex oxide micromagnets. Submitted.

[38] L. Lundgren, P. Svedlindh, P. Nordblad, and O. Beckman. Dynamics of the Relaxation-Time Spectrum in a CuMn Spin-Glass. *Physical Review Letters*, 51(10):911–914, Sep 1983.

[39] J. C. Mallinson. Damped gyromagnetic switching. *IEEE Transactions on Magnetics*, 36(4):1976–1981, Jul 2000.

[40] M. C. Martin, G. Shirane, Y. Endoh, K. Hirota, Y. Moritomo, and Y. Tokura. Magnetism and structural distortion in the $La_{0.7}Sr_{0.3}MnO_3$ metallic ferromagnet. *Physical Review B*, 53(21):14285–14290, Jun 1996.

[41] S. Mørup and G. Christiansen. Influence of magnetic anisotropy on the superferromagnetic ordering in nanocomposites. *Journal of Applied Physics*, 73(10):6955, 1993.

[42] S. Mørup, M. F. Hansen, and C. Frandsen. Magnetic interactions between nanoparticles. *Beilstein Journal of Nanotechnology*, 1:182–190, Dec 2010.

[43] A. Moser, K. Takano, D. T. Margulies, M. Albrecht, Y. Sonobe, Y. Ikeda, S. Sun, and E. E. Fullerton. Magnetic recording: advancing into the future. *Journal of Physics D: Applied Physics*, 35(19):R157–R167, Oct 2002.

[44] S. A. Nikitov, D. V. Kalyabin, I. V. Lisenkov, A. Slavin, Y. N. Barabanenkov, S. A. Osokin, A. V. Sadovnikov, E. N. Beginin, M. A. Morozova, Y. A. Filimonov, Y. V. Khivintsev, S. L. Vysotsky, V. K. Sakharov, and E. S. Pavlov. Magnonics: a new research area in spintronics and spin wave electronics. *Physics-Uspekhi*, 58(10):1002–1028, Oct 2015.

[45] R. G. Palmer, D. L. Stein, E. Abrahams, and P. W. Anderson. Models of Hierarchically Constrained Dynamics for Glassy Relaxation. *Physical Review Letters*, 53(10):958–961, Sep 1984.

[46] Y. Perrin, I. A. Chioar, V. D. Nguyen, D. Lacour, M. Hehn, F. Montaigne, B. Canals, and N. Rougemaille. Artificial frustrated spin systems. In *Proc. SPIE*, volume 9551, pages 95511R–95511R–9, 2015.

[47] P. Politi and M. G. Pini. Dipolar interaction between two-dimensional magnetic particles. *Physical Review B*, 66(21):214414, Dec 2002.

[48] A. K. Pramanik and A. Banerjee. Interparticle interaction and crossover in critical lines on field-temperature plane in $Pr_{0.5}Sr_{0.5}MnO_3$ nanoparticles. *Physical Review B*, 82(9):94402, Sep 2010.

[49] C. Rodrigo, E. Jiménez, F. J. Teran, N. Mikuszeit, L. Méchin, J. Camarero, and R. Miranda. Tailoring magnetic anisotropy in epitaxial half metallic $La_{0.7}Sr_{0.3}MnO_3$ thin films. *Journal of Applied Physics*, 110(1):013919, 2011.

[50] V. Russier. Calculated magnetic properties of two-dimensional arrays of nanoparticles at vanishing temperature. *Journal of Applied Physics*, 89(2):1287, Jan 2001.

[51] M. R. Scheinfein, K. E. Schmidt, K. R. Heim, and G. G. Hembree. Magnetic Order in Two-Dimensional Arrays of Nanometer-Sized Superparamagnets. *Physical Review Letters*, 76(9):1541–1544, Feb 1996.

[52] N. A. Spaldin. *Magnetic Materials: Fundamentals and Device Applications*. Cambridge University Press, 2003.

[53] R. L. Stamps, S. Breitkreutz, J. Åkerman, A. V. Chumak, Y. Otani, G. E. W. Bauer, J. Thiele, M. Bowen, S. A. Majetich, M. Kläui, I. L. Prejbeanu, B. Dieny, N. M. Dempsey, and B. Hillebrands. The 2014 Magnetism Roadmap. *Journal of Physics D: Applied Physics*, 47(33):333001, Aug 2014.

[54] K. Steenbeck and R. Hiergeist. Magnetic anisotropy of ferromagnetic $La_{0.7}(Sr, Ca)_{0.3}MnO_3$ epitaxial films. *Applied Physics Letters*, 75(12):1778, 1999.

[55] J. Stöhr and H. C. Siegmann. *Magnetism: From Fundamentals to Nanoscale Dynamics*. Springer, 2006.

[56] D. Sundararajan. *Discrete Fourier Transform: Theory, Algorithms and Applications*. WSPC, River Edge, SG, 2001.

[57] Y. Takamura, R. V. Chopdekar, A. Scholl, A. Doran, J. A. Liddle, B. Harteneck, and Y. Suzuki. Tuning Magnetic Domain Structure in Nanoscale $La_{0.7}Sr_{0.3}MnO_3$ Islands. *Nano Letters*, 6(6):1287–1291, Jun 2006.

[58] Y. Takamura, E. Folven, J. B. R. Shu, K. R. Lukes, B. Li, A. Scholl, A. T. Young, S. T. Retterer, T. Tybell, and J. K. Grepstad. Spin-flop coupling and exchange bias in embedded complex oxide micromagnets. *Physical Review Letters*, 111(10):107201, Sep 2013.

[59] Y. Taur and T. H. Ning. *Fundamentals of Modern VLSI Devices*. 2013.

[60] S. Teitel and E. Domany. Dynamical phase transitions in hierarchical structures. *Physical Review Letters*, 55(20):2176–2179, Nov 1985.

[61] G. E. Uhlenbeck and S. Goudsmit. Spinning electrons and the structure of spectra. *Nature*, 117:264–265, 1926.

[62] A. Vansteenkiste, J. Leliaert, M. Dvornik, M. Helsen, F. Garcia-Sanchez, and B. Van Waeyenberge. The design and verification of MuMax3. *AIP Advances*, 4(10):107133, Oct 2014.

[63] M. Varón, M. Beleggia, J. Jordanovic, J. Schiøtz, T. Kasama, V. F. Puntes, and C. Frandsen. Longitudinal domain wall formation in elongated assemblies of ferromagnetic nanoparticles. *Scientific Reports*, 5:14536, Jan 2015.

[64] M. Varón, M. Beleggia, T. Kasama, R. J. Harrison, R. E. Dunin-Borkowski, V. F. Puntes, and C. Frandsen. Dipolar Magnetism in Ordered and Disordered Low-Dimensional Nanoparticle Assemblies. *Scientific Reports*, 3, Feb 2013.

[65] E. E. Vogel, J. Cartes, P. Vargas, D. Altbir, S. Kobe, T. Klotz, and M. Nogala. Hysteresis in $\pm J$ Ising square lattices. *Physical Review B*, 59(5):3325–3328, feb 1999.

[66] M. Wolf, J. Gleitzmann, and W. Gey. Relaxation-caused suppression of magnetization in superconducting $YBa_2Cu_3O_{7-\delta}$ single crystals. *Physical Review B*, 47(13):8381–8384, Apr 1993.

[67] J. Zabaleta, M. Jaafar, P. Abellán, C. Montón, O. Iglesias-Freire, F. Sandiumenge, C. A. Ramos, R. D. Zysler, T. Puig, A. Asenjo, N. Mestres, and X. Obradors. Nanoscale magnetic structure and properties of solution-derived self-assembled $La_{0.7}Sr_{0.3}MnO_3$ islands. *Journal of Applied Physics*, 111(2):024307, Jan 2012.

[68] I. Žutić and S. Das Sarma. Spintronics: Fundamentals and applications. *Reviews of Modern Physics*, 76(2):323–410, Apr 2004.